# Optimising marine seismic acquisition

## Source encoding in blended acquisition and target-oriented acquisition geometry optimisation

Wu, S.

**DOI**
10.4233/uuid:6ed94a0a-200d-470c-80be-f6c7ab56f2af

**Publication date**
2020

**Document Version**
Final published version

**Citation (APA)**
Wu, S. (2020). *Optimising marine seismic acquisition: Source encoding in blended acquisition and target-oriented acquisition geometry optimisation*. [Dissertation (TU Delft), Delft University of Technology]. https://doi.org/10.4233/uuid:6ed94a0a-200d-470c-80be-f6c7ab56f2af

# OPTIMISING MARINE SEISMIC ACQUISITION

SOURCE ENCODING IN BLENDED ACQUISITION
AND
TARGET-ORIENTED ACQUISITION GEOMETRY OPTIMISATION

# OPTIMISING MARINE SEISMIC ACQUISITION

SOURCE ENCODING IN BLENDED ACQUISITION
AND
TARGET-ORIENTED ACQUISITION GEOMETRY OPTIMISATION

## Proefschrift

ter verkrijging van de graad van doctor
aan de Technische Universiteit Delft,
op gezag van de Rector Magnificus prof. dr. ir. T. H.J.J. van der Hagen,
voorzitter van het College voor Promoties,
in het openbaar te verdedigen op 14 juli 2020 om 15:00 uur

door

**Sixue Wu**

Master of Science in Applied Geophysics,
Technische Universiteit Delft, ETH Zürich, RWTH Aachen
geboren te Wuhan, China.

Dit proefschrift is goedgekeurd door de

promotor: Dr. ir. G. Blacquière
promotor: Dr. ir. D. J. Verschuur

Samenstelling promotiecommissie:

| | |
|---|---|
| Rector Magnificus | voorzitter |
| Dr. ir. G. Blacquière | Technische Universiteit Delft, promotor |
| Dr. ir. D.J. Verschuur | Technische Universiteit Delft, promotor |
| | |
| *Onafhankelijke leden:* | |
| Prof. dr. H. Maurer | ETH Zürich |
| Dr. ir. G.J.A Groenestijn | TNO |
| Dr. ir. P. Zwartjes | Saudi Aramco |
| Prof. dr. ir. R.F. Hansen | Technische Universiteit Delft |
| Prof. dr. W.A. Mulder | Technische Universiteit Delft |
| Prof. dr. A.W. Martinius | Technische Universiteit Delft |

*Keywords:* acquisition design, optimisation, deblending, simultaneous source, inversion, genetic algorithm, parameterisation

*Printed by:* Ridder Print, the Netherlands



ISBN 978-94-6384-130-6

An electronic version of this dissertation is available at
http://repository.tudelft.nl/.

*To my family*

# CONTENTS

# SUMMARY

Seismic data acquisition is a trade-off between cost and data quality subject to operational constraints. Due to budget limitations, 3D seismic acquisition usually does not have a dense spatial sampling in all dimensions. This causes artefacts in the processed images, velocity models, or other physical properties. However, we rely on, for example, the accurate images in determining the location of oil and gas-bearing geological structures, and the accurate elastic properties to characterise the reservoir. In this thesis, we propose new methods to improve existing technologies that can optimise marine seismic acquisition. In Part I, we aim at obtaining dense data in less time by improving the so-called blended seismic acquisition techniques. In Part II, we aim at obtaining an improved target illumination with a limited number of sources and receivers by developing an acquisition optimisation framework.

**Part I**

In blended seismic acquisition, source encoding is essential at the acquisition stage to allow for the separation of blended sources at the processing stage. We propose new source encoding techniques—both man-made and natural types—in blended seismic acquisition to improve the deblending performance. The man-made type of source encoding is called shot repetition, which exploits the impulsive character of the marine seismic source in blending. This source code consists of repeated spikes of ones and can be realized physically by activating a broadband impulsive source more than once at (nearly) the same location. The use of shot repetition allows the deblending process to be carried out in individual shot gathers; therefore, it can cope with a sparse source sampling. Both numerical and field data examples show that the method is feasible.

The natural type of source encoding is referring to using source ghosts as a part of the blending codes. The source ghost is introduced by the strong sea surface reflection and it can be considered as the response of a virtual source located at the mirror position of the actual source. We propose an acquisition concept that includes the source ghost as a natural source encoding such that it can be used for blending, where the end result has been deblended as well as deghosted. Numerical examples of different blending scenarios demonstrate that it is possible to use the source ghost as a type of source encoding for deblending purpose. In addition, a field data example of a depth-distributed broadband source shows that the method can be used to obtain a broadband solution.

**Part II**

Imperfect spatial sampling causes a lack of illumination at the target in the subsurface. The hampered image quality at the target area of interest causes high uncertainties in hydrocarbon exploration, reservoir monitoring, hydrocarbon production or $CO_2$ injection, which can have a high economic impact. Especially in the case of a complex overburden, the relation between surface sampling and target illumination is not trivial. Target-

oriented acquisition analysis based on wavefield propagation has been used to guide optimising the acquisition parameters. Such acquisition design is usually a manual optimisation process, with consideration of many aspects.

We develop an acquisition optimisation framework that automatically updates the acquisition geometry for improved target illumination. In the acquisition design method, the forward model is the so-called focal beam analysis, which shows the influence of the acquisition geometry on image quality by the image resolution and the angle-dependent illumination imprint. We review the formulation of focal beam analysis for primary wavefields to prepare for the inverse problem. To solve the inverse problem, we first present a gradient method that can optimise the receiver geometry while the source geometry is fixed and vice versa. In the linearised scenario, the gradient method is sufficient to find an acceptable minimum. Second, we show a nonlinear optimisation framework to solve the design problem where nonlinear constraints are present. A genetic algorithm is used to optimise the receiver geometry while the source geometry is fixed. A low-rank parameterisation is proposed to make the size of the search space manageable and, thus, make it feasible to use a genetic algorithm to solve the nonlinear acquisition design problem efficiently. Third, we present a gradient method that can optimise both the source and receiver geometries in a flip-flop mode to obtain a good target illumination. With numerical examples, we demonstrate that the three proposed methods are effective.

# SAMENVATTING

Seismische data-acquisitie is een afweging tussen datakwaliteit en beperkingen bij acquisitie. Om de kosten beheersbaar te houden, is de bemonstering van bronnen en ontvangers bij 3D seismiek meestal minder dicht dan idealiter het geval is. Deze limitatie kan resulteren in artefacten in de verwerkte afbeeldingen, snelheidsmodellen en andere fysische eigenschappen. Nauwkeurige locaties en hoeveelheden van olie- en gasvoorraden hangen echter juist af van een goede weergave van de ondergrond. In dit proefschrift wordt een nieuwe methode geïntroduceerd om bestaande technieken te verbeteren in seismische data-acquisitie op zee. Deel I concentreert zich op het verzamelen van data met een dichtere bemonstering in een kleiner tijdsinterval door het verbeteren van gemengde ('blended') acquisitietechnieken. Deel II concentreert zich op het verkrijgen van een verbeterde belichting van het doelgebied in de ondergrond door middel van een geoptimaliseerde acquisitie die tevens minder bronnen en ontvangers nodig heeft.

**Deel I**

We stellen nieuwe technieken voor broncodering voor – zowel kunstmatige als natuurlijke typen – in gemengde seismische acquisitie om de scheiding ('deblending') prestaties te verbeteren. Het door de mens gemaakte type broncodering wordt schotherhaling genoemd. Schotherhaling exploiteert het impulsieve karakter van de seismische bron op zee bij het mengen. Deze broncode bestaat uit herhaalde pieken en kan fysiek worden gerealiseerd door een impulsieve breedbandbron meer dan eens op (bijna) dezelfde locatie te activeren. Het gebruik van schotherhaling maakt het mogelijk om het scheidingsproces uit te voeren per individuele schot-opname, waardoor het kan omgaan met schaars gepositioneerde bronnen. Uit zowel numerieke als veldgegevensvoorbeelden blijkt dat de methode haalbaar is.

Het natuurlijke type broncodering verwijst naar het gebruik van de spiegelbron (ghost source) als onderdeel van de bron scheiding codes. De spiegelbron wordt geïntroduceerd door de sterke reflecties aan het oppervlak van de zee en veroorzaakt zijn eigen responsie. We stellen een acquisitieconcept voor dat de spiegelbron bevat als een natuurlijke broncodering zodat het kan worden gebruikt voor het mengen. In het eindresultaat zijn de bronnen gescheiden zijn en is de responsie van de spiegelbronnen verwijderd. Numerieke voorbeelden van verschillende mengscenario's tonen aan dat het mogelijk is om de spiegelbron te gebruiken als een type broncodering voor het scheiden van bronnen ('deblending'). Tenslotte wordt aan de hand van velddata aangetoond dat een breedband-oplossing kan worden verkregen met een in diepte gedistribueerde breedband-bron.

**Deel II**

Imperfecties in acquisitie veroorzaken gebreken in de belichting van de ondergrond. Dit veroorzaakt gebreken in de datakwaliteit, wat op zijn beurt onnauwkeurigheden geeft in

olie- en gasexploratie, monitoren van reservoirs en productie of injectie bij reservoirs. Vooral bij een complexe structuur van de ondergrond is het verband tussen de acquisitiegeometrie aan de oppervlakte en de belichting van het doelgebied in de diepe ondergrond niet triviaal. Een op het doelgebied gerichte acquisitie-analyse gebaseerd op golf-propagatie is gebruikt om acquisitieparameters te optimaliseren. Dit is meestal een handmatig proces dat vele aspecten in overweging neemt.

We ontwikkelen een acquisitie-optimalisatie raamwerk dat automatisch de acquisitiegeometrie verbetert voor specifieke doelbelichting. In de methode van acquisitieontwerp, is het voorwaartse model de zogenaamde 'focal beam analysis'. Deze toont de invloed van de acquisitiegeometrie op de beeldkwaliteit via de beeldresolutie en de hoekafhankelijke belichting. We beginnen met de formulering van 'focal beam analysis' voor primaire golfvelden ter voorbereiding op het inverse probleem. Om het inverse probleem op te lossen, presenteren we ten eerste een gradiëntmethode die de ontvangergeometrie kan optimaliseren terwijl de brongeometrie vaststaat en vice versa. In het gelineariseerde scenario is de gradiëntmethode voldoende om een acceptabel minimum te vinden. Ten tweede laten we een niet-lineair optimalisatiekader zien om het ontwerpprobleem op te lossen voor het geval dat niet-lineaire beperkingen aanwezig zijn. Een genetisch algoritme wordt gebruikt om de ontvangergeometrie te optimaliseren terwijl de brongeometrie vast is. Een lage-rang parametrisatie wordt voorgesteld om de grootte van de zoekruimte beheersbaar te maken en zodoende een genetisch algoritme te kunnen gebruiken om het niet-lineaire acquisitie-ontwerp proleem op te lossen. Ten derde presenteren we een gradiëntmethode die, in afwisseling, zowel de bron- als ontvangergeometrie kan optimaliseren om een goede doelbelichting te verkrijgen. Met numerieke voorbeelden laten we zien dat de drie voorgestelde methoden effectief zijn.

# 1

# INTRODUCTION

1

The general purpose of seismic acquisition is to acquire data that reveal information about the subsurface, e.g. to determine the location of oil and gas bearing geological structures. This information can be structural images, velocity models and elastic properties of the earth. On land, dynamite or vibroseis trucks are used as sources, and geophone receivers measure particle velocity signals (Yilmaz, 2001). In marine streamer acquisition, vessel towed air gun arrays are used as impulsive sources, and hydrophones receivers measure pressure (Vermeer, 2002). Nowadays, there are also geophones in the streamer to measure particle velocity (Tenghamn, 2006). Ocean Bottom Seismic (OBS) survey deploys receivers, that consist of both hydrophones and geophones, at the sea bottom. It can measure both pressure and particle velocity. This thesis will focus on the marine acquisition aspect.

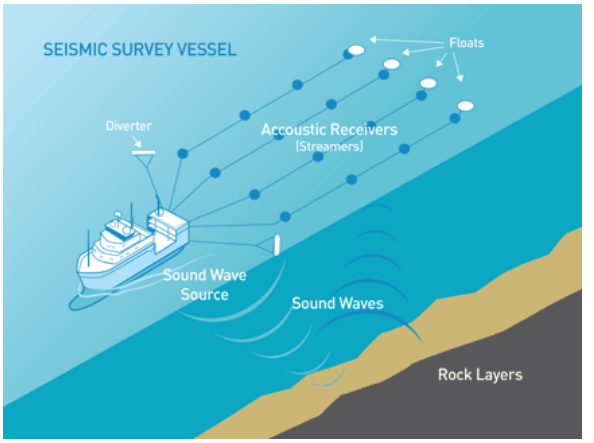


Figure 1.1: Illustration of a 3D marine streamer survey and the wave propagation paths (image from Pacific Gas Electric, 2019).

Seismic data acquisition is a trade-off between cost and data quality subject to operational constraints. Due to budget limitation, 3D seismic acquisition usually does not have dense spatial sampling in all spatial dimensions. This causes artefacts in the processed images, velocity models, or other physical properties. However, we rely on, for example, the accurate images in determining the location of oil and gas bearing geological structures, and the accurate elastic properties to characterise the reservoir. One challenge in seismic data acquisition is how to obtain densely sampled data in less time. Another challenge is how to obtain better quality data with a limited number of sources and receivers, which is especially prominent in a monitoring scenario.

In this thesis, we aim to improve existing technologies that can optimise marine seismic acquisition. Specifically, we look at the blended seismic acquisition for improvement of productivity; and we look at the acquisition geometry design for improvement of illumination quality.

## 1.1. BLENDED ACQUISITION

To tackle the first challenge, blended acquisition, or simultaneous source acquisition, has been proposed to acquire more data in less time (Beasley et al., 1998; Berkhout, 2008). In conventional acquisition, consecutive sources are fired with a waiting time to avoid interfering signals, and the waiting time can be long especially for deep targets. Blended acquisition allows signals to interfere with each other such that less survey time is used to acquire the same amount of sampling points. Similarly, in blended acquisition a denser source sampling can be achieved with the same time duration as in conventional acquisition. Therefore, this approach allows us to obtain more data in less time to improve data quality. In order to use the blended data, an additional processing step, called deblending, need to be added to the conventional processing workflow. The deblending methods require a dense source sampling to separate the interfering signals because the methods rely on signal coherency or sparsity in domains such as common receiver domain and common offset domain (e.g. Mahdad et al., 2011; Zu et al., 2017).

### 1.1.1. SOURCE ENCODING IN BLENDED SURVEY

In blended seismic acquisition, source signatures can be coded with sweeps or time delays at the acquisition stage to allow for separation of the blended sources at the processing stage (Barbier and Viallix, 1973; Bernhardt and Peacock, 1978; Womack et al., 1990). In seismic exploration, we are dealing with two types of source signatures: the short-duration impulsive and the long-continuous sweep (Ikelle, 2010). The sweep type of source encoding techniques, especially the linear sweep for onshore Vibroseis applications, has been well developed. In land Vibroseis surveys, multiple source responses that release sweep signals are recorded simultaneously (e.g. Andersen, 1995; Bagaini, 2006). Many of the Vibroseis sweeps are designed based on the orthogonality of signals, i.e. the autocorrelation of each signal is spiky while the cross-correlation of the signals is minimum. Such simultaneously acquired data can be separated as if they were acquired in a conventional way in the processing stage (Bagaini, 2008). The sweep type of source encoding cannot be applied to the airgun array.

In the current blended towed-streamer acquisition, mainly random time delays as a phase encoding technique are applied to the impulsive airgun sources along the source inline direction (e.g. Vaage, 2002). The corresponding deblending method is effective; however, its performance is often hindered by sparse source sampling because the method inherently requires a dense source sampling as it exploits signal coherency when resorting to other domains such as the common receiver domain. Barbier and Viallix (1973) introduced the marine seismic acquisition method called Sosie, where the source energy is split into a sequence of discrete pulses that have a spiky autocorrelation function. This approach was proposed to replace dynamite sources, used for marine acquisition in those days, such that the marine seismic acquisition would be more environmentally friendly. Abma et al. (2015) presented the independent simultaneous source acquisition, which makes use of orthogonal properties in blended seismic acquisition. Individual airguns in one airgun array are activated with controlled time delays to form near-orthogonal sequences. This type of source encoding in a blended experiment allows

effective deblending based on deconvolution of the source signature by sparse inversion in the common source domain (Mueller et al., 2015). On the other hand, it imposes challenges on hardware and real-time seismic data quality control.

In marine seismic acquisition, other types of source encoding techniques include the periodic source codes, which involve both time and space (e.g. Robertsson et al., 2016; Zu et al., 2016), and the source codes for the marine vibrator source (e.g. Halliday et al., 2017). Similar to the Vibroseis sweeps, the near-orthogonal marine source encoding can help achieving goals such as enhancing the signal and separating the interference. In this thesis, we discuss a phase source encoding technique that enables deblending independent of source sampling.

### 1.1.2. SOURCE GHOST AS NATURAL ENCODING

In marine seismic data, a source ghost is an event propagating upward from the source and reflected by the sea surface; in a similar fashion, a receiver ghost is the seismic data reflected by the sea surface, which ends at the receiver afterwards (Van Melle and Weatherburn, 1953; Parkes and Hatton, 1954). Ghost reflections are considered as noise because they cause frequency notches in the signal bandwidth, and deteriorate the temporal resolution in images. Numerous deghosting methods have been developed to achieve broadband seismic data: ghost elimination by linear and least-squares filtering (Lindsey, 1960; Schneider et al., 1964), ghost removal based on one-way wavefield extrapolation (Sønneland et al., 1986; Amundsen, 1993), deghosting methods based on Green's theorem (Weglein et al., 2002), wave-equation based deghosting (Beasley et al., 2013).

Many acquisition solutions have been developed for receiver-side deghosting: for example, depth-distributed streamers (Sønneland et al., 1986; Posthumus, 1993; Moldoveanu et al., 2007), slanted streamers (Bearnth and Moore, 1989; Soubaras and Lafet, 2011), dual-sensor streamers (Carlson et al., 2007; Day et al., 2013), and ocean bottom multicomponent receivers (Barr and Sanders, 1989; Docherty et al., 2005). In general, the receiver-side deghosting algorithms perform well due to the dense receiver sampling, especially in the inline direction.

In recent years, most developments of source deghosting are based on the depth-varying source array acquisition, which aims to avoid the notches introduced by the ghost reflection to be at the same frequency component (e.g. Moldoveanu, 2000; Hopperstad et al., 2008; Sablon et al., 2013; Parkes and Hegna, 2011). Numerical and field tests show that combining several source depths in an air gun array could improve the completeness of the source spectrum, especially in the low frequency bandwidth (Landrø and Amundsen, 2014; Haavik and Landrø, 2015). Still, source-side deghosting is more of a challenge because the deghosting algorithms suffer from the sparse source sampling in a typical marine seismic acquisition operation.

Instead of treating the source ghost as noise, we can also consider it as a virtual source located at the mirror position of the actual source. Thus, the ghost effect can be considered as a natural source encoding, and deghosting can be carried out with a deblending algorithm (Berkhout and Blacquiere, 2014). Additionally, it can be combined with man-made source codes (e.g. the random time delays in Parkes and Hegna, 2011) and provides an alternative algorithm to deal with the current depth-distributed broad-

band source.



## 1.2. ILLUMINATION-BASED ACQUISITION

A second challenge in seismic acquisition focuses on the data quality in terms of imaging quality. In the raw geophysical measurements, there are many quality control factors such as signal-to-noise ratio, fold coverage and signal coherency. Signal-to-noise ratio is typically enhanced by increasing the fold of coverage; signal coherency is enhanced by increasing the spatial sampling rates. However, these empirical requirement values do not guarantee a good quality of seismic deliverables, such as structural images, velocity models, and elastic parameters.

In classical acquisition design, geometries are decided prior to the acquisition based on the basic geological information such as target depth and maximum reflector dip angle (Vermeer, 2002). This approach ensures that the overall seismic image has good resolution and/or good angle coverage. However, certain targets can be inadequately imaged due to the complex geological overburden (Howard, 2007). The hampered image quality at the target area of interest can cause high uncertainties in reservoir monitoring and production, which can lead to high expenses. Ibrahim (2005) shows that the complex overburden, in combination with the used acquisition geometry, cause low-amplitude illumination and even shadow zones on the target reflectors in the reservoir, by using a 3D ray-trace modelling method. Howie et al. (2005) show a case study where the reprocessing of streamer seismic data alone did not provide enough uplift; an additional wide azimuth Ocean Bottom Seismic acquisition provided the required improvements in imaging. Muerdter and Ratcliff (2001) summarise the effects on illumination from different geological structures, and suggest that modelling should be done before acquisition to determine the acquisition parameters, such as the shooting direction, if the prior velocity model is available.

### 1.2.1. MODELLING APPROACHES FOR ACQUISITION DESIGN

Model-based acquisition analysis is a well-established approach to help us design a better acquisition geometry that ensures improved image quality at the target of interest. It uses modelling methods based on ray-tracing, the one-way wave equation and the two-way wave equation to compute the illumination criteria to appraise the acquisition geometry. This analysis is feasible where the macro subsurface velocity model with major reflectors is available, e.g. in a monitoring scenario. The *a priori* velocity model is used for modelling wavefield attributes that can indicate the illumination quality. For example, Muerdter and Ratcliff (2001) use ray-trace modelling; Volker et al. (2001) and Van Veldhuizen et al. (2008) use one-way wave equation modelling; Regone (2007) and Gardner et al. (2012) use finite-difference modelling; Kumar et al. (2016) use full wavefield modelling that includes multiple scattering wavefields. The results from these model-based acquisition analysis methods can qualify the target illumination property of the acquisition geometry and enable us to redesign the acquisition by changing the acquisition parameters to fulfil the illumination requirements. The acquisition geometry is

usually optimised by manually changing the acquisition parameters in the analysis until its illumination quality is acceptable.

### 1.2.2. GEOMETRY DESIGN AS AN OPTIMISATION

Solving a 3D seismic acquisition design as an optimisation problem was first proposed by Liner et al. (1998), where the challenge of balancing many geophysical requirements and operational constraints has been pointed out. For example, target values of fold coverage, bin size, far offset and azimuth coverage are required, while there is a limited number of available recording channels. Optimisation of the acquisition geometry is a nonlinear inverse problem. Morrice et al. (2001) parameterise an orthogonal split-spread design using decision variables on source and receiver location spacings, the amount of receiver equipment, and the production rate of the seismic crews. The problem statement is to minimise survey cost per square kilometre subject to geophysical requirements and operational constraints. The objective function is fast to calculate; therefore, the optimisation can be solved by the nonlinear optimization solver in Microsoft Excel. Similarly, Santos et al. (2019) optimise a 3D orthogonal land seismic surveys with seven geometry parameters and optimise a mixed-radix algorithm; a sufficient search is possible because the objective function involves simple calculations and therefore has no significant computation cost. However, the computation cost for a model-based acquisition design method is high, and we cannot afford to do a exhaustive search.

### 1.2.3. OPTIMISATION ALGORITHMS

The illumination-based acquisition design problem faces the challenges of the large amount of parameters and the nonlinearity of the design problem. Research has shown that global optimisation algorithms are effective for solving nonlinear problems. Alvarez et al. (2004) use an integer optimisation algorithm for a model-based 3D seismic survey design; Monsegny (2017) use a combination of a mix-integer algorithm and a particle swarm optimisation algorithm to optimise a split-spread survey. In order to quantify illumination using a wavefield modelling approach, both Alvarez et al. (2004) and Monsegny (2017) invert for only six standard design parameters, such that an exhaustive search is possible. Latiff et al. (2017) describe a particle swarm optimisation algorithm to optimise the target illumination under a gas cloud region; the objective function uses the illumination criteria defined by focal beam analysis; the receiver locations are considered as the particles; the parameters used in the search process are the three coefficients for the particles. Nakayama et al. (2019) use a repeated encoding sequence to form a parameter sequence in a genetic algorithm to optimise the deblending and data reconstruction quality in a 3D seismic survey. However, the computation costs for a model-based acquisition design method remain high. Linearised optimisation algorithms are fast. However, linearisation between the current sampling parameters and the illumination criteria is non-trivial since the sampling parameters are the spatial coordinates of the sampling points. This is one of the challenges taken up with this thesis.

## 1.3. THESIS OVERVIEW

### 1.3.1. RESEARCH QUESTIONS

The main questions that this thesis aims to answer are:

- How can source code design benefit blended marine seismic surveys?
- How can we optimise a seismic acquisition geometry for an improved target illumination, assuming a velocity model of the complex overburden is available?

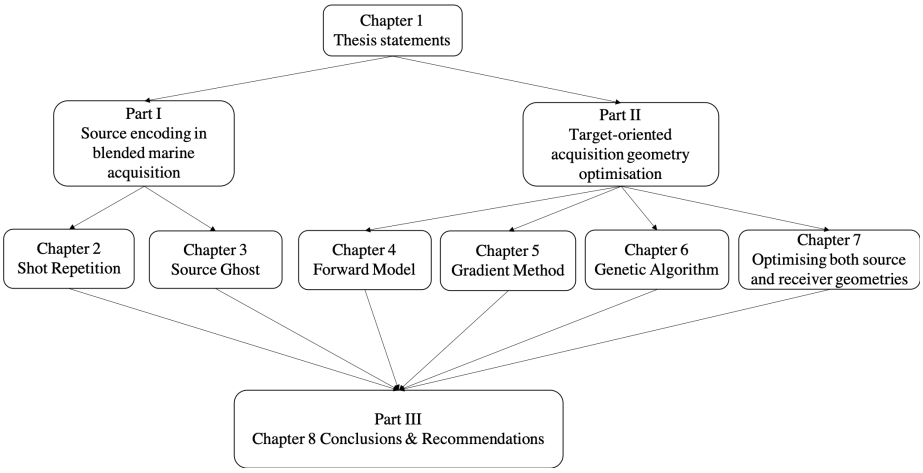


Figure 1.2: Illustration of the thesis outline.

### 1.3.2. OUTLINE

The outline of this thesis is shown in Fig. 1.2. The thesis consists of two parts, where Part I shows how we can further improve the blending technologies, and Part II shows the optimisation methods for acquisition geometry.

**Chapter 2** is the start of Part I. In this chapter, we introduce an alternative source encoding for blended marine seismic acquisition. The theory of blending and deblending is extended, and the deblending method is explained. The method is tested with a numerical example and field data.

In **Chapter 3**, we propose to use the source ghost as part of the blending code for blended marine seismic acquisition, such that the end result is deblended and deghosted. Firstly, the forward model that contains the ghost operator and the blending operator is given. Next, we show the deblending method with numerical examples of three different blending scenarios. A field data example of a depth-distributed broadband source is

shown to test our algorithm.

**Chapter 4** is the start of Part II of the thesis. In this chapter, we review and derive the formulations of focal beam analysis with primary wavefields, which is the forward model for the acquisition design problem. It shows the influence of the acquisition geometry on image quality by image resolution and angle-dependent illumination information. A numerical example is given to illustrate the focal beam analysis.

In **Chapter 5**, the linearised method of automated acquisition design is explained. We define the sampling density to be the inversion parameter. A two-step parameterisation approach is used to linearise the problem, and a gradient descent algorithm is implemented. We demonstrate the method with both simple and complex 3D velocity models.

In **Chapter 6**, we introduce an optimisation framework that uses a genetic algorithm to solve the acquisition design problem in a nonlinear scenario. The parameter space is reduced by using the results from the gradient method to form basis functions that describe our density function. We illustrate the method with an example that includes a cost constraint and a nonlinear operational constraint.

In **Chapter 7**, we present a gradient method that can optimise both source and receiver geometries in order to obtain a good target illumination, such that they can compensate the missing illumination for each other. Numerical examples with simple and complex 3D velocity models are used to demonstrate the method.

**Chapter 8** contains the general conclusions of this thesis and recommendations for future research.

# I

# PART I: SOURCE ENCODING IN BLENDED MARINE ACQUISITION

# 2

# SHOT REPETITION: AN ALTERNATIVE SEISMIC BLENDING CODE IN MARINE ACQUISITION

*In blended seismic acquisition, or simultaneous source seismic acquisition, source encoding is essential at the acquisition stage to allow for separation of the blended sources at the processing stage. In land seismic surveys, the vibroseis sources are encoded with near-orthogonal sweeps for blending. In marine seismic surveys, the sweep type of source encoding is difficult because the main source type in marine seismic exploration is the airgun array, which has an impulsive character. Another issue in marine streamer seismic data acquisition is that the spatial source sampling is generally coarse. This hinders the deblending performance of algorithms based on the random time delay blending code that inherently requires a dense source sampling as they exploit signal coherency in the common receiver domain. We present an alternative source code called shot repetition that exploits the impulsive character of the marine seismic source in blending. This source code consists of repeated spikes of ones and can be realized physically by activating a broadband impulsive source more than once at (nearly) the same location. Optimisation of the shot repetition type of blending code was done to improve the deblending performance. As a result of using shot repetition, the deblending process can be carried out in individual shot gathers. Therefore our method has no need for a regular dense source sampling: it can cope with irregular sparse source sampling; it can help with real-time data quality control. In addition, the use of shot repetition can be beneficial for the signal-to-background-noise ratio improvement.*

This chapter is adapted from a published paper in Geophysics (Wu et al., 2015).
DOI: https://doi.org/10.1190/geo2017-0649.1

In this chapter, we present an alternative seismic blending code that exploits the impulsive character of the marine airgun source and has no restrictions on source sampling (Wu et al., 2015). This source code, which we refer to as shot repetition, is a time sequence consisting of repeated spikes of ones and can be realized physically by activating the entire airgun array or several identical sub-arrays more than once at (nearly) the same location. An iterative deblending method, which is adapted from the one used in Mahdad et al. (2011), has been implemented for deblending in individual shot gathers. It overcomes sampling restrictions and simplifies real-time data quality control. Comparing with the more orthogonal blending codes that require precise control of the individual airguns, the practical implementation of our method and subsequent real-time data quality control are more straightforward. The shot repetition type of blending code was optimised to improve the deblending performance.

In the following sections, we extend the general forward model of source blending to include the case of shot repetition. After explaining the deblending method, we show results of deblending numerically blended field data with shot-repetition codes and a numerical example regarding background noise reduction. Finally, the deblending performance of the shot-repetition code is analysed.

## 2.1. THEORY AND METHOD

### 2.1.1. FORWARD MODEL

The matrix representation of seismic data (Berkhout, 1982) is used for constructing the forward model. The monochromatic seismic data is represented by **P**, the so-called data matrix in the frequency domain. Each element of **P** is a complex-valued number that represents one frequency component of a recorded trace. Each column of **P** represents a monochromatic shot gather, and each row represents a monochromatic receiver gather. Note that this matrix notation can represent both 2D and 3D seismic data, where in the case of 3D, each matrix column contains the concatenation of all receiver channels related to one seismic experiment (Kinneging et al., 1989). More details about the matrix notation can be found in Chapter 4.1 and 4.2. The general forward representation of source blending can be formulated as (Mahdad, 2012):

$$\mathbf{P}' = \mathbf{P}\Gamma, \tag{2.1}$$

where $\mathbf{P}'$ is the blended data matrix and $\Gamma$ is the blending matrix that contains the blending codes. Each column of $\Gamma$ corresponds to one blended seismic experiment, and each row of $\Gamma$ corresponds to a source location. The concept of using shot repetition as a seismic blending code is a special case of the above general forward model. In the case of shot repetition each source is activated more than once at nearly the same location. As a consequence, each nonzero element of the blending operator $\Gamma$ leads to multiple time delays for the source at location $k$ in blending experiment $l$. Hence, $\Gamma_{kl}$ can be written as a sum of phase terms:

$$\Gamma_{kl} = \sum_{n=1}^{N} e^{-j\omega\Delta t_{kl,n}}, \tag{2.2}$$

where $\Delta t_{kl,n}$ is the time shift corresponding to the $n^{th}$ activation of the source. For $N = 1$, each source is activated once with a certain time delay, representing conventional random time delay type of source encoding. The corresponding deblending method requires the full data set and the deblending power depends on the randomness of the shot time delays when resorting to other domains such as common receiver gathers. For $N > 1$, each source is activated more than once, representing shot repetition. The corresponding deblending method works on individual blended shot gathers. In this paper, we show examples with only one blended shot gather. In this case, the blending operator is a column of the full blending matrix $\Gamma$ and the blended data is a column of the full blended data $\mathbf{P}'$ in equation 2.1. For deblending a full data set, all shot gathers can be processed separately.

A simple numerical example of the forward model is illustrated in Figure 2.1. The unblended data is modelled as a fixed receiver spread with a spacing of 20 m. Two shots at lateral location 0.56 km and 2.48 km are coded with a pair of two-repetition source codes, and summed together to generate the blended data shown in Figure 2.1c. The shot-repetition codes used here are illustrated in Figure 2.2a and 2.2b, where the time delays between repeated spikes are 0.16 s and 0.24 s, respectively.

### 2.1.2. DEBLENDING METHOD

#### PSEUDO-DEBLENDING

Deblending aims at retrieving individual shots as if they were acquired conventionally. The deblending process is an underdetermined inverse problem, meaning that the blended data matrix $\mathbf{P}^{'}$ has fewer columns than $\mathbf{P}$. To solve this inverse problem, the following objective function is minimized:

$$J = ||\mathbf{P}^{'} - \mathbf{P}\Gamma||_2^2. \tag{2.3}$$

The general solution of the above least-squares minimization is referred to as the pseudo-deblended data:

$$\mathbf{P}_{ps} = \mathbf{P}^{'}\Gamma^{+}, \tag{2.4}$$

$$\Gamma^{+} = (\Gamma^{H}\Gamma)^{-1}\Gamma^{H}, \tag{2.5}$$

where $\Gamma^{+}$ is the generalized pseudoinverse and $\Gamma^{H}$ is the transposed complex conjugate or the Hermitian of the blending operator $\Gamma$. The pseudo-deblending procedure can be expressed as applying $\Gamma\Gamma^{+}$ to $\mathbf{P}$ according to equation 2.1. Because the blending operator $\Gamma$ contains the source codes in the frequency domain, $\Gamma^{H}$ in equation 2.5 performs correlations and $(\Gamma^{H}\Gamma)^{-1}$ in equation 2.5 is a diagonal matrix that scales the output amplitude to be minimum in the least-squares sense. Accordingly the diagonal elements of $\Gamma\Gamma^{+}$ are the scaled autocorrelations of source codes and the off-diagonal elements are the scaled cross-correlations of source codes in the frequency domain. Hence, the pseudo-deblending process can be seen as the scaled correlations of the source codes with the blended shot gather.

As an example, Figure 2.2 illustrates the diagonal and the off-diagonal elements of $\Gamma\Gamma^{+}$ after inverse Fourier transform, as the time-domain correlations, for $\Gamma$ that contains

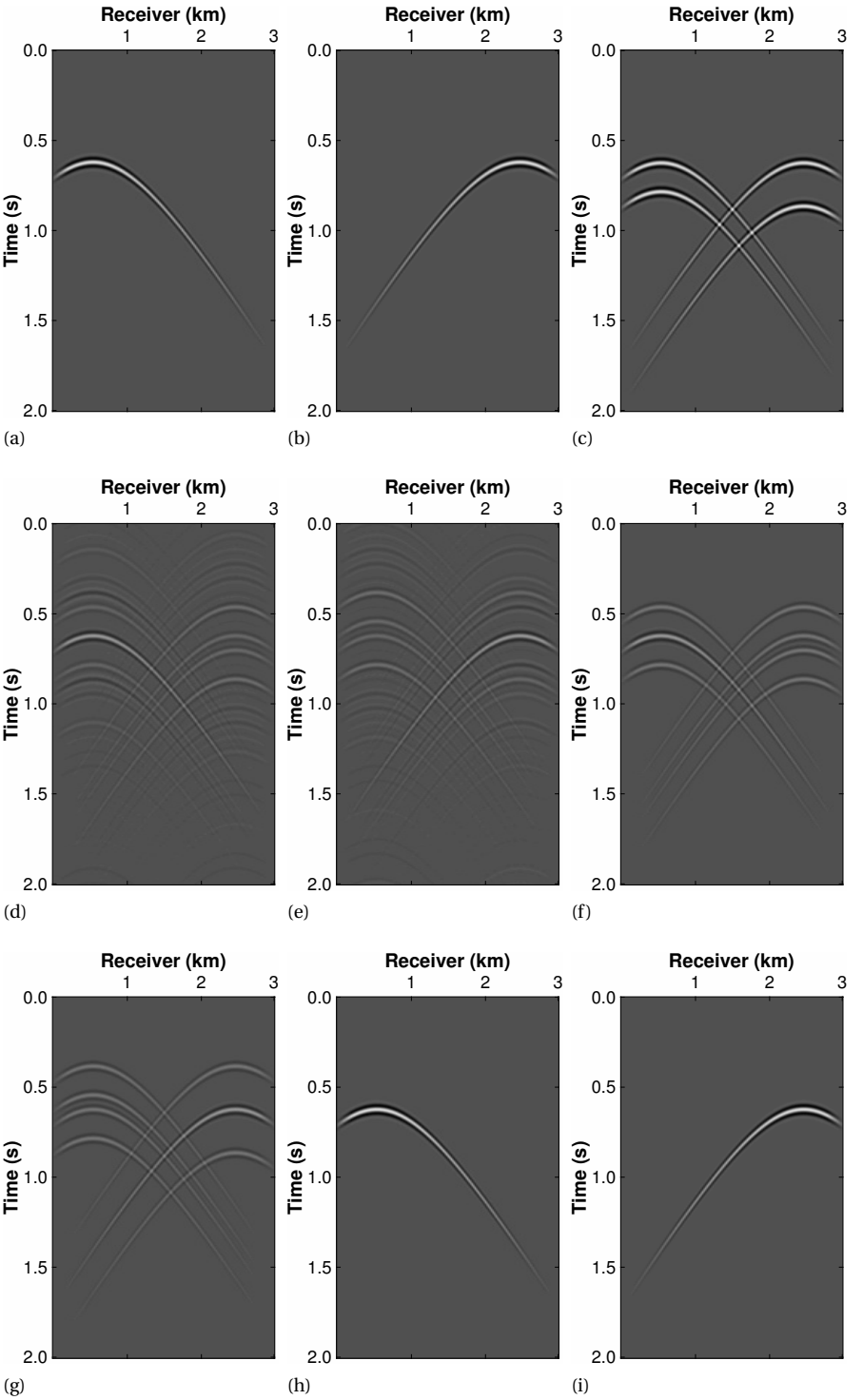


Figure 2.1: A numerical example of shot repetition: (a) unblended shot gather A, (b) unblended shot gather B, (c) blended shot gather including shot repetition, (d) pseudo-deblended shot gather A, (e) pseudo-deblended shot gather B, (f) blended shot gather correlated with the source code A, (g) blended shot gather correlated with the source code B, (h) deblended shot gather A, and (i) deblended shot gather B.

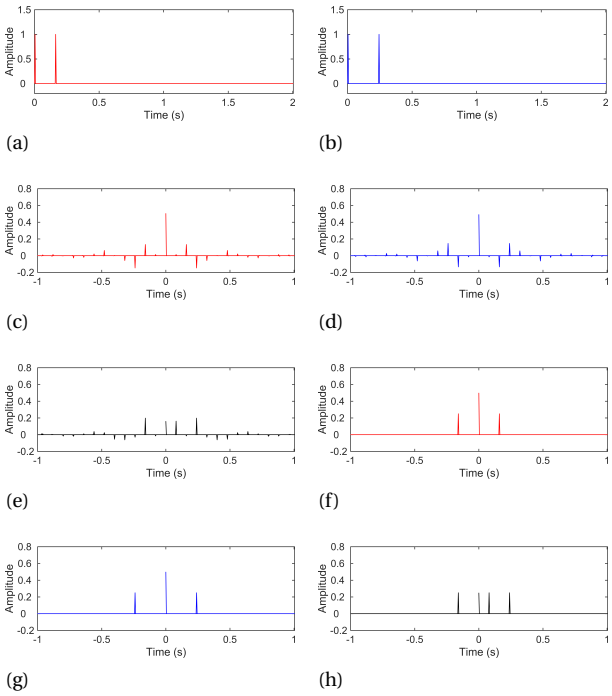


Figure 2.2: An illustration of a blending code set that contains two time delays: (a) source code A, (b) source code B, (c) scaled autocorrelation of source code A, (d) scaled autocorrelation of source code B, (e) scaled cross-correlation of source code A and B, (f) autocorrelation of source code A, (g) autocorrelation of source code B, and (h) cross-correlation of source code A and B.

the shot-repetition codes used in Figure 2.1. The zero-phased spikes in the autocorrelations in Figure 2.2c and 2.2d are related to the desired signals in Figure 2.1d and 2.1e, while the cross-correlation in Figure 2.2e is related to the interfering events in Figure 2.1d and 2.1e, which is also referred to as the blending noise. The success in deblending lies in the signal-to-blending-noise ratio in the pseudo-deblended data, which is related to the amplitude ratio of the peak to the cross terms. Figure 2 shows that the spike amplitude of 0.5 in the scaled autocorrelations in Figure 2.2c and 2.2d is higher than the maximum value of 0.2 among the cross terms in Figure 2.2e, yielding a ratio of 2.5.

Each column of the pseudo-deblended data $\mathbf{P}\Gamma\Gamma^{+}$ is a pseudo-deblended shot gather that contains the scaled autocorrelation of the shot, and the cross-correlation with the blended shot. It can be observed that the desired signals have higher amplitudes compared with both their side lobes and the blending noise in Figure 2.1d and 2.1e. This signal enhancement is due to the near-orthogonal source codes that are featured by a spiky autocorrelation function and low cross-correlation values (Mueller et al., 2016). This feature essentially allows deblending individual blended shot gathers.

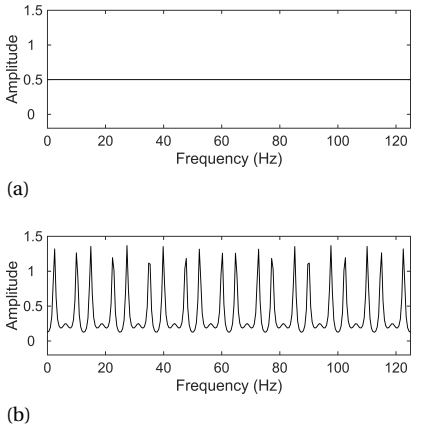


Figure 2.3: The amplitude terms of two blended sources, where (a) the source codes contain one time delay, and (b) the source codes contain two time delays.

#### BENEFIT OF AMPLITUDE SCALING IN THE CASE OF SHOT REPETITION

In the case of random time delay type of source encoding, each nonzero element of the blending operator $\Gamma$ contains a single phase term. The amplitude term $(\Gamma^H\Gamma)^{-1}$ in pseudo-deblending has scalar values on the diagonal for all frequencies. The pseudo-deblending can be expressed as multiplying with $\frac{1}{b}\Gamma^H$, where $b$ is a scalar value representing the number of blended shots in one experiment and $\Gamma^H$ corrects the phases in the correlation process (Mahdad, 2012). The amplitude scaling of $\frac{1}{b}$ ensures that the energy in the pseudo-deblended data and the energy in the blended data are equal, but it does not affect the amplitude ratio of the desired signal to the blending noise in the common shot domain. Figure 2.3a shows the amplitude term for a range of frequencies for $b = 2$.

As discussed before, pseudo-deblending in the case of shot-repetition source encoding as a correlation process can enhance the signal-to-blending-noise ratio in the common shot domain. From a processing point of view, the amplitude term $(\Gamma^H\Gamma)^{-1}$ maximizes this ratio in the least-squares sense for each frequency component. It is a periodic function of frequency. Figure 2.3b shows the amplitude term for a range of frequencies for a shot-repetition code with $N = 2$. Without the amplitude term, the magnitude of the spike in autocorrelation would be $N$ times the magnitude of the side lobes, and the cross-correlation would be $2N$ spikes of the value $\frac{1}{2N}$ as normal correlation process for optimised source codes. Figure 2.2f-h shows the correlations without the frequency-dependent amplitude scaling of the source codes in Figure 2.2a and 2b. Note that Figure 2.2f-h are normalized to compare to Figure 2.2c-e. The ratio of the spike value to the maximum value of the cross terms is 2, which is smaller than the one calculated before for Figure 2.2c-e (2.5). In the least-squares sense, the ratio of the spike value in Figure 2.2f and 2g to the sum of squared cross terms in Figure 2.2h is 2. While with the amplitude scaling in the pseudo-deblending, it can be calculated that the spike value in Figure 2.2c and 2.2d versus the sum of squared cross terms in Figure 2.2e reaches a higher ratio of 3.28. As an example with the simple synthetic seismic data, Figure 2.1f and g show the

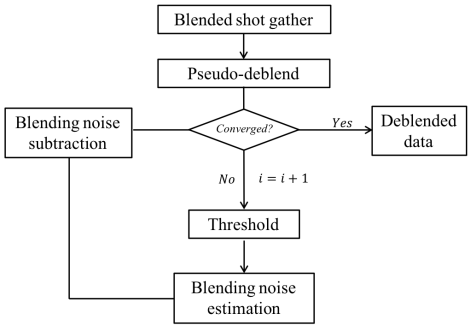


Figure 2.4: The workflow of the deblending method in the case of shot repetition.

blended shot gathers correlated with source code A and B, i.e. the pseudo-deblended shot gathers without the amplitude term. Note that Figure 2.1f and g are normalized to compare to Figure 2.1d and e. It is clearly visible that the interferences in Figure 2.1f and g have higher amplitudes than the interferences in pseudo-deblended shot gathers with amplitude scaling shown in Figure 2.1d and e.

#### ITERATIVE ALGORITHM

To further reduce the blending noise from the pseudo-deblended result, the iterative algorithm used in this paper is adapted from the deblending method proposed by Mahdad et al. (2011). That the deblending method is applicable in the common shot domain is due to the fact that the desired signal is stronger than the interference in the pseudo-deblended shot gathers. By incorporating a threshold for estimating the unblended data, we promote sparsity in the solution and the deblending problem is solved iteratively. The iterative updating scheme can be formulated as:

$$\mathbf{P}^{i+1} = \mathbf{P}'\Gamma^{+} - \overline{\mathbf{P}}^{i}[\Gamma\Gamma^{+} - \mathbf{I}], \tag{2.6}$$

where $\mathbf{P}^{i+1}$ represents the deblending result at iteration $i+1$, $\overline{\mathbf{P}}^{i}$ represents the deblended estimate constrained by the threshold at the $i^{th}$ iteration, and $\mathbf{I}$ is the identity matrix. A workflow of the deblending method in the case of shot repetition is given in Figure 2.4. The iterative process starts by applying a threshold to the pseudo-deblended data $\mathbf{P}_{ps}$, yielding a deblended estimate $\overline{\mathbf{P}}^{i}$. This estimate is blended and pseudo-deblended, and the interference is reconstructed by subtracting $\overline{\mathbf{P}}^{i}$ from $\overline{\mathbf{P}}^{i}\Gamma\Gamma^{+}$. The estimated interference $\overline{\mathbf{P}}^{i}[\Gamma\Gamma^{+} - \mathbf{I}]$ is subtracted from the pseudo-deblended data $\mathbf{P}'\Gamma^{+}$. The outcome is $\mathbf{P}^{i+1}$ containing less interfering energy. The iteration stops when there is no further improvement of the outcome. The results shown in Figure 2.1h and 2.1i are obtained by deblending the shot-repetition data in Figure 2.1c. It is clearly visible that the deblended shots are near-perfect compared with the original shots.

## 2.2. RESULTS

### 2.2.1. FIELD DATA EXAMPLE



To test the feasibility of the proposed blending technique in a more realistic setting, we applied the deblending method to a numerically blended field dataset. The original field data were from a 3D towed-streamer acquisition at the North Sea. The temporal and the spatial sampling interval are 4 ms and 12.5 m, respectively. In the pre-processed field data, the missing near offsets have been interpolated, and reciprocity was used to convert the data from a towed-streamer geometry to a split-spread geometry (Van Groenestijn, 2010). Two shot gathers at lateral location 0.375 km and 2.25 km from the pre-processed field data are coded numerically with the pair of source codes shown in Figure 2.7a and 2.7c, and blended to generate the data shown in Figure 2.5a. Each source code consists of eight repetitions.

The pseudo-deblended shot gathers are plotted in Figure 2.5b and 2.5f and the final deblended shot records are plotted in Figure 2.5c and 2.5g. It is clear that the desired signal has a much higher amplitude than the blending noise after pseudo-deblending. Compared with the original shot gathers in Figure 2.5d and 2.5h, it can be observed that the strong events in the shallow region from 0.0 s to 1.2 s are well resolved. The weak flat reflections in the deep region from 2.0 s to 3.0 s are quite well delineated. In this example the deblending error can be computed and displayed since the field data were numerically blended. The deblending errors are plotted in Figure 2.5e and 2.5i. The signal-to-noise ratio of the deblended data is 10.2 dB; the signal-to-noise ratio of the pseudo-deblended data is 3.1 dB; compared with the signal-to-noise ratio of shot-repetition data ($-11.8$ dB), pseudo-deblending reached an improvement of 14.9 dB and deblending reached an improvement of 22.0 dB. It took up to 10 seconds on a desktop computer to calculate the deblending results. This method can be easily paralleled for a full blended data set because the deblending process is carried out in individual blended shot gathers. This demonstrates that the technique can be applied during seismic acquisition and allows for real-time deblending quality control.

### 2.2.2. NOISE REDUCTION

Besides increasing the source density and/or reducing the survey time, blended acquisition improves the signal-to-noise ratio in seismic data (Berkhout and Blacquière, 2013). Both blended and unblended marine seismic records contain the planned, man-made source signal as well as signals from other sources such as traffic, fishing activities, flow noise, etc. The recorded events that are not related to the planned sources are referred to as the background noise. In the case of shot repetition, more sources are employed in each blended experiment and consequently more signal energy is sent into the subsurface while the background noise remains the same. The signal-to-background-noise ratio in shot-repetition data is therefore more favorable compared with conventional data or regularly blended data without shot repetition. In Figure 2.6, random background noise that consists of *f-k* filtered spikes is simulated and added to numerical shot-repetition data, where the unblended shot gathers in Figure 2.1a and 2.1b have

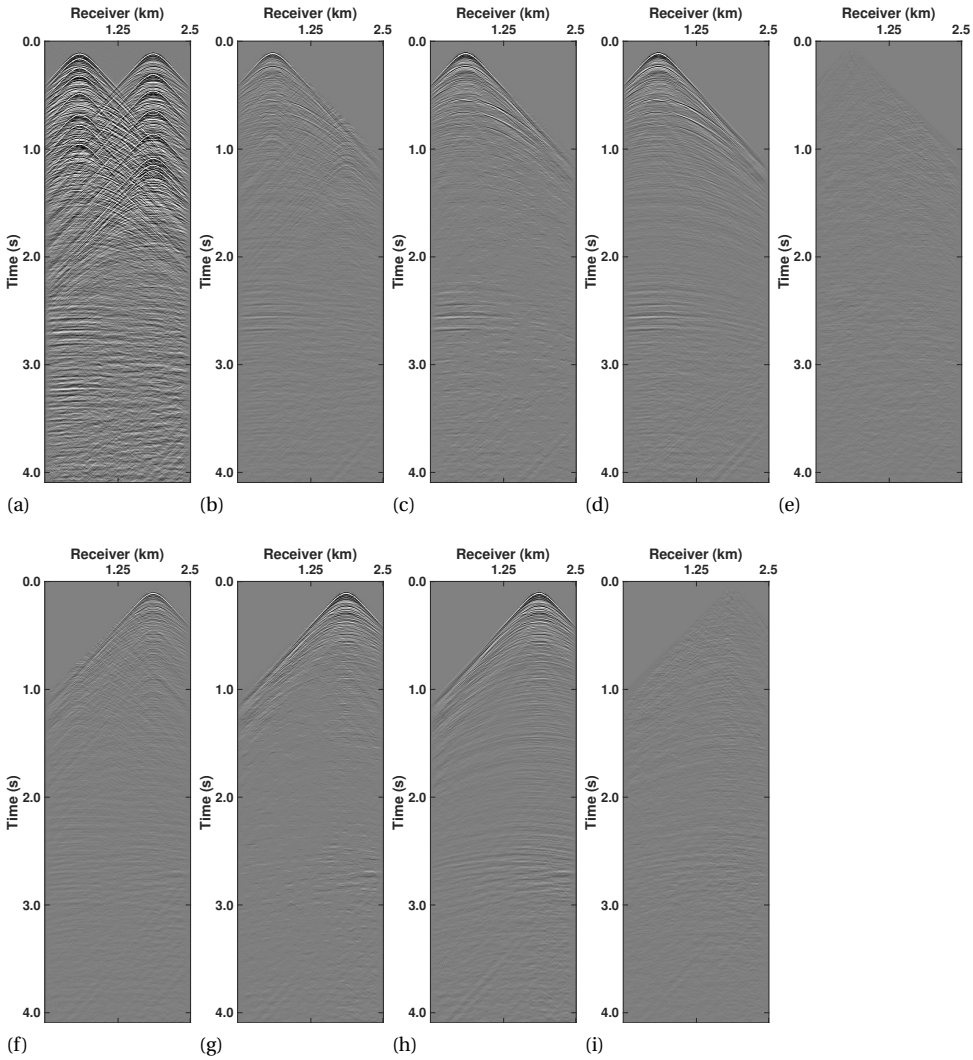


Figure 2.5: Field data example: (a) numerically blended shot gather, (b) pseudo-deblended shot gather A, (c) deblended shot gather A, (d) original shot gather A, (e) the deblending error of shot gather A (5c-5d), (f) pseudo-deblended shot gather B, (g) deblended shot gather B, (h) original shot gather B, and (i) the deblending error of shot gather B (5g-5h).

been blended using the same set of source codes as in the field data example. After deblending, the results have a lower noise level with the signal-to-background-noise ratio being 4.5 dB (Figure 2.6c and 2.6d). The conventional data with the same noise have the signal-to-background-noise level of −5.8 dB. The improvement is 10.3 dB. Again it is clear that the level of the residual noise in the deblended results is lower than the initial background noise level.

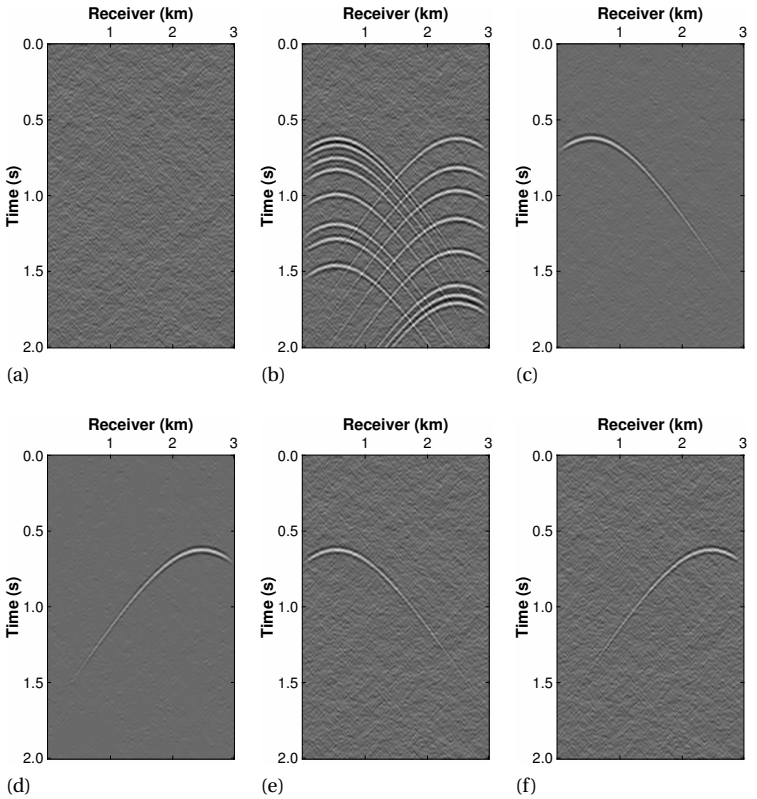


Figure 2.6: (a) Band limited random background noise, (b) blended shot gather with noise in a, (c) deblended shot gather A, (d) deblended shot gather B, (e) conventional shot gather A with noise in a, and (f) conventional shot gather B with noise in a.

### 2.2.3. SOURCE CODE OPTIMISATION

An important aspect of blended acquisition is the source code design. Mueller et al. (2016) described a method for optimising near-orthogonal source codes using a simulated annealing algorithm. Campman et al. (2017) utilized the so-called “Golomb Ruler" to optimise the shot firing time in an algebraic way such that the correlation property is maximized. In the case of shot repetition, we use a trial and error algorithm to optimise

the orthogonal properties of the blending code, which means we aim to obtain source code pairs with spiky autocorrelation and minimal cross-correlation. The deblending power depends on the signal-to-blending-noise ratio after pseudo-deblending. Since the pseudo-deblended data can be seen as the convolution of the scaled correlations of the shot-repetition source codes (such as in Figure 2.2c and 2.2d) and the unblended data, the scaled correlations of a source code pair can be used to indicate deblending performance. The spikes in autocorrelations represent the signal, while the cross-correlation represents the blending noise. The signal-to-blending-noise ratio in correlations can be evaluated by the amplitude of the spike in each autocorrelation divided by the sum of the squared cross-correlation values. The number of parameters in our shot-repetition code optimisation is $2N$, where $N$ is the number of repetitions in equation 2.2. Since the number of repetitions is limited, the number of parameters is small. It takes only 0.2 millisecond on a desktop computer for one trial and the number of trials is user defined. Typically, several hundred pairs of optimised shot-repetition codes can be obtained after 10000 trials.

Two pairs of source codes that contain eight repetitions are evaluated in Figure 2.7. The graphs on the left column correspond to the optimised source codes, while the graphs on the right column correspond to the non-optimised source codes. In this comparison, the correlation graphs of the pair of non-optimised source codes show side lobes and cross terms with higher amplitudes than those calculated using the optimised codes. It indicates that blending with the optimised source codes can reach better signal-to-blending-noise ratio than blending with the non-optimised source codes in the pseudo-deblended data.

Besides orthogonal properties, another factor we considered in optimising shot-repetition codes is the number of repetitions $N$. The larger the $N$ value, the better the signal-to-blending-noise ratio in correlation, and the better initial guess for deblending. This can be shown by comparing the scaled correlation graphs of the source codes which contain two spikes in Figure 2.2 with the scaled correlation graphs of the source codes which contain eight spikes in Figure 2.7.

Ten pairs of optimised source codes within a fixed time window are generated for each $N$ that ranges from 2 to 8, and they are tested using the field data discussed above. The residual noise level shows a decreasing trend (Figure 2.8a). Furthermore, the signal-to-noise ratio and the signal-to-noise ratio improvement of the deblending results both show an increasing trend (Figure 2.8b and 2.8c). This indicates that a higher number of shot repetitions is potentially better for the deblended data quality. Nevertheless, the residual noise level reduction with the increasing number of shot repetitions is limited. It is up to the acquisition requirement whether to adopt more repetitions in practice.

## 2.3. DISCUSSION

We have shown that the deblending method proposed by Mahdad et al. (2011) after a few modifications can be applied to shot-repetition data in individual shot gathers. In this paper, a threshold as a simple sparsity constraint is chosen to test the feasibility of shot-repetition blending. A more sophisticated sparsity promoting procedure in the

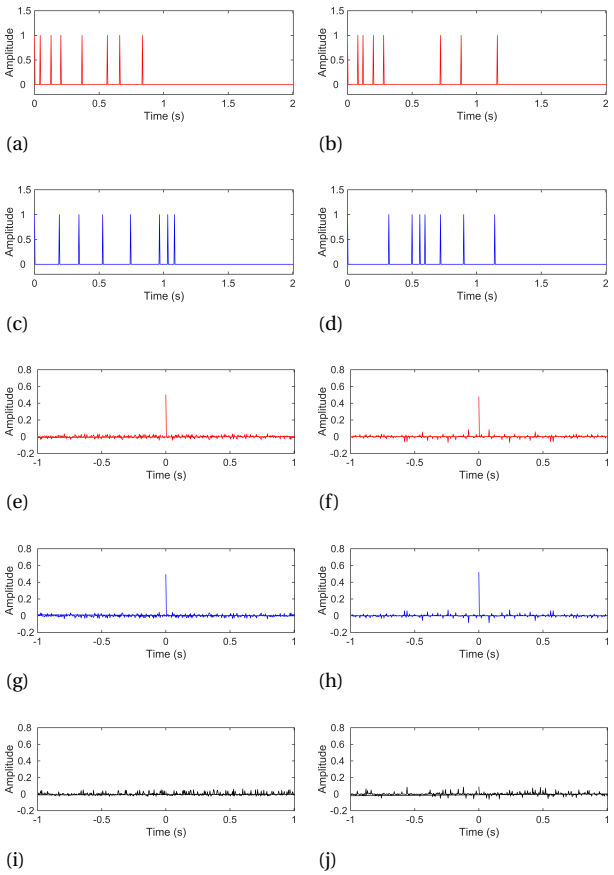


Figure 2.7: Left column: (a) optimised shot-repetition code A, (c) optimised shot-repetition code B, (e) scaled autocorrelation of source code A, (g) scaled autocorrelation of source code B, and (i) scaled cross-correlation of source code A and B. Right column: (b) non-optimised shot-repetition code A, (d) non-optimised shot-repetition code B, (f) scaled autocorrelation of source code A, (h) scaled autocorrelation of source code B, and (j) scaled cross-correlation of source code A and B.

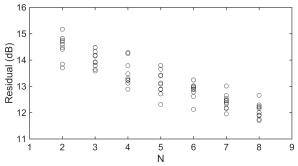


(a)

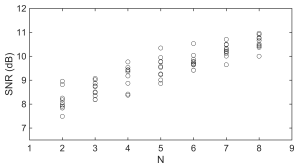


(b)

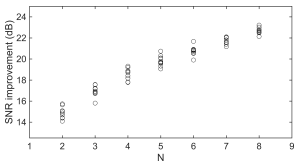


(c)

Figure 2.8: (a) The residual noise level in the deblending results. (b) The signal-to-noise ratio of the deblending results. (c) The signal-to-noise ratio improvement of the deblending results with increasing the number of shot repetitions.

deblending algorithm such as the focal-curvelet hybrid transform (Kontakis and Verschuur, 2017) or a better denoising tool such as the rank-reduction method (Chen et al., 2016) would likely improve the results even further. Furthermore, it is convenient to combine shot-repetition codes with other blending codes because of the same general source blending representation. Kontakis et al. (2016) performed numerical tests that combine shot repetition with the random time delays. The results showed that the additional constraints in common-receiver domain can improve separating the interfering energy in deblending on the condition of a sufficiently dense source sampling. The deblending framework based on shaping regularization proposed by Chen et al. (2014) offers a flexible way to control deblending using sparsity or coherency constraints. It is extended to a multiple-constraints regularized deblending framework by Chen (2015) with the extra constraint called iterative orthogonalization. From a processing point of view, this constraint enhances the signal-to-blending-noise ratio at each iteration and it helps speed up the convergence.

As Abma and Ross (2015) addressed, practical aspects are important in seismic marine source encoding. Besides the optimisation of source codes via evaluating correlation, some practical concerns should be addressed when designing such source codes, such as the varying source signatures, the engineering aspects, and the duration of the planned survey.

It has been shown that a larger repetition number $N$ can potentially improve the deblending quality provided that each shot can be perfectly repeated. In practice, the signature varies from shot to shot. More repetitions could introduce more shot-by-shot signature variations due to higher operational uncertainties. The appropriate choice of shot-repetition numbers in the code design should take both the benefit and the operational uncertainties into account. The minimum time shift in source code design is restrained by many engineering aspects, e.g., the total capacity of the onboard compressors, the duration of refilling the airgun, and the bubble periods for different size of airguns. The maximum time shift is limited by the criterion that the duration of the blended survey has to be shorter than the duration of the corresponding unblended survey for economical reasons.

As mentioned before, shot repetition type of source encoding can be realized in practice by activating the entire airgun array or several identical sub-arrays in sequence (similar to Parkes and Hegna, 2011). Because the signature variation between the repeated shots at nearly the same source location is assumed to be identical in this theoretical study, we recommend measuring both the firing times and the airgun signatures to allow a successful deblending. In general marine applications of source encoding, the near-field hydrophone measurement of the source signatures is as important as the recording of the shot firing times for deblending such field data.

Moreover, the amplitude of all repeated shots may be reduced in the source code design since the deblended data can still achieve the same amplitude as in the single-shot unblended data. This may contribute to a method that is more environmentally friendly with respect to the production of underwater noise. In a manner similar to that of the Sosie method proposed by Barbier and Viallix (1973), the energy of the output signal depends on the energy of the input signal. A prolonged input signal with lower average amplitude over time can supply the same amount of energy injection.

## 2.4. CONCLUSION

Shot repetition is a feasible alternative approach for source encoding in blended marine acquisition. It exploits the impulsive character of the marine seismic source. We demonstrated that the deblending method based on shot-repetition blending codes can be carried out in individual shot gathers with numerically blended field data. Accordingly our method has no need for a regular dense source sampling: it can cope with spatially sparse or irregular source sampling; it can help with real-time data quality control. From the signal-to-noise ratio analysis of a range of optimised source codes, we showed that optimisation of source code can improve the deblending performance. Another benefit of incorporating more shots per source location is that it can help reduce the random background noise.



It is possible to combine shot-repetition codes with other blending codes, e.g. random time delays to the blended inline sources. When the source sampling is sufficient, the additional constraint in other domains such as the common-receiver domain, can improve separating the interfering energy in deblending. When designing the source codes, it is beneficial to optimise them to improve the deblending performance. From a practical aspect, our source encoding method can be implemented straightforwardly by activating the entire airgun array or several identical sub-arrays repetitively. Additional effort of real-time data quality control is minimum because the shot-repetition data resembles the conventional data appearing multiple times.

# 3

# UTILIZING THE SOURCE GHOST IN A BLENDED MARINE ACQUISITION

*In blended data acquisition, source encoding is needed for the separation of the blended source responses. The source ghost introduced by the strong sea surface reflection can be considered as a virtual source located at the mirror position of the actual source. In this chapter, we propose an acquisition concept that includes the source ghost as a natural source encoding such that it can be used for deblending, where the end result has been deblended as well as deghosted. This acquisition method is easy to combine with man-made source encoding and also the concept of using the source ghost provides an interesting alternative to deal with the current depth-distributed source for broadband seismic data.*

This chapter is adapted from a published SEG Technical Program Expanded Abstract (2016).
DOI: https://doi.org/10.1190/segam2016-13684486.1

In blended data acquisition, source encoding is needed for the separation of the blended sources. In marine seismic surveys, many approaches of temporal source encoding have been employed (e.g. Abma et al., 2015; Mueller et al., 2015; Wu et al., 2015; Vaage, 2002). In this work, we consider the naturally blended source, i.e. the source ghost, as part of the blending code (Berkhout and Blacquiere, 2014). With the help of this natural blending code in depth, it is possible to use the source ghost for deblending. In addition, it is easy to combine with man-made source encoding and provides an interesting alternative to deal with the current depth-distributed broadband source.



In this chapter, we present three cases where source ghosts are treated as signal and then separated from the source response. In the first case, two sources are activated near simultaneously at different lateral locations. They are towed at different depths, and therefore these two sources also have different source ghosts correspondingly. In the second case, the blended source geometry is the same as in the first case. However this time each physical source is activated in a shot-repetition fashion, i.e. activated twice with certain time delays (Wu et al., 2015). The third case contains two sources situated at the same lateral position but at different depths. This is an analogue of the current depth-distributed source and a field data example will be discussed.

## 3.1. FORWARD MODEL

The forward model of blending with the source ghost is formulated based on the matrix representation described in Berkhout (1982). With the premise that the source sampling is sufficient, the monochromatic blended data can be formulated as:

$$\mathbf{P}^{'}(z_0;\pm z_m) = \mathbf{P}(z_0;z_0)\mathbf{G}(z_0,\pm z_m)\mathbf{\Gamma}, \tag{3.1}$$

where $\mathbf{P}(z_0;z_0)$ represents the unblended data acquired with both source and receiver arrays at the sea surface $z_0$. $\mathbf{G}$ represents the source ghost operator that generates the real source response with the ghost source response from all the sources presented in $\mathbf{P}(z_0;z_0)$:

$$\begin{aligned} &\mathbf{G}(z_0,\pm z_m) = \mathbf{F}(z_0,+z_m) + \mathbf{R}(z_0)\mathbf{W}(z_0,-z_m), \\ &with \quad z_m = z_m(z_1,z_2,...). \end{aligned} \tag{3.2}$$

Each row and column of $\mathbf{G}$ corresponds to the lateral source location in the unblended and ghost free data $\mathbf{P}(z_0;z_0)$. In the nonzero elements of the source ghost operator $\mathbf{G}(z_0,\pm z_m)$, $\mathbf{F}(z_0,+z_m)$ inverse extrapolates the wavefield to the actual source depth $z_m$, while $\mathbf{R}(z_0)\mathbf{W}(z_0,-z_m)$ forward extrapolates the wavefield to the source ghost depth $z_m$ and applies the sea surface reflectivity $\mathbf{R}(z_0)$, which generates the source ghost response. The depth level used in extrapolation is denoted by the function $z_m$, which is a function of the depth levels of each blended source $z_1, z_2$ and so on. After applying $\mathbf{G}(z_0,\pm z_m)$, all the sources have been extrapolated from the sea surface level to their respective depths below and above the sea surface. The above-mentioned extrapolation process can be implemented in the wavenumber frequency domain in the case of laterally invariant parameter values (speed of sound in water and sea surface reflectivity).

In equation 3.1, $\mathbf{\Gamma}$ is the blending matrix that contains the temporal source encoding. Each column of $\mathbf{\Gamma}$ corresponds to one blended seismic experiment, and each row corresponds to a source location. In this work, each nonzero element of $\mathbf{\Gamma}$ is formulated as a sum of phase terms, based on the source time delay $\Delta t_{kl,n}$:

$$\mathbf{\Gamma}_{kl} = \sum_{n=1}^{N} e^{-j\omega_{kl,n}}. \tag{3.3}$$

In the case where no temporal source encoding is applied, each nonzero element of $\mathbf{\Gamma}$ equals one. Figure 3.1a shows an example of blending two sources at different tow-depths. In the case where only one shot is fired at each source position (N=1 in equation 3.3), the blending matrix $\mathbf{\Gamma}$ represents the dithering blending code. In the case of shot repetition ($N \geq 2$ in equation 3.3), $\mathbf{\Gamma}$ becomes a sum of time shifts which adds the benefit of deblending being possible within a single common shot gather (Wu et al., 2015). In Figure 3.1d, an example of two sources at different tow-depths blended in a shot repetition fashion is shown.



## 3.2. DEBLENDING METHOD

By minimizing the objective function $||\mathbf{P}^{'} - \mathbf{PG\Gamma}||_2^2$, a least-squares solution is obtained for $\mathbf{P}$, and used as the start of an iterative process. This solution, $\mathbf{P}_{ps}$, is often referred to as the pseudo-deblended data:

$$\mathbf{P}_{ps} = \mathbf{P}^{'}(\mathbf{\Gamma}^H\mathbf{\Gamma})^{-1}\mathbf{\Gamma}^H(\mathbf{G}^H\mathbf{G})^{-1}\mathbf{G}^H. \tag{3.4}$$

In the pseudo-deblending process described by the above equation, the blended data is correlated with the source encoding which is a combination of time and depth.

To use the source ghost, the blended sources are required to be towed at different depths such that their corresponding source ghosts are different (Figure 3.1a). No temporal source encoding has been applied. It can be clearly observed that the ghosts of the blended sources have different phase shifts. Figure 3.1b shows a pseudo-deblended shot gather related to the left source. The amplitude of the left source signal is twice as strong compared with both its side lobes (ghosts) and the dispersed right source. Note that the pseudo-deblended data has a lower amplitude as a result of the amplitude shaping terms $(\mathbf{\Gamma}^H\mathbf{\Gamma})^{-1}$ and $(\mathbf{G}^H\mathbf{G})^{-1}$ in equation 3.4. By using the fact that the desired signal has the strongest amplitude in the shot gather, an iterative scheme which is similar to the one by Mahdad et al. (2011) is applied to obtain the deblended and deghosted shot record of the left source (Figure 3.1c). The notches in the f-k spectrum of the pseudo-deblended data are recovered (Berkhout and Blacquiere, 2014), though one can still observe a small imprint of blending in the f-k spectrum of the deblended shot. For the right source which is not displayed, the pseudo-deblended data and the deblending result have the same behaviour. This example shows that it is possible to deblend by using only the source ghost, without involving any temporal source code.

To illustrate the concept of using the source ghost in conjunction with temporal source encoding, we present an example where two blended sources are both activated

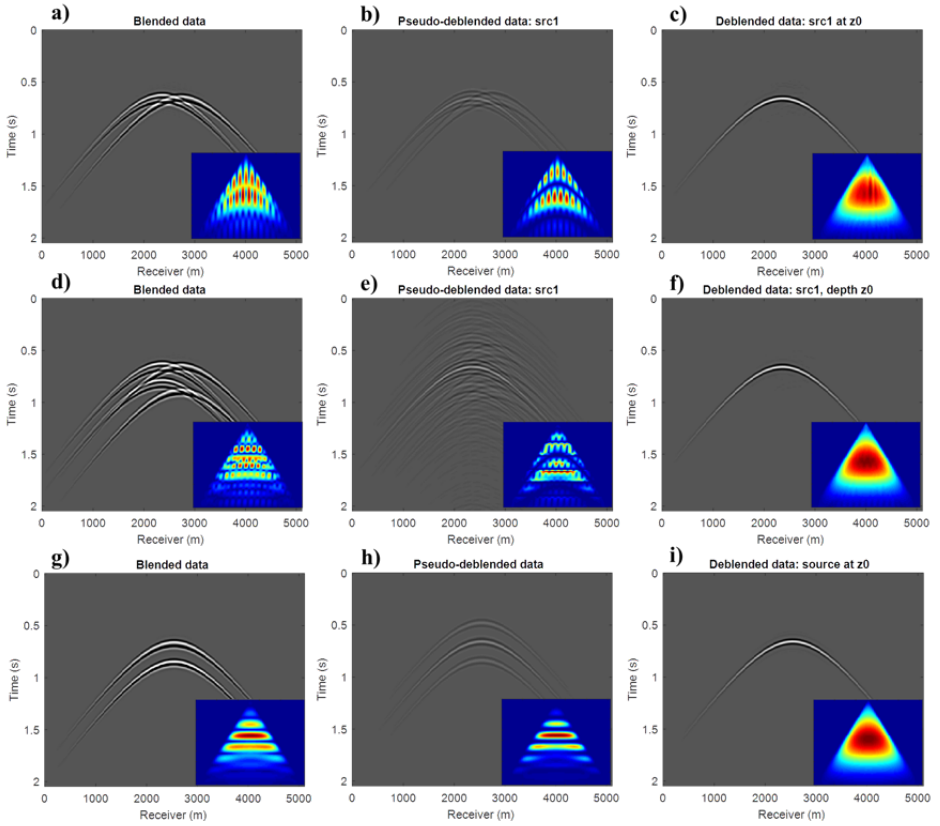


Figure 3.1: Three examples of blending two sources that are towed at different depths. The top row displays the case of blending with source ghosts: a) blended data, b) pseudo-deblended left source, c) deblended and deghosted left source. The middle row displays the case of blending two sources that are towed at different depths with shot repetition encoding: d) blended data, e) pseudo-deblended left source, f) deblended and deghosted left source. The bottom row displays the case of blending multi-level sources that have the same lateral location: g) blended data, h) pseudo-deblended data, i) deblended and deghosted source.

twice with certain time delays. The blended shot record is displayed in Figure 3.1d. After pseudo-deblending, again the left source signal has a higher amplitude than the dispersed right source (Figure 3.1e), and the side lobes of the signal are dispersed due to the shot-repetition code. Compared with the previous case, the signal to blending noise ratio in the pseudo-deblended data is higher and also the result in Figure 3.1f shows a better recovered f-k spectrum. This example demonstrates that with a more sophisticated temporal source code, it is possible to improve the deblending and deghosting result. Note that the inclusion of the temporal source code can be easily implemented by modifying the blending matrix in the forward model.



The third example constitutes of sources at the same lateral location but different depths (Figure 3.1g). This means that instead of manually activating the source twice, an extra physical source is added and allocated at a different depth. In Figure 3.1h, the signal in the pseudo-deblended data contains the contribution of four responses, i.e. two sources and their corresponding ghosts. The deblended and deghosted shot is shown in Figure 3.1i. The f-k spectrum of the result is again notch free. This example demonstrates an alternative method to deal with the current depth-distributed sources. A field data example of this case will be discussed in the following section.

## 3.3. EXAMPLE ON FIELD DATA

We tested the method on field data acquired in the Møre margin high, Norwegian sea. Two identical sub-sources are deployed with random time delays and located at the same lateral position and different depth at 10 m and 14 m. The streamers are located at a depth of 25 m with the receiver spacing being 12.5 m. The data is interpolated to have denser spatial sampling, and a simple receiver deghosting process has been applied. Additionally a time window that mutes both direct waves is applied. Figure 3.2a illustrates the blended shot gather with two overlapping shots that both contain source ghosts, and Figure 3.2c shows its f-k spectrum with frequencies up to 60 Hz. With a source at depth 14 m we normally expect the first source ghost notch at around 53 Hz. The reason that we don't observe this source ghost notch is that this notch is filled up by the overlapping shot at a depth of 10m. The horizontal notches are a result of vertical blending.

Figure 3.2b shows the deblended and deghosted data. From offset 0 to 6000 m, the shot is separated quite well, including the later weak events around 10 s. From offset 6000 m to 10000 m, some parts of the interfering shot are not completely removed, see e.g. the erroneous events that appear to be faster than the water bottom reflection. It is likely because of the small phase difference between the 10 m and the 14 m source and both their ghosts for high-angle events. After deblending, the source ghost has been removed which results in a higher resolution, see Figure 3.2b. The f-k spectrum of the deblended shot has no ghost notch at around 53 Hz and shows a reasonable recovering of low frequencies (Figure 3.2d). The horizontal notches have been mostly recovered, though it shows again the difficulty of recovering the events at high angles.

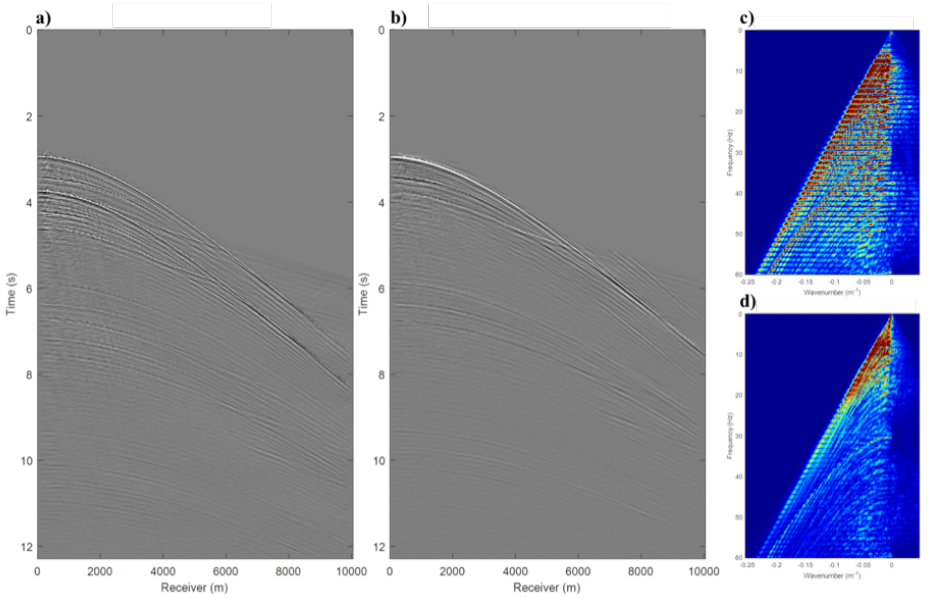


Figure 3.2: a) A shot gather of blended multi-level source field data; b) the deblended and deghosted data; c) the f-k spectrum of a); and d) the f-k spectrum of b).

## 3.4. CONCLUSION

In a blended acquisition, source encoding is needed. The ghost, as a result of the strong sea reflectivity, has a phase difference with respect to the real source, which depends on the tow-depth. Therefore, it can be considered a source code, which can benefit the deblending process. It is possible to use the source ghost as a type of source encoding for deblending purposes. In addition, the combination of a more sophisticated temporal source code and the source code in depth can improve the results and can be easily implemented. In the case where physical sources are situated at different depths, we consider our method as an interesting alternative to obtain a broadband solution. The test on field data shows promising results.

# II

# Part II: Target-oriented acquisition geometry optimisation

# 4

# FOCAL BEAM ANALYSIS WITH PRIMARY WAVEFIELDS

*Focal beam analysis is a model-based acquisition analysis tool. It shows the influence of the acquisition geometry on image quality by image resolution and angle-dependent illumination information. We use it to compute the illumination quality criteria in our acquisition design method. In this chapter, we review the formulation of focal beam analysis with respect to primary wavefields in preparation for solving the inverse problem.*

Part of this chapter is under revision for publication in Geophysical Journal International.

## 4.1. CONVENTIONS OF THE OPERATOR NOTATION

We use a matrix-based operator notation to formulate the focal beam analysis (Berkhout, 1982):

- Matrices are indicated with capital bold symbols, e.g. $\mathbf{P}$.
- Vectors that are part of a matrix are indicated by capital bold symbols with subscript. The distinction between a row vector and a column vector is made by adding a dagger superscript (†) when the vector is a row vector:

  $\mathbf{P}_j$ is the $j^{th}$ column of matrix $\mathbf{P}$.

  $\mathbf{P}_j^\dagger$ is the $j^{th}$ row of matrix $\mathbf{P}$.
- An element of the matrix is indicated by adding two subscripts which indicate the indexes of row and column: $\mathbf{P}_{ij}$ is the element on the $i^{th}$ row and $j^{th}$ column of matrix $\mathbf{P}$.

## 4.2. MATRIX REPRESENTATION OF PRIMARY SEISMIC DATA

Seismic wavefield propagation can be described by matrix operators (Berkhout, 1982). This is a discretised approach to represent the continuous wave field and the related operators in the space frequency domain. In this representation, each monochromatic component of the recorded primary wavefield can be formulated as:

$$\mathbf{P}(z_0;z_0) = \mathbf{D}(z_0) \sum_{m=1}^{M} [\mathbf{W}(z_0,z_m)\mathbf{R}(z_m)\mathbf{W}(z_m,z_0)]\mathbf{S}(z_0), \tag{4.1}$$

where $z_0$ represents the depth level of acquisition surface and $z_m$ represents the depth level in the subsurface model where the waves are reflected. The matrices in equation 4.1 have the following meaning:

- $\mathbf{P}(z_0;z_0)$: the so-called data matrix, where a column $\mathbf{P}_j$ represents the $j^{th}$ common shot gather and a row $\mathbf{P}_j^\dagger$ represents the $j^{th}$ common receiver gather.
- $\mathbf{S}(z_0)$: the source matrix, containing the source wavelet and the spatial location for a source at depth $z_0$. Each column represents the experiment number and each row represents the lateral source (array) location.
- $\mathbf{W}(z_m,z_0)$, forward downward wavefield propagation matrix. Each column contains a discretised vertical derivative of a Green's function, describing wave propagation from one grid point at surface level $z_0$ to many grid points at depth level $z_m$. There are no transmission effects included in this $\mathbf{W}$ operator.
- $\mathbf{R}(z_m)$: reflectivity matrix, describing the conversion of an incident wavefield into a reflected wavefield due to inhomogeneities at depth level $z_m$. It is a diagonal matrix when representing angle-independent reflectivity, and it has nonzero values on both diagonal and off-diagonals when representing angle-dependent reflectivity.

- $\mathbf{W}(z_0, z_m)$: forward upward wavefield propagation matrix. Each column contains a discretized vertical derivative of a Green's function, describing wave propagation from one grid point at the reflection level $z_m$ to many grid points at the acquisition surface $z_0$. There are no transmission effects included in this **W** operator.

- $\mathbf{D}(z_0)$: the receiver matrix. Each column represents the lateral receiver (array) location and each row represents the receiver (array) number.

Note that this matrix notation can represent both 2D and 3D seismic data, where in the case of 3D, each matrix column corresponds to a wavefield or an operator related to one seismic experiment for all lateral locations concatenated in one long vector (Kinneging et al., 1989). Based on the above notation, we write the forward model of focal beam analysis with respect to primary wavefield in the following sections.



## 4.3. IMAGING BY DOUBLE FOCUSING

In seismic imaging, we can retrieve the angle-averaged reflectivity for structural imaging, and we can also obtain the angle-dependent reflectivity for deriving detailed velocity and density information in stratigraphic inversion. Figure 4.1a shows a schematic illustration of the angle-averaged reflectivity matrix, where the black dots represent the nonzero diagonal elements. The angle-dependent reflectivity matrix has nonzero values on both its diagonal and off-diagonals. Figure 4.1b shows a schematic illustration of the angle-dependent reflectivity matrix, where the wavelet-shape curve in each column represents the spatial convolution operator that describes the angle-dependent reflection at a lateral location $j$.

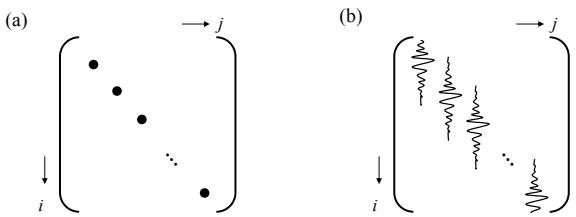


Figure 4.1: Schematic illustrations of (a) the angle-averaged reflectivity matrix, where the black dots represent the nonzero diagonal elements, and (b) the angle-dependent reflectivity matrix, where the wavelet-shape curve in each column represents the spatial convolution operator that describes the angle-dependent reflection at a lateral location $j$.

### 4.3.1. ANGLE-AVERAGED REFLECTIVITY

For structural imaging, to get the reflectivity at a grid point, the essential step of prestack migration is carried out via double focusing. The estimate of angle-averaged reflectivity

of grid point $i$ at depth level $z_m$ can be formulated as:

$$\mathbf{P}_{ii}(z_m; z_m) = \mathbf{F}_i^{\dagger}(z_m, z_0)\mathbf{P}(z_0; z_0)\mathbf{F}_i(z_0, z_m), \tag{4.2}$$

where $\mathbf{P}(z_0; z_0)$ represents the seismic data recorded at the surface; the focusing operator $\mathbf{F}$ is approximated as the transposed complex conjugate (Hermitian) of the forward extrapolation operator $\mathbf{W}$; the row vector $\mathbf{F}_i^{\dagger}$ and the column vector $\mathbf{F}_i$ focus the wavefield at the surface to the target location $i$; and $\mathbf{P}_{ii}(z_m; z_m)$ is the focused wavefield at the target location $i$. Assuming perfect source and receiver sampling, we can obtain:

$$\mathbf{P}_{ii}(z_m; z_m) = \mathbf{R}_{ii}(z_m; z_m) + \epsilon_{ii}(z \neq z_m), \tag{4.3}$$

where $\mathbf{R}_{ii}(z_m)$ is the angle-averaged reflectivity at lateral location $i$ on depth level $z_m$, and $\epsilon_{ii}(z \neq z_m)$ is the contribution from other depth levels. Summing over all frequency components, i.e. applying the imaging condition by selecting $t = 0$ s, we can obtain $\mathbf{R}_{ii}(z_m, z_m)$. A complete image of the subsurface model can be obtained by applying the focusing operators to every grid point at all depth levels.



### 4.3.2. ANGLE-DEPENDENT REFLECTIVITY

For retrieving the angle-dependent reflection coefficient, a process in combination of applying the focusing operator and the Radon transformation is required (De Bruin et al., 1990). The angle-dependent reflectivity for a grid point $j$ can be obtained by:

$$\mathbf{P}_j(z_m; z_m) = \mathbf{F}(z_m, z_0)\mathbf{P}(z_0; z_0)\mathbf{F}_j(z_0, z_m), \tag{4.4}$$

where $\mathbf{P}(z_0; z_0)$ represents the seismic data recorded at the surface; $\mathbf{F}_j(z_0, z_m)$ focuses the data from the source side to the grid point $j$; $\mathbf{F}(z_m, z_0)$ focuses the data from the receiver side to a range of lateral locations $i$ around the grid point $j$; and $\mathbf{P}_j(z_m; z_m)$ is the focused wavefield containing the angle-dependent reflection coefficient at grid point $j$ at depth level $z_m$. Assuming perfect source and receiver sampling, we can obtain:

$$\mathbf{P}_{ij}(z_m; z_m) = \mathbf{R}_{ij}(z_m; z_m) + \epsilon_{ij}(z \neq z_m), \tag{4.5}$$

where $\mathbf{R}_{ij}(z_m; z_m)$ is the element of the angle-dependent reflection coefficient, and $\epsilon_{ij}(z \neq z_m)$ represents the contribution from other depth levels since the data $\mathbf{P}(z_0; z_0)$ contains reflections from other depth levels. After Radon transformation, the angle-dependent reflection coefficients for the lateral location $j$ can be found at the zero-intercept time (De Bruin et al., 1990; Van Wijngaarden, 1998).

## 4.4. FOCAL BEAM ANALYSIS

Acquisition geometries are imperfect in practice. Correspondingly, the receiver and source matrices $\mathbf{D}$ and $\mathbf{S}$ are not identity matrices. After the focusing step, the influence of the acquisition geometry is still in the retrieved grid point response. Focal beam analysis is a model-based acquisition analysis method that can quantify this influence in terms

of the focal source and receiver beams separately, as well as the focal functions that assess the image resolution and angle-dependent amplitude information (Berkhout et al., 2001; Volker et al., 2001; Van Veldhuizen et al., 2008; Kumar et al., 2016).

### 4.4.1. FOCAL BEAMS

When considering only one depth level $z_m$, combining equation 4.1 and equation 4.2, gives the following expression:

$$\mathbf{P}_{ii}(z_m; z_m) = \mathbf{F}_i^{\dagger}(z_m, z_0)\mathbf{D}(z_0)\mathbf{W}(z_0, z_m)\mathbf{R}(z_m)\mathbf{W}(z_m, z_0)\mathbf{S}(z_0)\mathbf{F}_i(z_0, z_m). \tag{4.6}$$

All terms on the right hand side of the reflectivity matrix concern only the seismic experiment on the source side, and all terms on the left hand side concern only the seismic experiment on the receiver side. For a specific target point $k$ and stationary geometries, we can define the focal beams by setting $i = k$. The focal source beam $\mathbf{S}_k$ and the focal receiver beam $\mathbf{D}_k^{\dagger}$ as vectors in the spatial domain can be written as:

$$\mathbf{S}_k(z_m) = \mathbf{W}(z_m, z_0)\mathbf{S}(z_0)\mathbf{F}_k(z_0, z_m), \tag{4.7}$$

and

$$\mathbf{D}_k^{\dagger}(z_m) = \mathbf{F}_k^{\dagger}(z_m, z_0)\mathbf{D}(z_0)\mathbf{W}(z_0, z_m). \tag{4.8}$$

The source beam shows how well the sources can be focused to a single point, and the receiver beam shows how well the receivers can detect the wavefield reflected at a single point. In the case of perfect sampling, the receiver and source matrices are identity matrices. Consequently, the resulting beams are vectors, where the $k^{th}$ element is the only nonzero element and has the value of one. However, acquisition geometries are imperfect in practice due to rough terrain and financial budgets. Correspondingly, the receiver and source matrices **D** and **S** are not identity matrices. After the focusing step, the influence of the acquisition geometry is still in the estimated reflectivity. So with the known propagation and focusing operator, we can quantitatively evaluate the acquisition influence from the receiver and source geometry by focal beams.

### 4.4.2. FOCAL FUNCTIONS

Focal functions —the resolution function and the Amplitude-Versus-ray Parameter (AVP) function —are defined to evaluate the combined influence from source and receiver geometries.

#### RESOLUTION FUNCTION

The resolution function is defined as the confocal image of a unit point diffractor at the target location (Volker et al., 2001). The response of a unit point diffractor $k$ measured at the surface can be formulated as:

$$\delta_k\mathbf{P}(z_0; z_0) = \mathbf{D}(z_0)\mathbf{W}(z_0, z_m)\mathbf{I}_k\mathbf{I}_k^{\dagger}\mathbf{W}(z_m, z_0)\mathbf{S}(z_0), \tag{4.9}$$

where $\delta$ indicates that the wavefield is related to a unit point. The reflectivity matrix is represented by the product of $\mathbf{I}_k$ and $\mathbf{I}_k^\dagger$, which are the $k^{th}$ column and the $k^{th}$ row of the identity matrix $\mathbf{I}$, respectively. Since we assume a unit point diffractor, the reflectivity matrix has the value one at the only nonzero element at the $k^{th}$ lateral location. Combining equation 4.2 and 4.9, the double focusing result of the data $\delta_k\mathbf{P}(z_0;z_0)$ gives:

$$\delta_k\mathbf{P}_{ii}(z_m;z_m) = \mathbf{F}_i^\dagger(z_m,z_0)\delta_k\mathbf{P}(z_0;z_0)\mathbf{F}_i(z_0,z_m), \tag{4.10}$$

$$= [\mathbf{F}_i^\dagger(z_m,z_0)\mathbf{D}(z_0)\mathbf{W}_k(z_0,z_m)][\mathbf{W}_k^\dagger(z_m,z_0)\mathbf{S}(z_0)\mathbf{F}_i(z_0,z_m)], \tag{4.11}$$

where the index $i$ varies around the target point $k$. From the definition of focal beams in equations 4.7 and 4.8, the above equation can be written as:



$$\delta_k\mathbf{P}_{ii}(z_m;z_m) = \mathbf{D}_{ik}(z_m)\mathbf{S}_{ki}(z_m), \tag{4.12}$$

where $\mathbf{S}_{ki}$ and $\mathbf{D}_{ik}$ are the $i^{th}$ elements of the source and receiver beams, respectively; $\delta_k\mathbf{P}_{ii}$ is the $i^{th}$ element of the resolution function. This equation indicates that the resolution function can be obtained by an element-by-element multiplication of the source and receiver beam in the space-frequency domain:

$$diag\{\delta_k\mathbf{P}(z_m;z_m)\} = \mathbf{D}_k^{\dagger,T}(z_m)\circ\mathbf{S}_k(z_m), \tag{4.13}$$

where $\circ$ denotes the element-wise multiplication, and $diag\{\cdot\}$ denotes the diagonal elements of a matrix; therefore, $diag\{\delta_k\mathbf{P}(z_m;z_m)\}$ represents the resolution function related to the target point $k$. The resolution function shows the combined imprint of the source and receiver geometry in the spatial domain. Two attributes of the resolution function are the peak amplitude and the width of the main peak. Side lobes are related to spatial aliasing. Note that here the formulation is for a single frequency component. The broadband resolution function is obtained by summing over all monochromatic resolution functions, that is to say, applying an imaging condition.

#### ANGLE-VERSUS-RAY-PARAMETER FUNCTION

The bifocal image of an angle-independent unit reflector at depth $z_m$ in the linear Radon domain is defined to be the Angle-Versus-ray-Parameter (AVP) function. The response of a unit plane reflector at depth $z_m$ measured at the surface can be formulated as:

$$\Delta\mathbf{P}(z_0;z_0) = \mathbf{D}(z_0)\mathbf{W}(z_0,z_m)\mathbf{I}\mathbf{W}(z_m,z_0)\mathbf{S}(z_0), \tag{4.14}$$

where $\mathbf{I}$ is an identity matrix; $\Delta$ indicates that the wavefield is related to a unit plane reflector. The double focusing result of the data $\Delta\mathbf{P}(z_0;z_0)$ gives:

$$\Delta\mathbf{P}_{ik}(z_m;z_m) = \mathbf{F}_i^\dagger(z_m,z_0)\Delta\mathbf{P}(z_0;z_0)\mathbf{F}_k(z_0,z_m), \tag{4.15}$$

$$= [\mathbf{F}_i^\dagger(z_m,z_0)\mathbf{D}(z_0)\mathbf{W}(z_0,z_m)][\mathbf{W}(z_m,z_0)\mathbf{S}(z_0)\mathbf{F}_k(z_0,z_m)], \tag{4.16}$$

where the index $i$ varies around the target point $k$. From the definition of focal beams in equations 4.7 and 4.8, the above equation can be written as:

$$\Delta \mathbf{P}_{ik}(z_m; z_m) = \mathbf{D}_i^{\dagger}(z_m)\mathbf{S}_k(z_m). \tag{4.17}$$

Equation 4.17 shows that the $(i,k)^{th}$ element of the bifocal image is given by a matrix multiplication of the receiver beam for location $i$, and the source beam for location $k$ in the spatial domain. For all grid points $i$ around the target $k$, the bifocal image can be written as:

$$\Delta \mathbf{P}_k(z_m; z_m) = \mathbf{D}(z_m)\mathbf{S}_k(z_m), \tag{4.18}$$

where $\mathbf{D}(z_m)$ is a matrix where each row is a vector $\mathbf{D}_i^{\dagger}$ —the focal receiver beam for the $i^{th}$ grid point around $k$. This shows that the bifocal image for grid point $k$ is obtained by using one focal source beam for target $k$, and many focal receiver beams for all grid points $i$. For computation efficiency, we assume local homogeneity around target $k$ such that the focal receiver beams $\mathbf{D}_i^{\dagger}$ for all grid points are identical to $\mathbf{D}_k^{\dagger}$ (Van Veldhuizen, 2006). Thus, the elements of $\Delta \mathbf{P}_k$ can be expressed as the spatial convolution of $\mathbf{D}_k$ and $\mathbf{S}_k$. Therefore, the AVP function $\Delta \tilde{\mathbf{P}}_k$ can be approximated as an element-wise multiplication in the linear Radon domain:

$$\Delta \tilde{\mathbf{P}}_k(z_m; z_m) = \tilde{\mathbf{D}}_k(z_m) \circ \tilde{\mathbf{S}}_k(z_m), \tag{4.19}$$

where $\tilde{\mathbf{D}}_k$ and $\tilde{\mathbf{S}}_k$ are the focal receiver and source beams in the linear Radon domain, respectively. The AVP function shows how the acquisition geometry influences the angle-dependent information of the target. The attributes of the AVP function are spatial bandwidth and spectral completeness. The broadband AVP function is obtained by summing the monochromatic AVP functions along lines of constant ray parameter (Van Veldhuizen, 2006).

### 4.4.3. IMPLEMENTATION OF FOCAL BEAM ANALYSIS

We use a simple 3D velocity model to illustrate the focal beam analysis method. The frequency range is chosen as 5 to 40 Hz. The velocity model with a salt body is displayed in Figure 4.2a and a target point is located at $(x_1, x_2, z)$ =(1500 m, 1500 m, 525 m). For the chosen target point, the receiver and source geometries shown in Figure 4.2b are assessed, and the broadband focal beam analysis results are shown in Figure 4.3. The focal receiver and source beams can show the detecting and focusing abilities of the receiver and source geometries separately in the spatial domain (Figure 4.3a and b) and in the linear Radon domain (Figure 4.3d and e). The resolution function in Figure 4.3c is the element-wise multiplication of the focal beams in the spatial domain. The AVP function in Figure 4.3f is the element-wise multiplication of the transposed focal receiver beam in Figure 4.3d and the focal source beam in Figure 4.3e in the linear Radon domain.

The acquisition geometry in Figure 4.2b is a typical orthogonal land acquisition geometry, where the receiver line interval is 200 m and the source line interval is 100 m. Due to the large receiver and source line intervals, the focal receiver beam has side lobes in the $x_2$-direction and the focal source beam has side lobes in the $x_1$-direction in the spatial domain. By virtue of the orthogonal aliasing directions in receiver and source

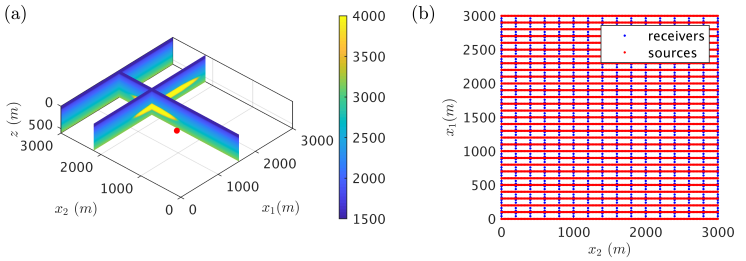


Figure 4.2: (a) A 3D velocity model with a target point located at (1500 m, 1500 m, 525 m). (b) An example acquisition geometry, where the blue dots represent the receivers and the red dots represent the sources.



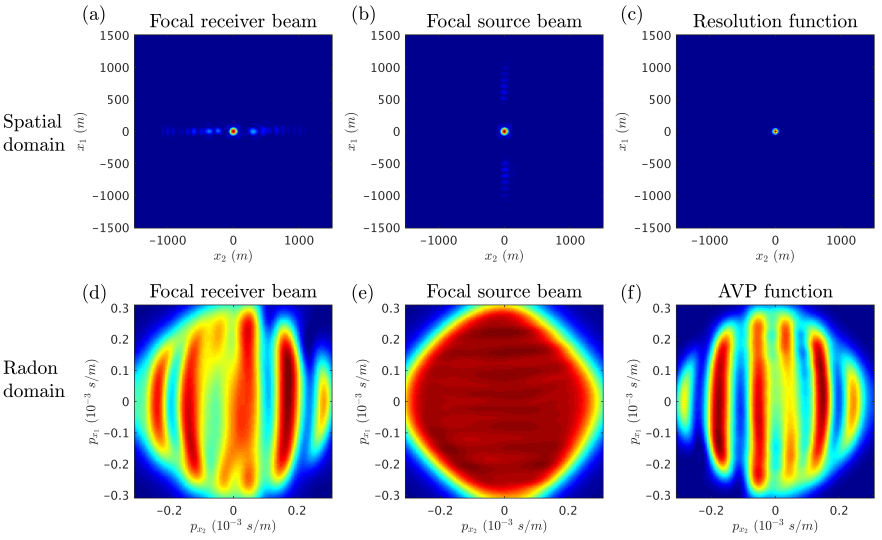


Figure 4.3: Broadband focal beam analysis result of the example geometry: (a) focal receiver beam in the spatial domain, (b) focal source beam in the spatial domain, (c) resolution function, (d) focal receiver beam in the linear Radon domain, (e) focal source beam in the linear Radon domain, and (f) AVP function.

crosslines, the aliasing effects cancel out in the resolution function, which shows a desired spiky peak in Figure 4.3c. Figure 4.3d shows missing angles because the receivers are sparsely sampled in the $x_2$-direction. The focal source beam in Figure 4.3e shows a full angle coverage and no missing angles because the source sampling in the $x_1$-direction is sufficient. However, the resulting AVP function has missing angles since it shows the combined influence from both source and receiver geometries. From the results, it is straightforward to conclude that the receiver geometry needs to be improved if a full angle coverage is desired at the target point.

## 4.5. IMAGING V.S. FOCAL BEAM ANALYSIS

Focal beam analysis provides the focal beams and the focal functions. Computing the focal functions can be thought of as imaging of the target point, where a double focusing procedure is carried out. A velocity model is needed to calculate the propagation and the focusing operators.

In imaging, the unknown parameter is reflectivity. We estimate it by removing the propagation effect and the sampling operators. In focal beam analysis, we assume that the reflectivity is known as a grid point response or unit reflector response. Therefore, the resulting focal functions —the confocal and bifocal imaging results of the target —reveal the influence of the sampling operators on the image, instead of the reflectivity.

In this chapter, we have shown how the quality of the receiver and source sampling geometries can be evaluated via focal beam analysis. In an acquisition design problem, the unknown parameters are the sampling operators. In the next chapter, we will quantify the illumination quality criteria defined by focal functions, and solve the unknown sampling operators via optimisation.

# 5

# OPTIMISING THE RECEIVER GEOMETRY: A GRADIENT DESCENT METHOD

*Optimising the acquisition geometry is the inverse problem of acquisition analysis, where the unknown is the sampling geometry. In the previous chapter, we reviewed the forward model of focal beam analysis. In this chapter, we solve the inverse problem by using a gradient descent method, where we aim to update the receiver geometry for an optimum target illumination.*

Part of this chapter is under revision for publication in Geophysical Journal International.

## 5.1. ACQUISITION DESIGN AS AN OPTIMISATION PROCESS

Acquisition design can be solved as an optimisation problem (Liner et al., 1998). In the previous chapter, we reviewed the forward model of focal beam analysis. There are seven aspects that can influence the focal beam result, that is to say, the target location, the velocity model, frequency range, the wavefield modelling and migration operators, and the source as well as receiver sampling on the acquisition surface. To reduce the inversion parameters, we assume the velocity model is known as *a priori* knowledge, and allow the parameters—the target, frequency range, the wavefield modelling and migration operators—be user-defined in advance.

A flowchart of the optimization method is shown in Figure 5.1, where the steps in the green boxes are the input, and the step in the yellow box is updating the acquisition geometry. The focal functions are computed for each updated geometry, and compared to the requirement. Ideally, the updating process stops when the focal functions reach the requirement. The challenges of solving this optimisation problem are: large amount of parameters, nonlinearity, and high computation cost. We will address these aspects in the following sections.



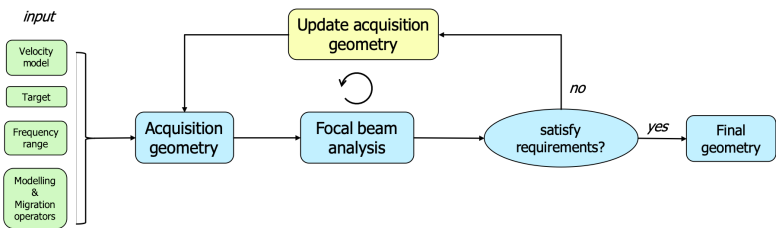


Figure 5.1: A workflow of optimising the acquisition geometry for target illumination.

### 5.1.1. PARAMETERISATION

A geometry optimisation where all spatial sampling locations are independent parameters is a very nonlinear problem which is difficult to solve. For instance, Araya-Polo et al. (2016) describe a sub-modular optimisation algorithm, and Latiff et al. (2017) describe a particle swarm algorithm to optimise the acquisition parameters. Both types of methods face the challenges of the large amount of parameters and the nonlinearity of the design problem. Research has shown that global optimisation algorithms are effective for solving nonlinear problems; however, the computation costs remain high. Linearised optimisation algorithms are fast. However, linearisation between the sampling parameters and the illumination criteria is non-trivial since the sampling parameters are the spatial coordinates of the sampling points.

To linearise the acquisition design problem, we use a two-step parameterisation strategy. First, the sampling density, which is defined as the number of sampling points per unit area, is chosen as the continuous parameter of the inverse problem. Second, we transform the density distribution into a realization of a sampling geometry via the weighted centroidal Voronoi diagram (Secord, 2002). In a 2D space, the Voronoi diagram

partitions the plane into regions based on the weight given by the continuous density function; the centroids of the Voronoi cells are then the sampling locations; this process can be done by the Lloyd's algorithm (see Okabe et al., 2009, for more details). Thus, this transformation distributes the centroids with a spatial distance that is inversely proportional to the local density value. We can express the discrete receiver and source locations as the following:

$$\mathbf{D} = f(\phi_r(x, y)), \tag{5.1}$$

and

$$\mathbf{S} = f(\phi_s(x, y)), \tag{5.2}$$

where $\phi_r$ and $\phi_s$ represents the sampling receiver and source density at each lateral location$(x, y)$ at the surface, respectively; $f(\cdot)$ denotes the process that turns a density distribution to a discrete set of points representing the sampling geometry; $\phi_r(x, y)$ is normalised such that the sum of $\phi_r(x, y)$ is the total number of sampling points in **D**; $\phi_s(x, y)$ is normalised such that the sum of $\phi_s(x, y)$ is the total number of sampling points in **S**. Figure 5.2a shows a general example of the sampling density, where dark colours represent high values and light colours represent low values. Figure 5.2b shows the sampling map obtained after applying the weighted centroidal Voronoi diagram algorithm. The consequent sampling is dense where the density value is high, and the sampling is sparse where the density value is low.




Figure 5.2: Feature of the sampling density transformation: (a) a horizontal gradient map is transformed to, (b) a set of sampling points whose spatial density distribution is proportional to the input gradient map.

The transformation function has a nondeterministic characteristic: it can generate completely different sampling sets from the same input density distribution, because the transformation algorithm uses a random number generator. On the one hand, this characteristic allows the actual sampling locations to be flexible. The parameter—sampling density—can be seen as a macro solution of the acquisition geometry, which can be used for flexible acquisition systems, regular acquisition systems, and potentially automated devices. On the other hand, this characteristic causes uncertainty in the illumination quality, which is assessed by the focal functions that depend on the realization of the sampling geometry. This aspect will be analysed in the numerical examples. Overall, we are able to linearise the relationship between the parameters and the illumination criteria, by using the continuous density function instead of the spatial coordinates of all individual sampling points as parameters, and by turning the density-to-sampling transformation into a separate step.

### 5.1.2. CONSIDER THE RECEIVER SIDE

To further reduce the inversion parameters, we consider optimising only the receiver geometry when the source geometry is fixed, or vice versa. The scenario of a fixed source geometry is used to formulate the inversion method. The methodology holds likewise for optimising the source geometry with a fixed receiver geometry, because sources and receivers are interchangeable due to reciprocity (Knopoff and Gangi, 1959). The resolution and the angle distribution at the target can be represented by the resolution function and the AVP function, respectively, which were defined in the previous chapter. The reference resolution and AVP function are determined from the full 3D regular source and receiver geometries, which obey the Nyquist sampling criterion. The reference geometry is considered to have the best attainable illumination.

This scenario can be considered as determining an optimum Ocean Bottom Node (OBN) layout in the marine environment subject to a limited amount of OBN's, and assuming a full 3D sampling on the source side. The objective of the simplified problem is to automatically optimise a receiver geometry for a good illumination of the chosen target, as close to the reference focal functions as possible.



### 5.1.3. A FIXED NUMBER OF RECEIVERS

To reduce the nonlinearity of the problem, we fix the total number of receivers, assuming we know the best number of receivers to proceed. In a uniform receiver layout, the illumination quality improves with an increasing amount of receivers until the Nyquist sampling criterion is satisfied. In our set-up, the distribution of receivers can be non-uniform. Therefore, the relationship between the sampling number and the illumination quality is very nonlinear. With each sampling number, there are the optimum geometry and the worst geometry. During updating, a geometry with less sampling points can still be better than a geometry with more sampling points. Below the Nyquist number, we expect that the illumination improves with the increasing number of receivers until the spatial sampling satisfies the Nyquist criterion (Nyquist, 1928), on the condition that the geometry of each sampling number is the optimum.

Despite the nonlinearity, an inversion scheme will update the geometry to one whose sampling number is close to the Nyquist requirement through optimisation, if the number of sampling points is flexible. The choice of using an indefinite number of receivers will be discussed in Chapter 6. For the examples in this chapter, we fix the number of sampling points far below the Nyquist requirement to gain insight into how we can subsample the data below the Nyquist requirement. Therefore, the optimisation problem becomes mathematically not-well defined—there is always an error term remaining—and there exist many geometry solutions of a similar error value. In other words, there is no unique solution. Typically, the amount of stationary equipment is also restricted in practice. In summary, we are dealing with a nonlinear problem with many possible solutions that have the same error.

### 5.1.4. TWO ASPECTS OF ILLUMINATION

The previously described resolution function and the AVP function are used as the illumination criteria. They represent two interconnected aspects of the illumination property. They are used to formulate two individual objective functions detailing the purposes of optimising the image resolution and optimising the angle-dependent information.

#### OPTIMISING THE IMAGE RESOLUTION

To optimise the image resolution, we have the following objective function:

$$J_1 = \sum_{x,y} ||diag\{\delta_k \mathbf{P}(z_m, \phi_{ref})\} - diag\{\delta_k \mathbf{P}(z_m, \phi_r)\}||^2, \tag{5.3}$$

where $diag\{\delta_k \mathbf{P}(z_m, \phi_{ref})\}$ represents the resolution function from the reference receiver density distribution $\phi_{ref}$, which is chosen as a full 3D sampling that satisfies the Nyquist criterion ; $diag\{\delta_k \mathbf{P}(z_m, \phi_r)\}$ represents the resolution function from the receiver density to be optimised, $\phi_r$. Thus it follows that only the image amplitude at target level $z_m$ is considered when comparing to the reference. The gradient required is:

$$\nabla_{\phi_r} J_1 = -2 \sum_{\omega} \mathbf{W}_k(z_0, z_m)[\mathbf{E}_k(z_m) \circ \mathbf{S}_k(z_m)][\mathbf{W}(z_0, z_m)]^H, \tag{5.4}$$

where the residual $\mathbf{E}_k(z_m) = diag\{\delta_k \mathbf{P}(z_m, \phi_{ref})\} - diag\{\delta_k \mathbf{P}(z_m, \phi_r)\}$. The element-wise multiplication of $\mathbf{E}_k(z_m)$ and $\mathbf{S}_k(z_m)$ is a computational simplification of a matrix multiplication, which is originated from the definition of the resolution function in equation 4.12. Combined with the definition of $\mathbf{S}_k(z_m)$ in equation 4.7, the multiplication with the source beam implies that the residual is forward propagated to the surface, sampled by the source geometry, and back propagated to the target. After that, the product $\mathbf{E}_k(z_m) \circ \mathbf{S}_k(z_m)$—the residual now including the source sampling effect—is again forward propagated from the target level to the acquisition surface, then correlated with the upgoing one-way wavefield from the target. At the end, the imaging condition is applied by summing over all frequencies. Note that the objective function and the gradient are formulated for one target point. In the case of multiple target points, the objective function and the gradient are computed by summing over all target points.

#### OPTIMISING THE ANGLE-DEPENDENT INFORMATION

To optimise the angle-dependent information, we have the following objective function:

$$J_2 = \sum_{p_x, p_y} ||\Delta\widetilde{\mathbf{P}}_k(z_m, \phi_{ref}) - \Delta\widetilde{\mathbf{P}}_k(z_m, \phi_r)||^2, \tag{5.5}$$

where $\Delta\widetilde{\mathbf{P}}_k(z_m, \phi_{ref})$ represents the AVP function from the reference receiver density $\phi_{ref}$, and $\Delta\widetilde{\mathbf{P}}_k(z_m, \phi_r)$ represents the AVP function from the variable density $\phi_r$. This criterion means that we consider the angle-dependent imprint that is associated with the target depth level $z_m$ compared to the reference. The reference beam from the full 3D sampling is considered to have the best attainable angle distribution. The gradient required is:

$$\nabla_{\phi_r} J_2 = -2 \sum_{\omega} \mathbf{W}_k(z_0, z_m)[\mathbf{L}^H\{\widetilde{\mathbf{E}}_k(z_m) \circ \widetilde{\mathbf{S}}_k(z_m)\}][\mathbf{W}(z_0, z_m)]^H, \tag{5.6}$$

where the residual $\widetilde{\mathbf{E}}_k(z_m) = \Delta\widetilde{\mathbf{P}}_k(z_m,\phi_{ref}) - \Delta\widetilde{\mathbf{P}}_k(z_m,\phi_r)$, and $\mathbf{L}^H$ represents the inverse linear Radon transform. The element-wise multiplication of the source beam $\widetilde{\mathbf{S}}_k(z_m)$ and the residual $\widetilde{\mathbf{E}}_k(z_m)$ is in the linear Radon domain; therefore, it is a convolution in the spatial domain. Similar to the gradient of optimising the image resolution in equation 5.4, the residual in the Radon domain is combined with the source beam, then transformed to the spatial domain. The gradient is obtained by forward propagation, correlation with the one-way wavefield from the target, and applying the imaging condition. The objective function and the gradient are formulated for one target point. In the case of multiple target points, the objective function and the gradient are computed by summing over all target points.

#### ALGORITHM

We use a gradient descent scheme with a line search procedure to solve the optimisation problem. Since the problem is nonlinear and not-well defined, different initial guesses are used to find the approachable minimum. Initial guesses are chosen as the one-way wavefield amplitude at the acquisition surface, and concentrated circles of different radius above the target. The pseudo-algorithm of geometry optimisation using $J_1$ is given in algorithm 1. Due to the parameterisation approach, the same density distribution can be transformed to different sampling sets that have a range of misfit values and varying gradient. We apply a Gaussian smoothing to the calculated gradient to reduce the dependence of one specific sampling set. In addition, we use a pre-defined maximum number of iterations and select the smallest $J_1(\phi_r^i)$ after the process is finished. At a later stage of the iteration, there is only a small density update, and density can be seen as nearly repeated. Inherently the density is transformed to different geometries that may have different $J_1$ values; therefore, the algorithm accounts for the nondeterministic feature in the parameterisation approach. The algorithm of geometry optimisation using $J_2$ follows the same procedure with the corresponding equations replaced.

**Algorithm 1** Geometry optimisation using $J_1$

**Input:** target location, initial guesses $\phi^0_{r_{1,2,\ldots,N}}$, $i_{max}$, $i = 1$
1: **for** each initial guess **do**
2:  **while** $i \leq i_{max}$ **do**
3:  Transform $\phi_r$ to geometry **D** using the algorithm described in Secord (2002)
4:  Compute resolution function $\delta_k\mathbf{P}(z_m)$ by equation 4.18
5:  Compute objective function $J_1$ by equation 5.3
6:  Compute gradient $\nabla_{\phi_r} J_1$ by equation 5.4, and apply a Gaussian smoothing
7:  Line search procedure, select step size $\alpha$
8:  Update density $\phi_r^{i+1} = \phi_r^i + \alpha\nabla_{\phi_r} J_1$
9:  $i = i + 1$
10:  **end while**
11: **end for**
12: Select density with the lowest $J_1$ value

## 5.2. NUMERICAL EXAMPLES

### 5.2.1. SIMPLE 3D SALT MODEL

A simple 3D velocity model with an ellipsoidal salt body is used to test the method (Figure 5.3). The target point located at a depth of 570 m is indicated by a red dot in the 3D velocity model. For computational efficiency, the frequency range used here is 5 Hz to 10 Hz. Based on the Nyquist criterion, the full 3D geometry that ensures a minimal aliasing effect for the corresponding bandwidth requires roughly 1400 receivers. In this example, the source geometry and the reference receiver geometry are full 3D geometries that satisfy the Nyquist criterion. For geometry optimisation, the receiver number is limited to 100, which is around 7% of the Nyquist requirement. Figure 5.4 shows that the reference resolution function has no side lobes, and the AVP function has a full angle coverage. The AVP function has a non-flat spectrum due to the influence of the salt overburden. We consider that the focal functions from the full 3D sampling on both the source and receiver sides represent the best attainable illumination. We optimise the receiver geometry for a maximum match to the target illumination obtained by the reference receiver geometry by using $J_1$ and $J_2$ separately.



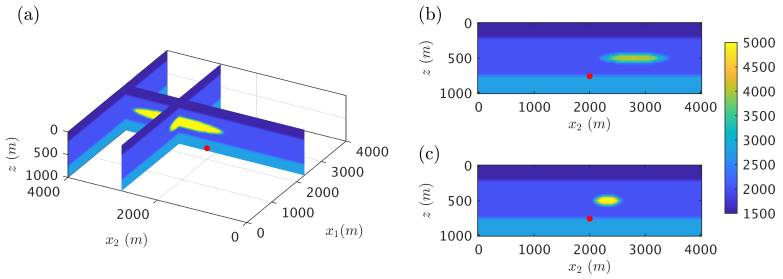


Figure 5.3: (a) 3D velocity model with the target point represented by a red dot, (b)-(c) velocity model cross sections. The spatial coordinate of the target point is (2000 m, 2000 m, 570 m).

Figure 5.5 shows the focal beam analysis results of a uniform geometry with 100 receivers. This represents the conventional scenario since OBN's are typically evenly deployed. Figure 5.5a shows that the acquisition area has a uniform spatial sampling density, which is transformed to the corresponding receiver geometry via the weighted Voronoi algorithm in Figure 5.5b. The consequent resolution function has a sharp peak, see Figure 5.5c and 5.5e; the residual in Figure 5.5g is small with the maximum error being 1% of the scale of the resolution function. The resulting AVP function covers high angles with many azimuths in the middle range missing (Figure 5.5d and f).

Figure 5.6 shows the optimisation results using $J_1$, i.e. using the resolution function as the criterion. Compared to the focal analysis results of the uniform geometry, both the residuals of the resolution function and the AVP function have a lower amplitude (Figure 5.6g and h), although the optimisation scheme only uses the resolution function to compute the update. This is probably because the resolution and AVP functions are two interconnected aspects of the same illumination property. Resolution concerns the

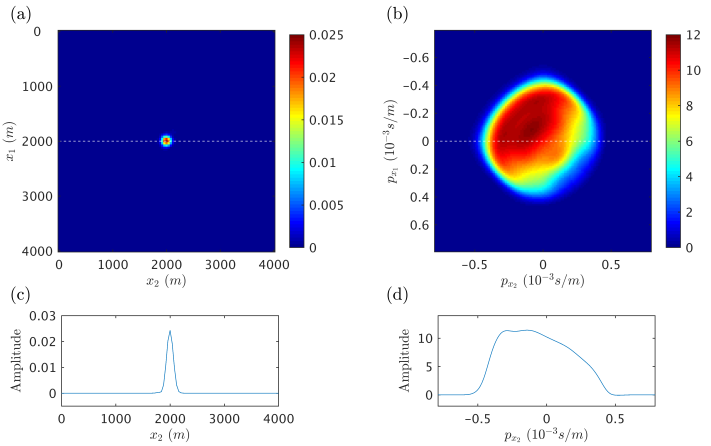


Figure 5.4: (a) Reference resolution function, (b) reference AVP function, (c) a cross section of (a) at $x_1 = 2000$ m, (d) a cross section of (b) at $p_{x_1} = 0$ s/m.



angle-averaged image accuracy, and the AVP function describes the angle-dependent information. Optimising for one could lead to certain improvements in the other criterion. Figure 5.7 shows the optimisation results using $J_2$, where the AVP function is used as the criterion. It is clearly visible that the residual of the AVP function in Figure 5.7h is the lowest compared to the residuals in Figure 5.5h and 5.6h, and the cross section of the AVP function in Figure 5.7f shows the closest match to the reference.

Since the same sampling density distribution can be transformed to different geometry realizations of varying illumination quality, we transform the density distributions in Figure 5.5a, 5.6a and 5.7a each to 100 different geometry realizations, and analyse their variations in $J_1$ and $J_2$ values. Figure 5.8a presents the histograms of $J_1$ values calculated from the 100 geometries that are transformed from the density optimised for $J_1$ (red), the density optimised for $J_2$ (green), and the uniform density (blue). The density optimised for $J_1$ shows an improvement in resolution in general: the red histogram has a lower mean value than the blue histogram; the variation of the red histogram is approximately one third of the variation of the blue histogram; though there is a small overlap between the two histograms. Even though it appears that all density maps have relative large variation in $J_1$ values, the resolution of three density distributions are all close to the reference—there is no visible error in Figure 5.5e, 5.6e and 5.7e. Figure 5.8b presents the histograms of $J_2$ values calculated from the 100 geometries that are transformed from the density optimised for $J_1$ (red), the density optimised for $J_2$ (green), and the uniform density (blue). The density optimised for $J_2$ shows the best angle coverage among the three densities: the mean value of the green histogram is the lowest, and much smaller than the blue histogram; the variation of the green histogram is only ten percent of the variation of the blue histogram. Compared to Figure 5.8a, there is a larger difference when optimising for $J_2$. This makes sense because the resolution is mainly affected by the spatial sampling rate. Since the total amount of sampling points remains the same during optimisation, there is not a large improvement in resolution. Further-

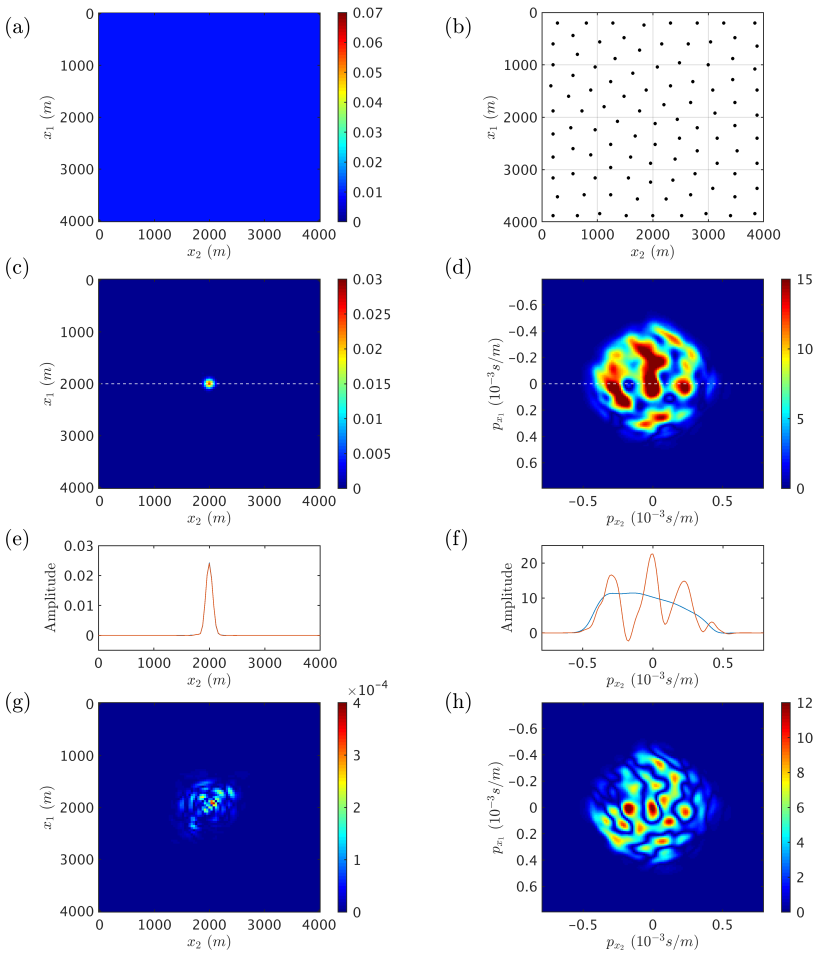


Figure 5.5: Focal beam analysis results of a uniform receiver geometry under the simple salt model: (a) receiver density distribution, (b) receiver geometry, (c) corresponding resolution function, and (d) AVP function. The dashed lines in (c) and (d) indicates the cross section locations of plot (e) and (f). The red line in (e) and (f) represents the evaluated geometry, while the blue line represents the reference geometry. (g)-(h) The residuals of the resolution function and the AVP function respectively, displayed in absolute scale.

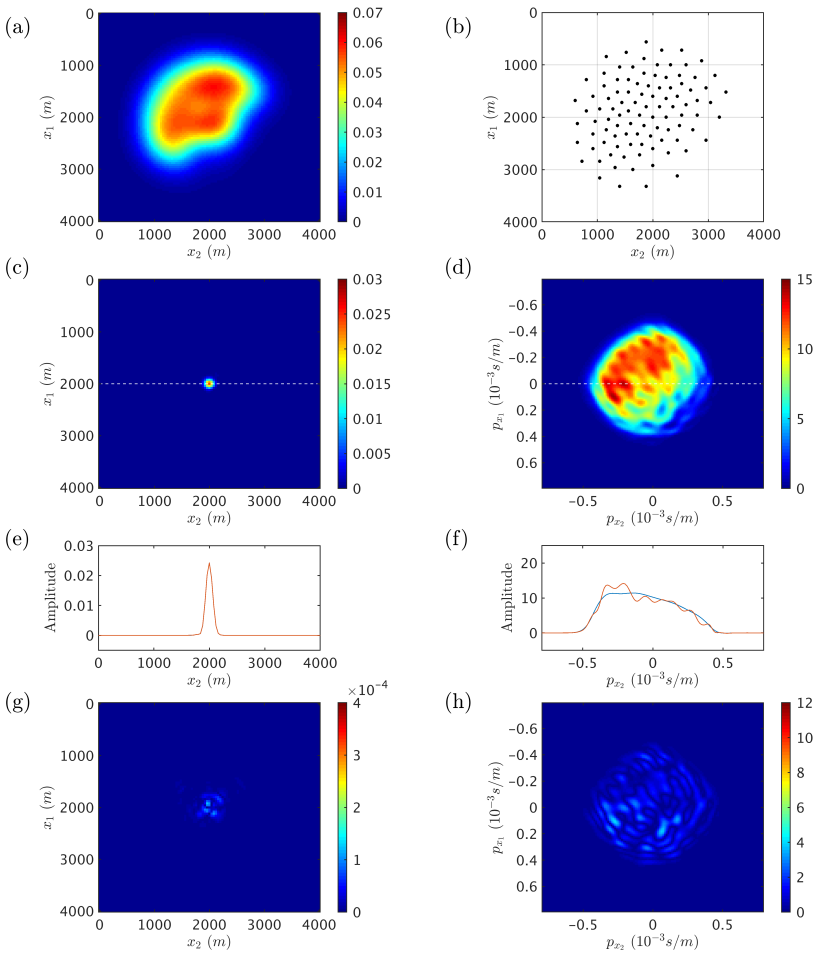


Figure 5.6: Geometry optimisation results using $J_1$ under the simple salt model: (a) optimised receiver density distribution, (b) optimised receiver geometry, (c) corresponding resolution function, and (d) AVP function. The dashed lines in (c) and (d) indicates the cross section locations of plot (e) and (f). The red line in (e) and (f) represents the evaluated geometry, while the blue line represents the reference geometry. (g)-(h) The residuals of the resolution function and the AVP function respectively, displayed in absolute scale.

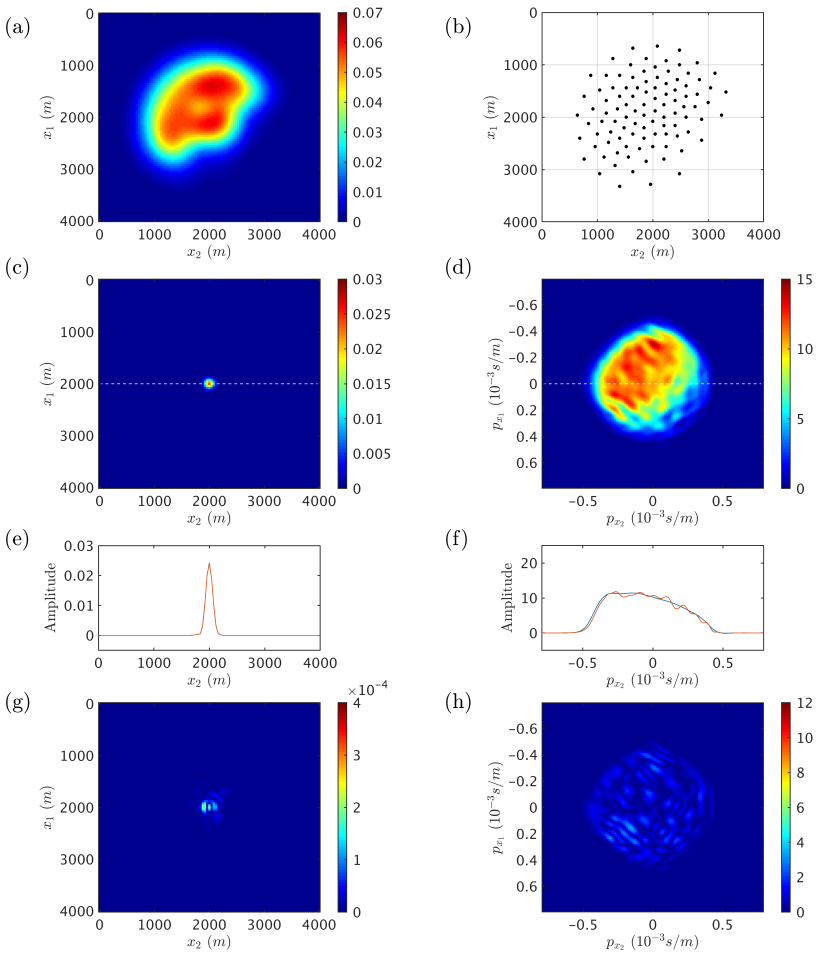


Figure 5.7: Geometry optimisation results using $J_2$ under the simple salt model: (a) optimised receiver density distribution, (b) optimised receiver geometry, (c) corresponding resolution function, and (d) AVP function. The dashed lines in (c) and (d) indicates the cross section locations of plot (e) and (f). The red line in (e) and (f) represents the evaluated geometry, while the blue line represents the reference geometry. (g)-(h) The residuals of the resolution function and the AVP function respectively, displayed in absolute scale.

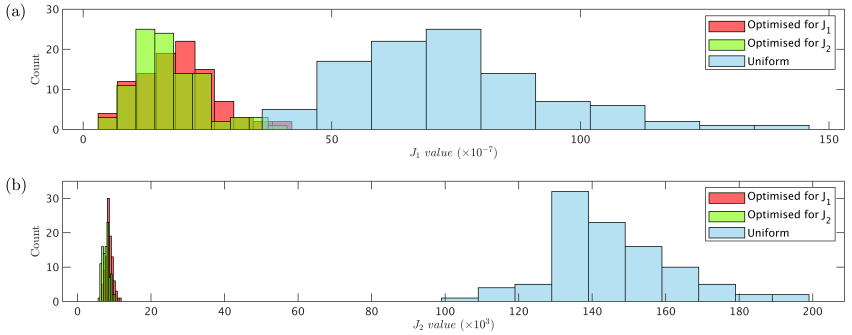


Figure 5.8: (a) Histograms of $J_1$ values of 100 realizations of the receiver density optimised for $J_1$ (red), the density optimised for $J_2$ (green), and the uniform density (blue). (b) Histograms of $J_2$ values of 100 realizations of the density optimised for $J_1$ (red), the density optimised for $J_2$ (green), and the uniform density (blue).



more, the histogram distributions of density optimised for $J_1$ and $J_2$ overlap each other. This is probably because the density maps optimised for $J_1$ and $J_2$ in Figure 5.6a and Figure 5.7a have high resemblances. From this analysis, we conclude that the variation in objective function values due to the specific geometry realization from the same density function will have some impact on the optimisation process, but the effect is acceptable.

The density maps and geometries after optimisation are no longer uniform. The spatial variation in the density map indicates the areas that should have a higher sampling rate and the areas that could have a lower sampling rate. There exist other geometry solutions with similar objective function values, since the optimisation problem is nonlinear and not well-defined. The solution space can be reduced by adding extra constraints such as acquisition deployment preferences. For instance, there might be areas that are restrictive for stationary receivers. The results show that a uniform geometry already satisfies the resolution requirement; the optimisation for $J_1$ improves the resolution in a small scale; a larger improvement is limited by the total amount of sampling points. Optimising for $J_2$ shows a significant improvement in the angle distribution compared to the uniform geometry. The optimised geometries have a better angle coverage on all azimuths, and the spectrum has small fluctuations compared to the reference.

### 5.2.2. SEG/EAGE SALT MODEL

The geometry optimisation scheme is also tested for a subsampled SEG/EAGE salt model (Aminzadeh et al., 1996). The velocity model is shown in Figure 5.9, and the reference focal functions are shown in Figure 5.10. The peak of the resolution function is located at the lateral location of the target. The complex salt overburden has a clear imprint on the AVP function. In this example, the frequency range is 5−10 Hz, and the Nyquist sampling requires roughly 7300 receivers. The source geometry and the reference receiver geometries are full 3D geometries that satisfy the Nyquist criterion. The receiver number is limited to 300, which is around 4% of the Nyquist requirement.

First, we show the focal beam analysis results of a uniform geometry of 300 receivers

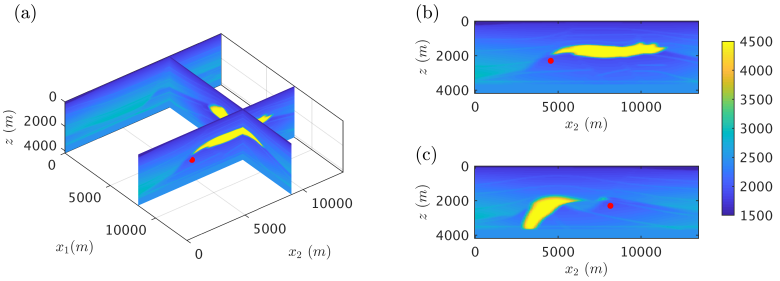


Figure 5.9: (a) 3D SEG/EAGE salt model with the target point represented by a red dot, (b)-(c) velocity model slices where the target is denoted by a red star. The coordinate of the target point is (8160 m, 4560 m, 2300 m).

(Figure 5.11). The resolution function has a sharp peak in Figure 5.11c and e; the misfit in Figure 5.11g is small with the maximum being 0.8% of the scale of the resolution function. However, there are high-amplitude fluctuations in the AVP function compared to the reference (Figure 5.11d and f). Figure 5.12 shows the optimisation results using $J_1$, and Figure 5.13 shows the optimisation results using $J_2$. Comparing the focal functions of these three cases, Figure 5.11g shows the smallest residual of the resolution function; Figure 5.12h shows the smallest residual of the AVP function; the uniform geometry has an acceptable resolution but a high residual in angle coverage.



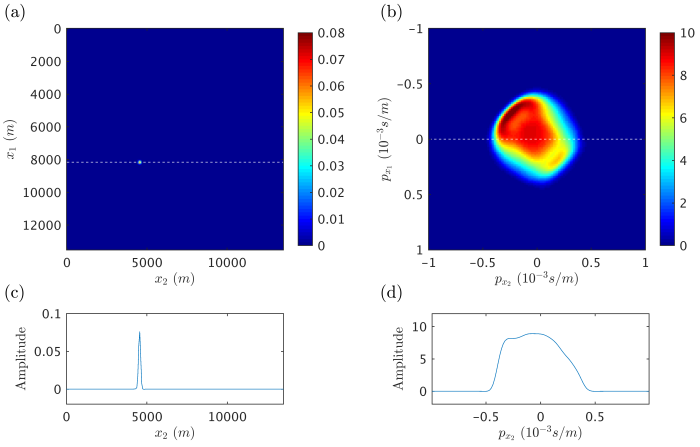


Figure 5.10: (a) Reference resolution function, (b) reference AVP function, (c) a cross section of (a) at $x_1 = 8000$ m, and (d) a cross section of (b) at $p_{x_1} = 0$ s/m.

Because of the uncertainty in illumination quality, again we transform the densities in Figure 5.11a, 5.12a and 5.13a each to 100 geometries and analyse their variations in $J_1$ and $J_2$. Figure 5.14a presents the histograms of $J_1$ values calculated from the 100 geometries that are transformed from the density optimised for $J_1$ (red), the density optimised for $J_2$ (green), and the uniform density (blue). The density optimised for $J_1$ shows a small-scale improvement in resolution: the mean value of the red histogram is the

lowest, though a large portion of it overlaps with the histogram of the uniform density. Note that it may appear that all density maps have relatively large variation in $J_1$ values; however, they all have an acceptable resolution since the error is barely visible when compared to the reference in Figure 5.11e, 5.12e, and 5.13e. Moreover, the $J_1$ values for the density optimised for $J_2$ (green) are larger than those for the uniform density. This means that optimising for angle coverage does not necessarily lead to an optimum image resolution.

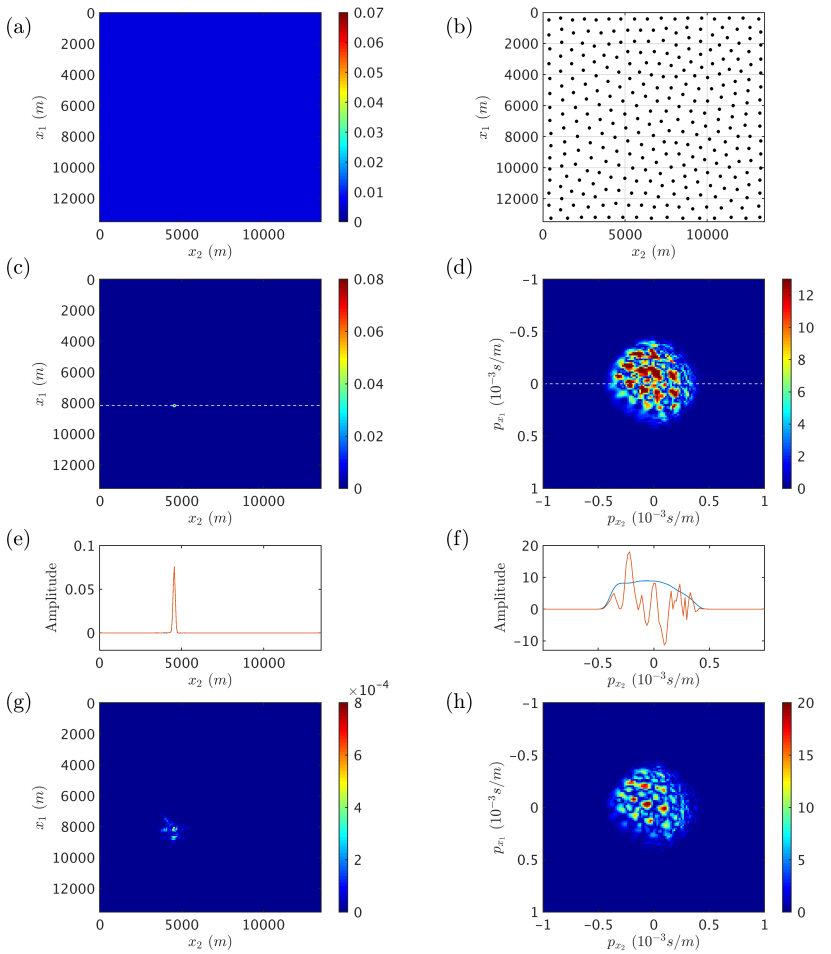


Figure 5.11: Focal beam analysis of a uniform receiver geometry under the SEG/EAGE salt model: (a) receiver density distribution, (b) receiver geometry, (c) corresponding resolution function, and (d) AVP function. The dashed lines in (c) and (d) indicates the cross section locations of plot (e) and (f). The red line in (e) and (f) represents the evaluated geometry, while the blue line represents the reference geometry. (g) and (h) are the residuals of the resolution function and the AVP function respectively, displayed in absolute scale.

Figure 5.14b presents the histograms of $J_2$ values calculated from the 100 geometries that are transformed from the density optimised for $J_1$ (red), the density optimised for

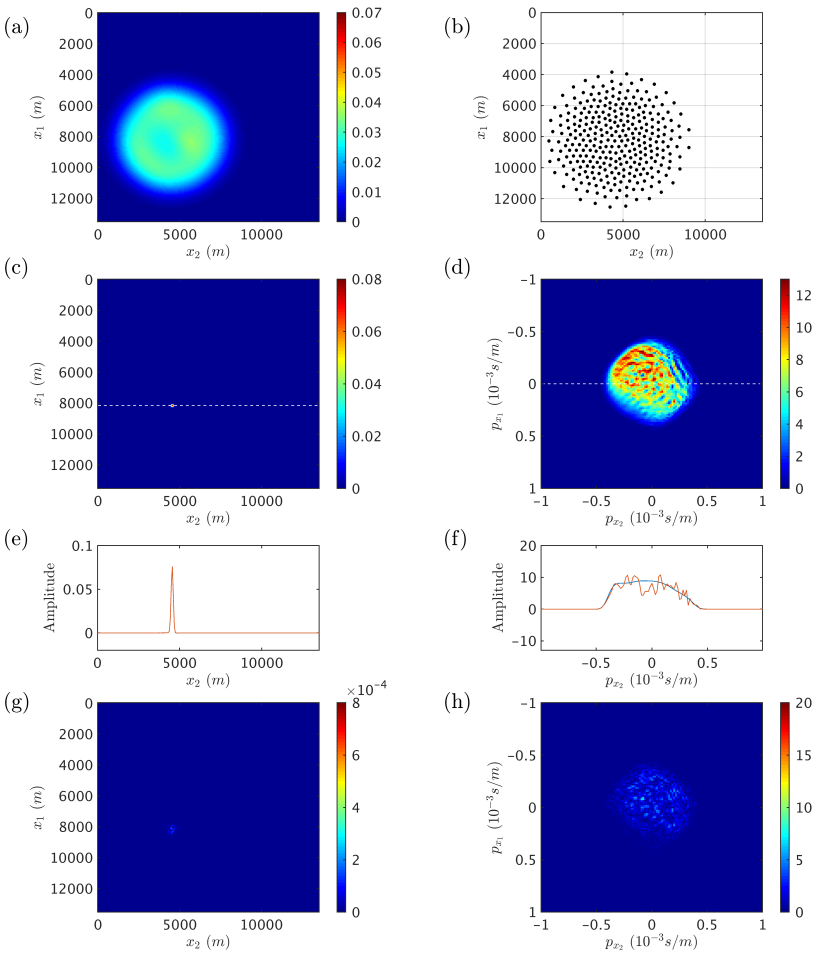


Figure 5.12: Geometry optimisation results using $J_1$ under the SEG/EAGE salt model: (a) optimised receiver density distribution, (b) optimised receiver geometry, (c) corresponding resolution function, and (d) AVP function. The dashed lines in (c) and (d) indicates the cross section locations of plot (e) and (f). The red line in (e) and (f) represents the evaluated geometry, while the blue line represents the reference geometry. (g) and (h) are the residuals of the resolution function and the AVP function respectively, displayed in absolute scale.

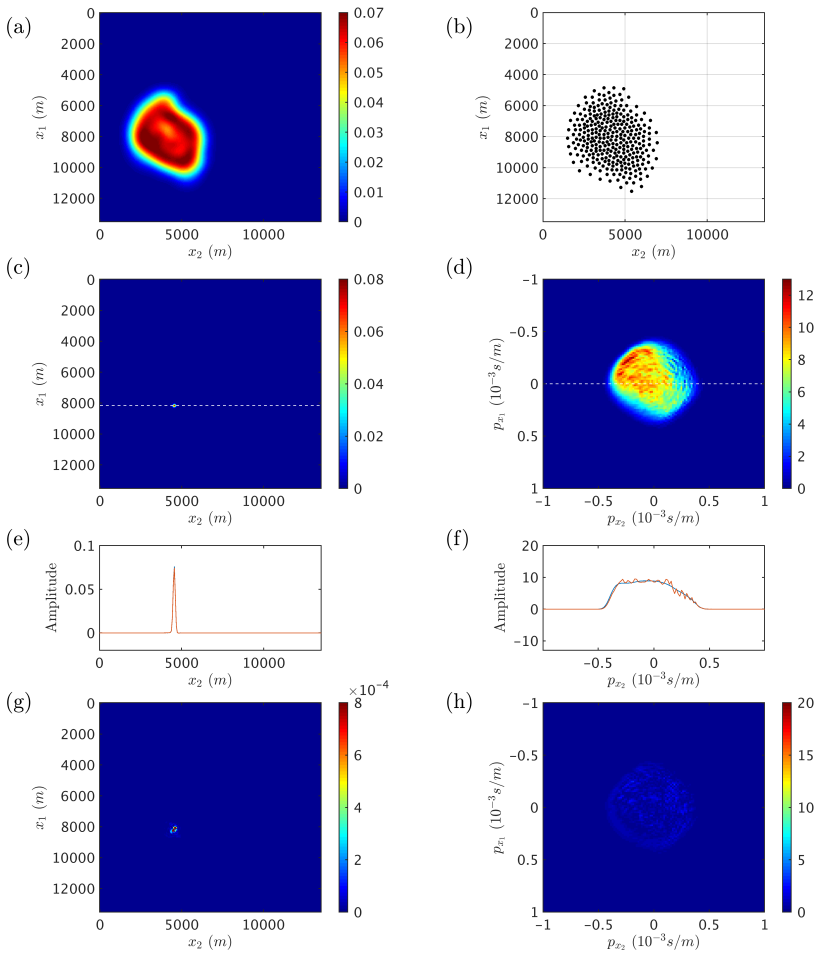


Figure 5.13: Geometry optimisation results using $J_2$ under the SEG/EAGE salt model: (a) optimised receiver density distribution, (b) optimised receiver geometry, (c) corresponding resolution function, and (d) AVP function. The dashed lines in (c) and (d) indicates the cross section locations of plot (e) and (f). The red line in (e) and (f) represents the evaluated geometry, while the blue line represents the reference geometry. (g) and (h) are the residuals of the resolution function and the AVP function respectively, displayed in absolute scale.

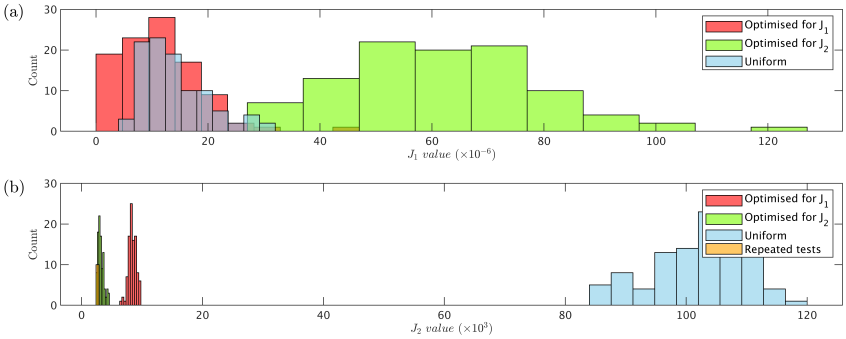


Figure 5.14: (a) Histograms of $J_1$ values of 100 realizations of the receiver density optimised for $J_1$ (red), the density optimised for $J_2$ (green), and the uniform density (blue). (b) Histograms of $J_2$ values of 100 realizations of the density optimised for $J_1$ (red), the density optimised for $J_2$ (green), the uniform density (blue), and the one-bin histogram of the ten repeated tests of optimising for $J_2$ (orange).



$J_2$ (green), and the uniform density (blue). In addition, we repeat the complete optimisation process for $J_2$ ten times to test the overall stability with the inherent uncertainty of the sampling set. The J2 values of the outcome are plotted as a one-bin histogram (orange) in Figure 5.14b. The density optimised for $J_2$ has the best angle coverage: the green histogram has the lowest mean value, and its variation is ten percent of the variation of the blue histogram. The $J_2$ values of the ten repeated tests lie within the range of the green histogram. It shows that optimising for $J_2$ is stable, despite the variations in geometry realizations during the optimisation process.

The density maps and geometries after optimisation in Figure 5.12a have a relatively symmetric shape, while the density map in Figure 5.13a has an irregular shape. This implies that the resolution requirement is less affected by the complex overburden than the AVP requirement, where the complex overburden can have an asymmetric effect on the geometry. Moreover, optimising for $J_1$ already leads to a huge improvement in the AVP function compared to the uniform situation. Nevertheless, the density optimised for J2 achieves the highest amplitude accuracy over all azimuths and angles.

### 5.2.3. VELOCITY ERROR ANALYSIS

Our acquisition design method requires the *a priori* knowledge of the subsurface, and the acquisition geometry is optimised for the input velocity model. A completely wrong velocity model could lead to an acquisition geometry that has an unacceptable illumination quality. In practice, typically a macro velocity model can be obtained from legacy seismic data. To analyse the influence of the velocity error, we use a velocity model that has been smoothed with a 600 m box of the velocity displayed in Figure 5.9 as the input velocity model and optimise for $J_2$. Therefore, the reference focal functions and the update directions are computed using the smoothed velocity model instead of the true velocity model during optimisation. As a result, Figure 5.15a and b show the optimised density and geometry using $J_2$ with the smoothed velocity; Figure 5.15c-h show the focal

functions that are computed using the true velocity model such that we can evaluate the true illumination quality. The optimised density has an irregular shape and is different from the optimised density using the true velocity in Figure 5.13a; the resolution function has a sharp peak in Figure 5.15c and e; the misfit in Figure 5.15g is small with the maximum being 0.8% of the scale of the resolution function. Compared to the optimisation result using the true velocity model, the angle distribution in Figure 5.15d is indeed different from the one in Figure 5.13d; however, Figure 5.15f and g show a similar residual level compared to the residual plots in Figure 5.13f and g. In addition, the histogram of 100 geometries transformed from the resulting density shows a similar $J_2$ distribution compared to the one obtained by using the true velocity model (Figure 5.16).

## 5.3. DISCUSSION

We have demonstrated that the proposed gradient method with several initial guesses is effective in designing a 3D geometry for an optimum illumination. In the examples of the SEG/EAGE salt model, we used four initial guesses and the number of iterations for each individual process is typically 50; so the total number of iterations is 200. In comparison, a genetic algorithm needs around 4500 evaluations of the objective function to reach a geometry solution of a similar quality.



The reference AVP functions in Figure 5.4d and 5.10d do not have flat spectra, because we have a laterally varying velocity model and we use the complex conjugate of the propagation operator as the migration operator in the calculation of focal functions. Hence, there is an imprint of the complex velocity in the AVP function. It is possible to include an illumination compensation or to use a least-squares migration in the focal function calculation, to ensure a flat AVP spectrum. However, such applications are not expected to change the optimisation results, because both the reference and the updated focal functions are calculated using the same migration operator.

The proposed method does not guarantee a global minimum solution due to the nonlinear parameter-data relationship. A local minimum is acceptable for the acquisition design problem, since it provides improved illumination. With regard to the non-uniqueness of the geometry solutions, we expect additional constraints to reduce the ambiguity in solutions. In practice, we can generate a group of solutions that have a similar error, then choose one according to the acquisition preferences. For instance, the receivers can only be deployed in a certain area due to obstacles in field; the inline direction of the marine streamer usually depends on the ocean flow direction. These extra constraints can help eliminate candidate geometries and reach realistic proposals.

Acquisition geometry design consists of designing both the source and the receiver geometries. Our current implementation copes with one at a time. As demonstrated in the examples, we design the receiver geometry with the source side fixed. Likewise, the source geometry can be optimised with the receiver side fixed. The gradient expression for optimising the source geometry would be equation 5.4 and 5.6 with $\mathbf{S}_k(z_m)$ being replaced by $\mathbf{D}_k(z_m)$. To optimise both the source and the receiver geometries simultaneously, we can think of a double-loop approach that optimises the source geometry for several iterations, then optimises the receiver geometry with the latest source geometry

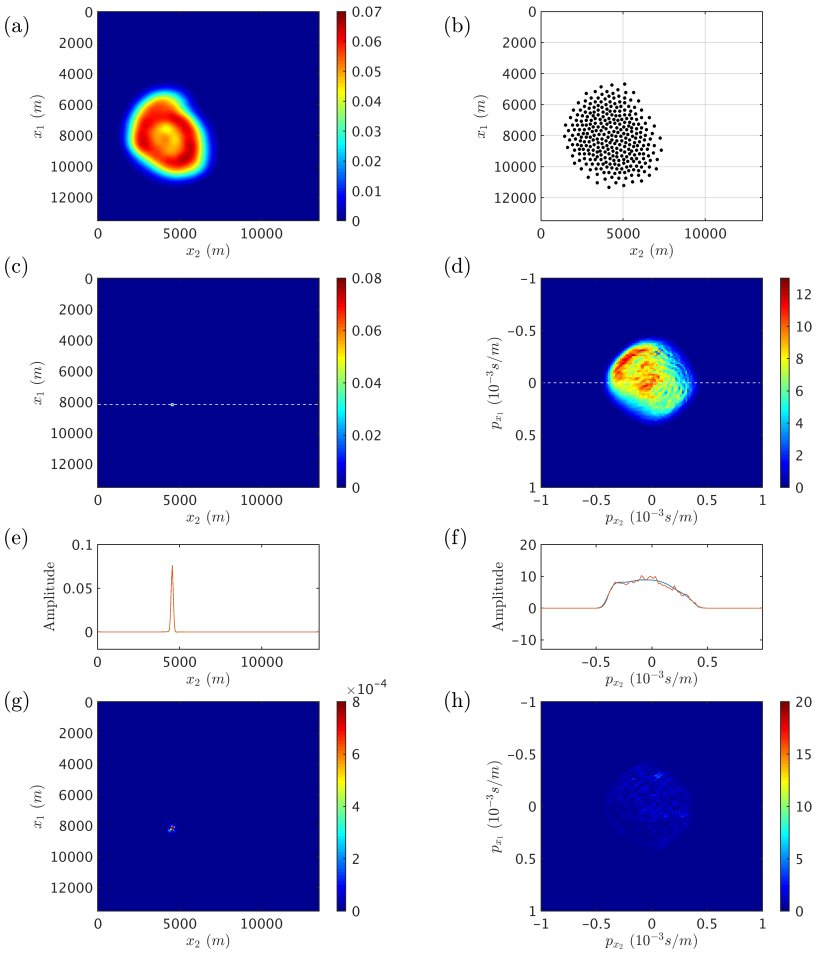


Figure 5.15: Geometry optimisation results using $J_2$ under the smoothed SEG/EAGE salt model: (a) optimised receiver density distribution, (b) optimised receiver geometry, (c) corresponding resolution function, and (d) AVP function that are computed with the true velocity model. The dashed lines in (c) and (d) indicates the cross section locations of plot (e) and (f). The red line in (e) and (f) represents the evaluated geometry, while the blue line represents the reference geometry. The reference focal functions are computed using the true velocity model for comparison. (g) and (h) are the residuals of the resolution function and the AVP function respectively, displayed in absolute scale.

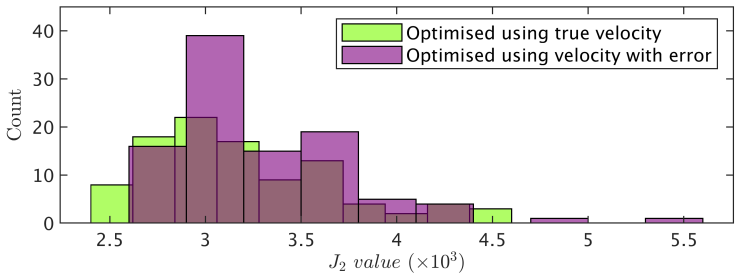


Figure 5.16: Histograms of $J_2$ values of 100 realizations of the density optimised for $J_2$, using the true velocity (green) and the smoothed velocity model (purple).

for several iterations, and so on. This method will be discussed in Chapter 7.

One potential extension of the current method is to design for long-offset data only, e.g. because FWI requires high-angle diving waves. An acquisition geometry that has a good angle coverage at the high angles is likely to be beneficial for FWI. Shen et al. (2018) have shown that the far offset of the OBN data was one of the key ingredients for the quality uplift in the FWI velocity model. For the geometry optimisation, it is possible to apply a weight to favour the large angles in the AVP function and only invert for this weighted AVP function.

In this chapter, we have shown examples with a simplified scenario with no noise presence, a single target point, and a fixed receiver number. Noise is an important aspect to address in seismic acquisition design. In a land acquisition environment, the seismic data processing suffers tremendously from an unsatisfactory signal to noise ratio, which is caused by strong surface-wave noise; and in a marine acquisition environment, the seismic data processing suffers more from surface multiple reflections. The quantitative models of how noise affects the data quality should be established; after that, we can use them as the acquisition design criteria or include them in the existing design methods. Note that illumination is the only criterion used here. In practice, we also need to consider the impact of other processing techniques before imaging.

In the examples, we only optimise the geometry for one target point, and the resulting sampling density tends to be non-uniform. When multiple target points are considered, the optimised density is expected to become more regular, depending on the extent of the subsurface target area. If the target area is relatively small and the overburden is complex, we expect an non-uniform density distribution. However, if the target is a large area such that the criterion would be to have a general good image of the subsurface, a different forward model should be chosen instead of the focal beam analysis for computational efficiency. For example, a 3D ray-trace modelling such as the one described in Ibrahim (2005) would be more suitable to assess the image quality of a large area in the subsurface.

The focal beam analysis used here to quantify the illumination properties is based on primary wavefield. Multiple scattering could provide additional illumination at the target point under certain circumstances. (Kumar et al., 2016) discussed the focal beam analysis including multiples and showed that the focal beam results with multiples are

better compared to the focal beam results with primaries only. It is possible to change the forward model to focal beam analysis including multiples in our method. The optimisation problem is expected to be more nonlinear due to the nonlinear behaviour of multiples, which can result in many geometries that have a similar objective function value. The resulting acquisition geometries are expected to be irregular due to the multiple propagation paths and the complex overburden.

A fixed number of receivers is chosen to reduce the nonlinearity of the optimisation problem. With the current gradient method, the easiest way to incorporate an indefinite receiver number is to repeat the procedures in Figure 5.1 or algorithm 1 for several different receiver numbers. We can then compare the quality and the cost from different numbers of receivers. It is also possible to make the receiver number varying within a certain range, by adding a constraint on the total number of receivers to $J_1$ and $J_2$ in equation 5.3 and 5.5, respectively. However, keep in mind that a varying number of sampling points will make the optimisation problem more nonlinear. A linearised algorithm is likely to end up in local minima. We will discuss a global optimization method incorporating such a constraint in the next chapter.

This methodology and the parameterisation provide interesting opportunities in designing the location of ocean-bottom seismometers for crustal imaging purpose (Peirce and Day, 2002), or finding an optimum distribution of an earthquake monitoring network (Rabinowitz and Steinberg, 1990). It requires the knowledge of the geological overburden, the location of the hypocentre, and the earthquake mechanism. The criterion would be redefined to suit the requirement in crustal imaging or earthquake monitoring. For instance, the forward model should include converted waves for crustal imaging. The gradient calculation would be modified according to the forward formulation, nevertheless the inversion framework can stay the same. The sampling density, as a macro solution of the geometry, provides the opportunity of a linearised framework, which is computationally efficient.



## 5.4. CONCLUSIONS

We have proposed and demonstrated a methodology that can automatically optimise an irregular acquisition geometry for an improved target illumination under a complex overburden. The results indicate interesting geometry design strategies for two different requirements. When the requirement is resolution, the uniform geometry already has an acceptable resolution. When the requirement is angle coverage, an optimised geometry achieves a high amplitude accuracy over all azimuths and angles compared to the uniform geometry. In the optimisation scheme, the parameter—sampling density—is a macro solution of the acquisition geometry, which can be used for flexible acquisition systems, regular acquisition systems, and potentially automated devices. This parameterisation allows us to use a linearised optimisation algorithm via a gradient descent scheme to solve the acquisition design problem. Focal beam analysis provides the link between the subsurface and the target illumination for calculating the update. The proposed method is effective and computationally efficient.

# 6

# OPTIMISING THE RECEIVER GEOMETRY: A GENETIC ALGORITHM

*In the previous chapter, we presented a gradient method to solve the acquisition design problem. The gradient method was sufficient to find an acceptable minimum in the linearised situations. However, in practice the acquisition design problem is nonlinear due to many nonlinear factors and constraints that are difficult to linearise, e.g. spatial restrictions for the deployment of receivers. Global optimisation algorithms are more suitable for solving nonlinear acquisition design problems; however, the computation cost is high. In this chapter, we propose a low-rank parameterisation to make the size of the search space manageable and, thus, make it feasible to use a genetic algorithm to solve the nonlinear acquisition design problem.*

This chapter is being submitted for publication in a professional journal.

## 6.1. NONLINEAR ACQUISITION DESIGN PROBLEM

Optimising an acquisition geometry in practice is a nonlinear problem due to many nonlinear factors and constraints that are difficult to linearise. For instance, Morrice et al. (2001) parameterise an orthogonal split-spread design using decision variables on source and receiver location spacings, the amount of receiver equipment, and the production rate of the seismic crews. The nonlinear objective function of minimising cost is fast to calculate; therefore, the optimisation can be solved by an exhaustive search. However, the computation cost for a model-based acquisition design method is high, so we cannot afford to do an exhaustive search. In order to quantify illumination using a wavefield modelling approach, many methods use a reduced number of design parameters, such that an efficient search is possible (e.g. Alvarez et al., 2004; Monsegny, 2017).

In this chapter, we propose a nonlinear optimisation framework where focal beam analysis is used as the forward model and a genetic algorithm is used to solve the problem. To demonstrate the method, we choose the angle-dependent illumination as the criterion for acquisition geometry optimisation (AVP function), and add nonlinear constraints to the objective function. Similar as in Chapter 5, we fix the source geometry and optimise the receiver geometry. Thus, the objective function can be formulated as the following:



$$J = \sum_{p_x,p_y} ||\Delta\widetilde{\mathbf{P}}_k(z_m,\phi_{ref}) - \Delta\widetilde{\mathbf{P}}_k(z_m,\phi_r)||^2 + Constraints, \tag{6.1}$$

where $\phi_r$ is the receiver sampling density; $\phi_{ref}$ is the reference sampling density, which is chosen as a full 3D sampling; $z_m$ is the target depth level; $p_x$ and $p_y$ are the horizontal ray parameters; subscript $_k$ indicates the target location; the tilde sign indicates the linear radon domain; therefore, $\Delta\widetilde{\mathbf{P}}_k$ represents the AVP function. $Constraints$ represent penalty functions that can limit the number of sampling points, the cost, and incorporate the implementation preferences in practice. They are usually nonlinear functions.

## 6.2. PARAMETERISATION

Using the sampling density for inversion as described in the previous chapter allows a linear approximation between the illumination criteria and the update. However, for a global optimisation algorithm this means a large number of parameters, which is the same number as the number of grid cells in the model. It is also possible to use the spatial coordinates of the sampling points; however, the sum of parameters is at least in the order of a few hundred. To use a global optimisation method efficiently, we need to limit the number of parameters to the order of tens. In our method, we use the sampling density and transform it to the actual geometry for evaluating the AVP function. To reduce the number of parameters, we introduce a low-rank parameterisation approach based on the sampling density such that a sufficient search is possible.

### 6.2.1. PRINCIPLE COMPONENT ANALYSIS

In order to reduce the number of parameters for a genetic algorithm, we use Principle Component Analysis (PCA) to extract features from a range of possible sampling density solutions. In mathematical terms, these features are referred to as the principle components, which are a set of orthogonal basis vectors whose linear combinations can exactly represent the original data set. The original data can also be approximated by using the most prominent basis vectors, which have the largest eigenvalues. Since the basis vectors with large eigenvalues contain the main features of the dataset, they together can characterise the whole data set in an efficient way. Because of this property, PCA is widely used in reducing data redundancy, dimension reduction in large data sets, and feature extraction in machine learning (Jolliffe, 2011; Bengio et al., 2013).

A collection of possible solutions need to be selected as the first step of this approach. We can use prior knowledge to generate a collection of possible solutions. For example, we can use certain patterns above the target location, the amplitude of the one-way wavefield propagated from the target to the surface, the inter-iteration densities from the gradient method, and human-interacted drawings. As an example, Figure 6.1 shows a collection of possible solutions from the gradient method. More details with regard to this will be discussed in Section 6.3. In this work, we assume that the basis vectors—which are extracted from a range of possible solutions—can sufficiently characterise the solution space of the optimisation problem. Therefore, searching for a linear combination of the basis vectors can form a density solution that is close to the global minimum.



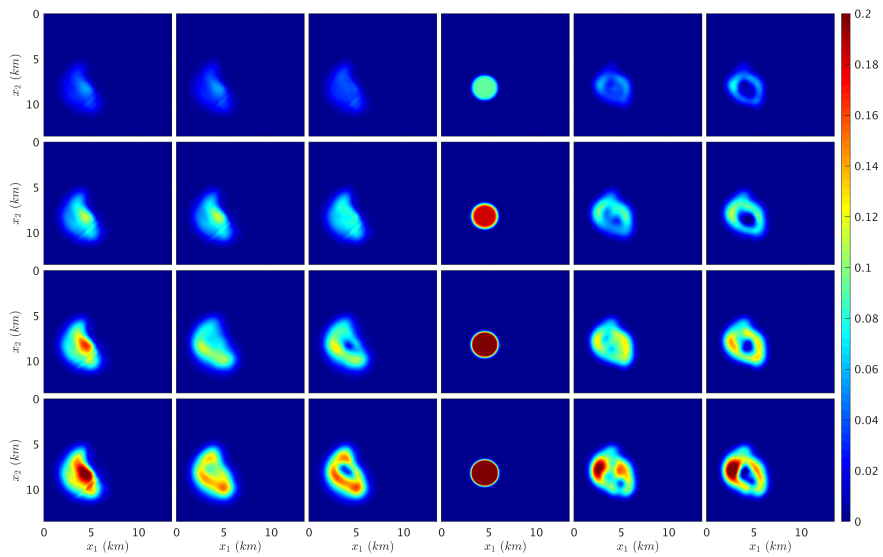


Figure 6.1: A collection of possible density solutions selected from the gradient method. Each row corresponds to a different total number of sampling points, which is the sum of all spatial values. From top to bottom, the total number of sampling points increases.

### 6.2.2. BASIS IMAGES AND EIGENVALUES

After selecting a collection of possible solutions, we extract the most prominent features from the collection by performing PCA. Each density distribution, such as the ones in Figure 6.1, is reorganized to a column vector; and all vectors are concatenated in a big matrix that forms the input data for PCA. The matrix can be formulated as:

$$A = [\Gamma_1, \Gamma_2, ..., \Gamma_M], \tag{6.2}$$

$$with\ \Gamma_i = \Phi_i - \overline{\Phi}, \tag{6.3}$$

where $\Phi_i$ represents a column vector of the length $Nx_1 \times Nx_2$, reorganised from a 2D spatial density distribution. The average of the density vectors is defined by $\overline{\Phi} = \frac{1}{M}\sum_{i=1}^{M}\Phi_i$; $\Gamma_i$ represents the difference of each density vector from the average; the matrix $A$ contains $M$ shifted density vectors.

PCA can be solved by eigendecomposition or singular value decomposition of the covariance matrix of the input data (Jolliffe, 2011). The covariance matrix is given by $C = AA^T$, which measures the similarity by the correlation between all possible pairs of the density vectors $\Phi_i$. Here, we choose eigendecomposition to solve the PCA. The eigenvectors $\mathbf{v}_k$ of C can be found:

$$C\mathbf{v}_k = \mu_k \mathbf{v}_k,\ for\ k = 1, 2, ..., M, \tag{6.4}$$

where $\mathbf{v}_k$ is the eigenvector; $\mu_k$ is the eigenvalue; $M$ represents the total number of eigenvectors found, which equals the total number of input density vectors. All eigenvectors are sorted according to the eigenvalues in a descending order. The principle components are the ordered eigenvectors, each one accounting for a different variation of the density vectors. The eigenvalues represent the importance of all eigenvectors given the order of significance of the variation. These eigenvectors are a set of orthogonal bases that together characterise the variation between the density vectors.

Each eigenvector $\mathbf{v}_k$ is reorganized into a 2D image, and we call it a basis image. For example, we show the first ten basis images in Figure 6.2 of the 24 input densities shown in Figure 6.1. The procedure described here is similar to the procedure of extracting the so-called eigenfaces in the field of face recognition (Turk and Pentland, 1991). Figure 6.3 shows the average, which is used to compute the covariance matrix. The basis images are orthogonal and together they can characterise the main features of the input data—the density distributions.

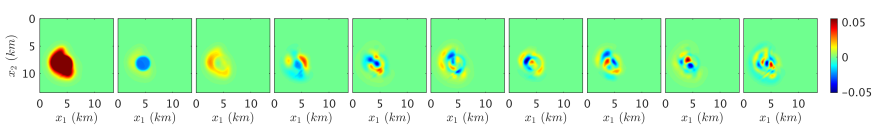


Figure 6.2: The first ten basis images from the eigendecomposition/PCA of the input density distributions.

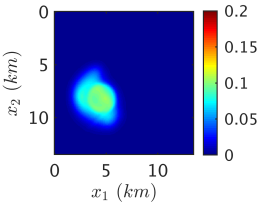


Figure 6.3: The average density of all densities presented in Figure 6.1.

### 6.2.3. LOW-RANK APPROXIMATION

Each individual density can be re-expressed exactly as a linear combination of all the M basis images. Each density can also be approximated using only the most significant basis images, those that have the largest eigenvalues and which, therefore, account for the most variance within the set of density images. The linear weights $\Psi = [\psi_1, \psi_2, ..., \psi_{M'}]$ are the parameters for the genetic algorithm, where $M'$ is the number of basis images used. A new density vector can be generated by the following operation:

$$\Phi_{new} = \sum_{k=1}^{M'} \mathbf{v}_k \psi_k + \overline{\Phi}. \tag{6.5}$$

The new density vector is then reorganised to a 2D density distribution, after which it can be used to calculate the objective function. The projection of each original density in Figure 6.1 organised into a column vector, onto the bases is a vector that contains the linear weights for each basis vector. The multiplication of the projections and the eigenvectors plus the average gives the input density. As an example of low-rank approximation, $M = 24$ in Figure 6.1, but we use $M' = 10$ in Figure 6.2 to approximate the input densities. Figure 6.4 shows the reconstruction error using the ten basis images; note that the colour scale is ten percent of the one of the input data displayed in Figure 6.1 to improve visibility. Although there are minor errors, we consider the first ten basis images sufficient to reconstruct the input densities.

We verify this approach with a new density distribution that is not from the input densities in Figure 6.5a. Figure 6.5b shows the reconstructed density using $M' = 10$. We can see that the main features are reconstructed, while the amplitude is different in some detailed areas. Overall, the reconstruction is relatively good, considering that only ten basis images are used. We can then proceed with these ten basis images and use the parameter vector $\Psi$, which contains only ten scalar values, as the parameters for the genetic algorithm.

## 6.3. GENETIC ALGORITHM FOR AN OPTIMUM GEOMETRY

We use a genetic algorithm to find the optimum parameters—the best linear combination of the basis vectors—to obtain the optimum geometry. Genetic algorithms are well established methods in the category of evolutionary computation to solve global optimisation problems. The main idea is to evolve the initial population to fit the objective

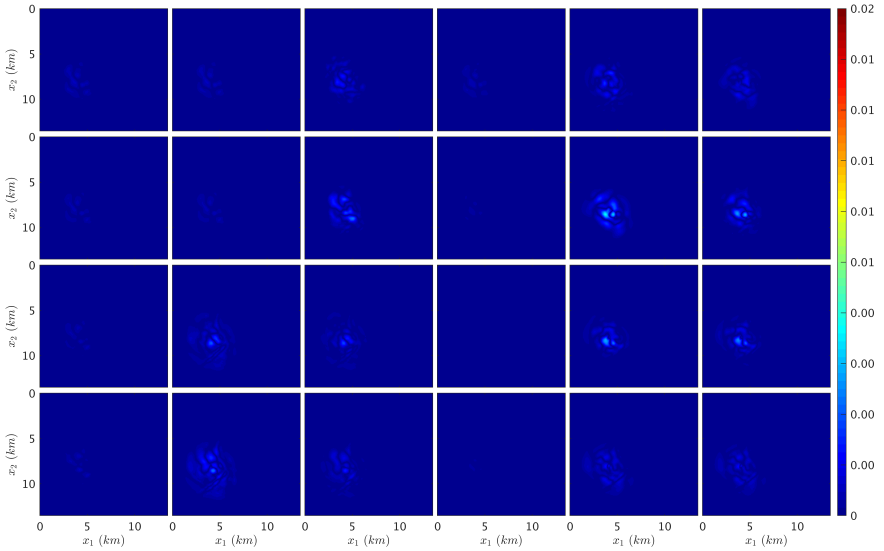


Figure 6.4: The difference between the input densities and the reconstructed ones.

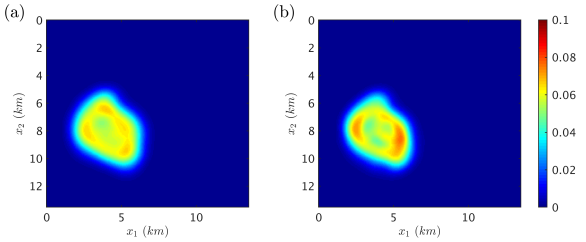


Figure 6.5: (a) A density map that is not from the collection of density solutions shown in Figure 6.1. (b) The reconstructed density map using the ten basis vectors in Figure 6.2.

by operators that are inspired by Darwinian natural selection. For a detailed description of genetic algorithms, see Holland (1975); for a description of genetic algorithm applications in geophysical problems, see e.g. Sambridge and Drijkoningen (1992); Curtis and Snieder (1997). The process of a genetic algorithm can be summarised as: 1) initialize a random population of parameter vectors; 2) evaluate the objective function for each parameter vector; 3) create a new population by selection, crossover and mutation operators; 4) repeat step 2)–3) until the stopping criterion is met.

The upper and lower bounds of the vector elements are set as several times the maximum and minimum of the projection vectors. At each iteration of the genetic algorithm, the parameter vectors are updated and new densities are generated; then the objective function is evaluated for the new densities. In this way, the number of parameters is reduced to the order of ten's and the genetic algorithm can run efficiently. For implementation, the MATLAB® genetic algorithm toolbox is used.

## 6.4. NUMERICAL EXAMPLES

The SEG/EAGE velocity model (Aminzadeh et al., 1996), displayed in Figure 5.9, with a target located at (8160 m, 4560 m, 2300 m) is used to test the method. We consider a scenario of stationary receivers and full 3D sampling at the source side. First, we explain how the collection of possible solutions can be generated. Second, we compare the genetic algorithm to the gradient method in a linearised scenario, where the amount of receivers is fixed. Third, we allow the amount of receivers to be flexible; in addition, we consider two constraints: a cost constraint on the number of receivers and a nonlinear spatial feasibility map. With this example, we show that with the genetic algorithm framework, it is easy to include various constraints.



### 6.4.1. GENERATE A COLLECTION OF POSSIBLE SOLUTIONS

As an example in this chapter, the collection of possible solutions is selected from the initial guess from the gradient method, the final density for each initial guess, and the linear combination of the initial guess and the first gradient from the gradient method. The gradient method is performed for several fixed numbers of receivers, $N_r$. For each $N_r$, the gradient method starts with different initial guesses; and for each initial guess, the density that has the lowest misfit value is chosen as the resulting density. The resulting densities from very different initial guesses are usually different in shapes; this is probably because the gradient method is sensitive to local minima. In other words, the resulting densities from different initial guesses are in different local minima. To account for the other possible solutions that are in between the initial guesses and the resulting density, we take each initial guess, and add a scaled version of its gradient at the first iteration. By doing this, we intend to include a sufficient variety of solutions that contain all the required characteristics of the solution space.

The gradient method was run for the velocity model shown in Figure 5.9. For $N_r$ of 150, 300, 450, and 600, the receiver density is optimised using the gradient method. The 24 selected possible solutions are displayed in Figure 6.1, where the rows from top to

bottom are the density maps selected from optimisation for $N_r$ of 150, 300, 450 and 600, respectively. The first and the fourth columns correspond to two different types of initial guesses, which are the one-way wavefield energy and a concentrated circle. The second and the fifth columns correspond to the final density results. The third and the sixth columns correspond to the linear combination of the initial guesses and their gradients. We can see that in a row they are mostly different in shape; in a column, they have some resemblance in shape but are different in values.

### 6.4.2. GEOMETRY OPTIMISATION IN A LINEARISED SCENARIO

With a fixed amount of receivers, the inverse problem is relatively linear, so that the gradient method is already sufficient to find an acceptable minimum. We set the receiver number to be 300 and compare the results from the gradient method and the genetic algorithm. By doing this, we can verify the genetic algorithm setting to produce similar quality results as the gradient method.

The gradient method starts from two different initial models, being the one-way wavefield energy and a concentrated circle. It uses a line search of five steps and the number of iterations for each run is 10. For the genetic algorithm, the objective function development is shown in Figure 6.6. The number of generations is 150 and the population size is 200. The number of parameters is ten referring to the ten basis images in Figure 6.2 that are used to construct a new density. The mean value and the minimum value of the objective functions in each generation is shown in Figure 6.6a; and Figure 6.6b shows a zoomed-in version of the minimum objective function from generation 20 to the end. We can clearly see that the general trend goes down and there are fluctuations in the values showing that it is a nonlinear problem.

The resulting density functions from the gradient method and the genetic algorithm are shown in Figure 6.7. We transform the densities in Figure 6.7 to 100 geometry realisations and plot their objective function values in histograms in Figure 6.8. The resulting densities are different in shape; however, the histograms of 100 realizations of them overlap, due to the nondeterministic feature in the transformation from the density to the geometry realisations. This shows that they have similar quality in the AVP function. It also shows that the genetic algorithm with the current setting can find a similar quality result compared to the gradient method with the fixed number of receivers. Note that the gradient method is not limited by the ten eigen images.

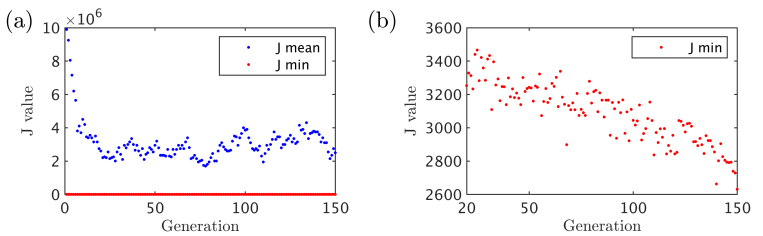


Figure 6.6: Objective functions during the generations of the genetic algorithm.

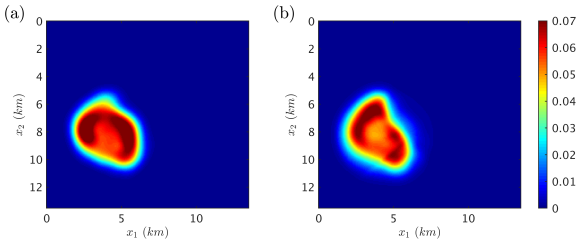


Figure 6.7: Resulting density maps from (a) the gradient method, and (b) the genetic algorithm.

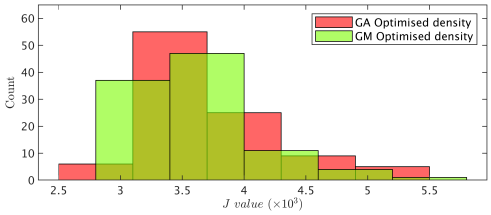


Figure 6.8: Histograms of the results from 100 runs of the gradient method (GM) and the genetic algorithm (GA).



### 6.4.3. GEOMETRY OPTIMISATION WITH NONLINEAR CONSTRAINTS

#### COST CONSTRAINT ON SAMPLING NUMBER

Incorporating the sampling density, we next use the genetic algorithm to solve acquisition design in a scenario with nonlinear constraints. The first constraint is the cost in relation to the number of receivers, of which we choose to be a shifted and stretched sigmoid function. The constraint function can be written as:

$$J_{cost}(\phi_r) = \frac{a}{1 + e^{-b(\sum \phi_r - c)}} + d, \tag{6.6}$$

where $a, b, c, d$ are real-valued scaling factors. The constraint is on the sum of the receiver density, i.e. the total number of receivers. The number of receivers can be changed, by changing the weighting factor of this constraint function.

The cost constraint function used in this example is shown in Figure 6.9, with $a = 1200, b = 0.02, c = 280, d = 95.49$, and a maximum number of the receivers being 600. We can see that it is a nonlinear function of the total amount of sampling points. The red dots are the bench marks of $N_r = 150, 300, 450, 600$. Note that the gradient results from these receiver numbers were used to make the collection of possible solutions to prepare for the parameterisation of the genetic algorithm.

#### DEPLOYMENT FEASIBILITY MAP

We add another nonlinear spatial feasibility map to the receiver locations. In practice, there are many locations that are not feasible for the stationary receivers. For example,

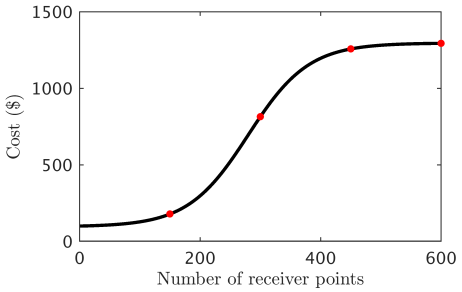


Figure 6.9: Cost penalty function versus the number of receivers, where $a = 1200, b = 0.02, c = 280, d = 95.49$, and the maximum number of receivers is 600.

the region near the platform is not accessible; when the sea floor is rough , the placement of receivers is restricted. Therefore, we introduce a spatial constraint on the receiver density, which states the maximum density allowed in a certain region given by $\phi_{max}(x,y)$. Note that $\phi_{max}$ may be zero for certain $(x,y)$. The total objective function combining these two constraints can be written as:

$$J_{tot} = \sum_{p_x,p_y} ||\Delta\widetilde{\mathbf{P}}_k(z_m,\phi_{ref}) - \Delta\widetilde{\mathbf{P}}_k(z_m,\phi_r)||^2 + \lambda J_{cost}(\phi_r),\ s.\ t. \quad \phi_r(x,y) \le \phi_{max}(x,y), \tag{6.7}$$

where $\sum_{p_x,p_y} ||\Delta\widetilde{\mathbf{P}}_k(z_m,\phi_{ref}) - \Delta\widetilde{\mathbf{P}}_k(z_m,\phi_r)||^2$ is the objective function of the AVP criterion shown in equation 6.1; $\lambda$ is the coefficient of the constraint function $J_{cost}$; $\phi_{max}$ represents the maximum receiver density allowed at each lateral location on the acquisition surface.

The deployment feasibility map used in this example is shown in Figure 6.10. The black curved line represent a ridge formation on the sea floor where no receivers can be placed; the density there is zero. The rectangular region and the elliptical region have restrictions on the maximum local density. This may be caused by a rough sea floor. This map restricts the aerial distribution of the receiver sampling.

#### CONSTRAINED OPTIMISATION

In the method of using the genetic algorithm, the feasibility map in Figure 6.10 is added to the collection of possible solutions and PCA is performed to produce ten basis images, which are are used together with the parameters to generate the updated densities. For the constraint $\lambda$, the higher the value, the lower the number of receivers in the final results. We vary the value of $\lambda$ and run the genetic algorithm. The resulting densities and the corresponding AVP functions are shown in Figure 6.11. From left to right, there are results from $\lambda = 100, 10, 1$, and the corresponding resulting receiver number is 206, 371, 599, respectively. From top to bottom, there are the receiver densities, geometries, AVP functions, the cross section of the AVP function plotted against the reference, and the residuals. Since in Figure 6.11a the receiver number is small, the lower right corner is less influenced by the rectangular spatial constraint. In Figure 6.11f and k, you can see a clear imprint of the rectangular shape. In Figure 6.11d, the amplitude has a large

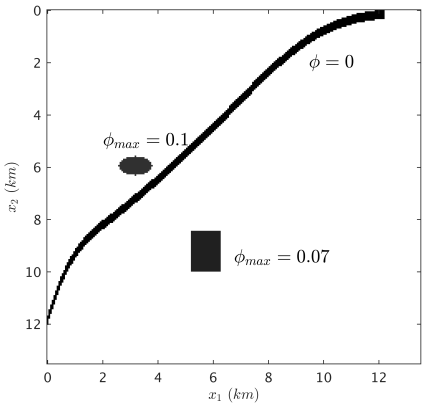


Figure 6.10: Nonlinear spatial constraint on the feasibility of the receiver sampling.

fluctuation, in Figure 6.11i and n have less amplitude fluctuation, but the angles around $p_{x_2} = -0.5\ 10^{-3} s/m$ are less represented. In the residual plots (Figure 6.11e, j, o), Figure 6.11e visibly has the highest residual; however, it can be argued that Figure 6.11j and o have a similar level of residual, even though Figure 6.11o has a much higher receiver number. This is probably due to the spatial feasibility map, that restricts the quality of the AVP function. Figure 6.12 shows the histogram of 100 geometries from the resulting densities from $\lambda = 100, 10, 1$. It can be seen that the objective function is lower when the number of receivers is higher; however, the improvement from $\lambda = 1$ to $\lambda = 10$ is arguably small. The results show that it is possible to incorporate a genetic algorithm to accommodate different constraints in the acquisition design problem.



## 6.5. DISCUSSION

The results of this work suggest that a genetic algorithm framework is easy to use in the presence of nonlinear geophysical and operational constraints. It is a derivative-free method so that the additional constraint functions can be simply added to the main objective function. The gradient method, which produces the collection of possible solutions, takes 4*2*50=400 iterations; and the genetic algorithm takes 200*150=30000 iterations, even though with ten parameters. The benefit is that the possible solutions generated by the gradient method can narrow down the search space for the genetic algorithm, such that a sufficient search is viable.

Genetic algorithms have been successfully applied in solving many global optimisation problems. However, they also have limitations, especially tuning set-up parameters in practice. A genetic algorithm has to be tuned for each particular problem to assure convergence and an efficient search. For example, first, the population size should be chosen large enough to avoid premature convergence (Sambridge and Drijkoningen, 1992). Second, it could be that all populations in one generation are equally good, then the driving force of the genetic operator is lost. The settings in our examples can be fur-

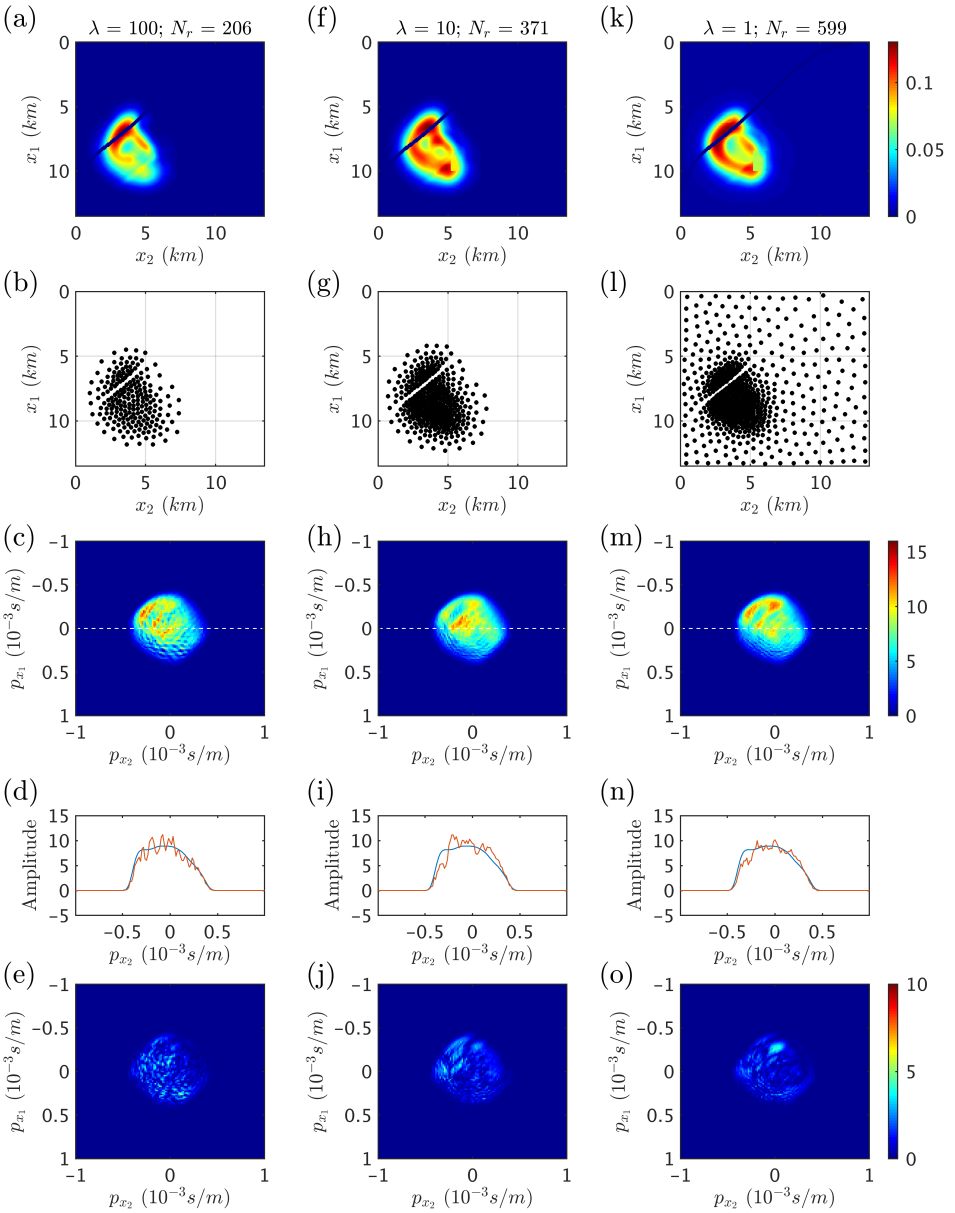


Figure 6.11: Geometry optimisation results with varying $\lambda$: left column $\lambda = 100$; middle column $\lambda = 10$; right column $\lambda = 1$. From top to bottom, each row corresponds to the optimised density distribution, the geometry, the AVP function, the cross sections of AVP function at $p_{x_1} = 0$, and the residual, respectively.

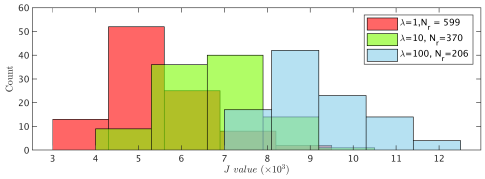


Figure 6.12: Histograms for resulting receiver densities with $\lambda = 1$ (blue), $\lambda = 10$ (orange), and $\lambda = 100$ (yellow).

ther improved for efficiency; and the mechanism of the genetic algorithm can also be changed to suit the problem and have better convergence performance. However, we do not recommend concentrating on improvement in this one particular problem, since the setting will change for a different problem. Once the acquisition scenario is fixed, further improvements on the optimisation efficiency can be gradually achieved.

There are other ways to limit the number of parameters in a genetic algorithm. For example, the density distribution can be represented by a coarse grid of support values from which the density function can be interpolated. Even though it will be difficult to get ten parameters. The disadvantage of this approach is that we can only get a low-resolution density distribution and we loose the details of the density distribution in order to keep the number of parameters small. In this work, we choose not to use such parameters; this approach indeed can be tested but not limited to. Future research on parameterisation for the acquisition geometry is required.

PCA has the strength of parameter reduction, but has also limitations. Firstly, PCA assumes linearity; the density is formed by linear combinations of these basis images. Second, we assumed that the basis images contain all the characteristics of the solutions. However, it is possible that the linear combination of the basis images will not result in a better solution. It does not assure all characteristics. Then we are searching in the same pool. Thus, it is important in this method to use the gradient method to produce enough variations of possible solutions.

Inverse problems can be solved using machine learning methods (Röth and Tarantola, 1994). The combination of PCA and genetic algorithm hints the future work of solving the acquisition design problem using machine learning methods. Many popular machine learning methods, such as support vector machines, neural networks, classification and regression trees, etc., can be seen as just different ways of estimating basis functions from data (Murphy, 2012). PCA can be seen as equivalent to a linear neural network. Earp and Curtis (2019) use a statistical neural network to solve the nonlinear travel time tomography problem. The velocity model can be seen as the receiver density distribution. The density parameterisation for the acquisition geometry can stay the same, and for each realisation an objective function value can be calculated. The densities and the corresponding objective functions from both the gradient method and the genetic algorithm can be used to train the neural network.

## 6.6. CONCLUSIONS

In conclusion, we have presented a low-rank parameterisation approach to reduce the number of parameters for the acquisition design problem by using PCA, and solve it with a genetic algorithm. The results show that the method is effective in finding a reasonable minimum, in comparison to the gradient method, in a scenario of a fixed number of sources. In a scenario of flexible number of sources, the genetic algorithm finds solutions with different weights on the cost constraint. This approach can be used for solving the acquisition geometry design in other nonlinear situations and is compatible with other nonlinear constraints.

# 7

# OPTIMISING BOTH SOURCE AND RECEIVER GEOMETRIES

*Previously, we have presented a gradient method and a genetic algorithm that can optimise the receiver geometry while the source geometry is fixed and vice versa. In this chapter, we present a gradient method that can optimise both the source and receiver geometries in order to obtain a good illumination of a chosen target point, such that they can compensate the missing illumination for each other. With numerical examples, we demonstrate that the proposed method is effective.*

This chapter is adapted from a published SEG Technical Program Expanded Abstract (2019).
DOI: https://doi.org/10.1190/segam2019-3216398.1

In Chapter 5, we have presented optimisation of the receiver geometry using a gradient method, where the sources are assumed to be densely available and only the receiver geometry is optimised. Figure 7.1 illustrates the flowchart of the method, where the step in the blue box—update receiver geometry—is made automatic such that redesigning the geometry manually is no longer necessary. The focal receiver beams in the spatial and/or the linear Radon domain are used as the illumination criteria; and the velocity model, the target, the frequency range, the wavefield modelling and migration operators are the user-defined inputs. A gradient descent method is implemented to solve the optimisation problem so that it is computationally efficient.

A complete acquisition geometry design should include the source as well as the receiver sampling geometry on the acquisition surface. In this chapter, we propose a method that optimises both receiver and source geometries, and uses the AVP function as the criterion. The flowchart in Figure 7.2 shows that the inversion has two variables to update, i.e. the receiver geometry and the source geometry. We limit the number of receivers and sources, and use a double-loop flip-flop updating procedure to solve the optimisation problem.

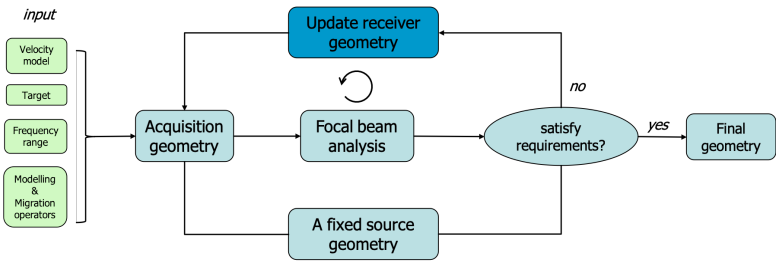


Figure 7.1: A flowchart of target-oriented acquisition design that optimises the receiver geometry with a fixed source geometry.

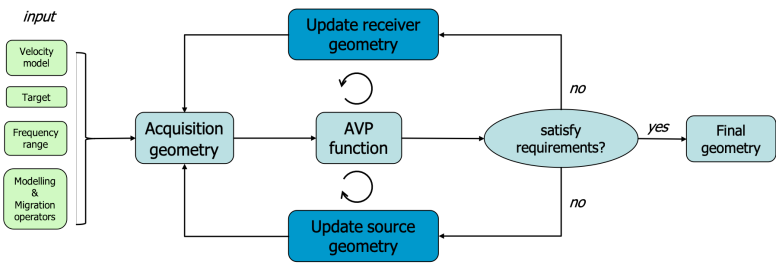


Figure 7.2: A flowchart of target-oriented acquisition design that optimises both receiver and source geometry. Note that we use a flip-flop updating procedure to solve the optimisation problem; i.e. the source geometry is fixed while updating the receiver geometry, and vice versa.

## 7.1. OPTIMISING FOR BOTH RECEIVER AND SOURCE GEOMETRY

### 7.1.1. OBJECTIVE FUNCTION

To optimise the receiver and source sampling geometry for a good illumination at the target, we define an objective function in a least-squares sense, which aims to minimise the difference between the AVP function obtained from the updating source and receiver geometries and the one from a user-defined reference geometry. As described in Section 5.1.1, the sampling density, which is defined as the number of sampling points per unit area, is used as the parameter of this inversion scheme. The full 3D regular geometry obeying Nyquist criterion is chosen as the reference geometry. The objective function is formulated as follows:

$$J = \sum_{p_x,p_y} ||\Delta\widetilde{\mathbf{P}}_k(z_m,\phi_{ref},\phi_{ref}) - \Delta\widetilde{\mathbf{P}}_k(z_m,\phi_r,\phi_s)||^2, \tag{7.1}$$

where $\phi_r$ and $\phi_s$ are the receiver and source sampling densities, respectively; $\phi_{ref}$ is the reference sampling density; $\Delta\widetilde{\mathbf{P}}_k(z_m,\phi_{ref},\phi_{ref})$ represents the AVP function from the reference receiver and source density $\phi_{ref}$, and $\Delta\widetilde{\mathbf{P}}_k(z_m,\phi_r,\phi_s)$ represents the AVP function from the variable receiver density $\phi_r$ and the variable source density $\phi_s$. More details have been discussed in Section 5.

### 7.1.2. RECEIVER DENSITY UPDATE

Based on the objective function in equation 7.1, and the definition of the AVP function in Chapter 4, we can write the gradient with respect to the receiver density as:

$$\nabla_{\phi_r} J = -2\sum_{\omega} \mathbf{W}_k(z_0,z_m)\mathbf{L}^H\{\widetilde{\mathbf{E}}_k(z_m)\circ\widetilde{\mathbf{S}}_k(z_m)\}[\mathbf{W}(z_0,z_m)]^H, \tag{7.2}$$

where the residual $\widetilde{\mathbf{E}}_k(z_m) = \Delta\widetilde{\mathbf{P}}_k(z_m,\phi_{ref},\phi_{ref}) - \Delta\widetilde{\mathbf{P}}_k(z_m,\phi_r,\phi_s)$, and $\mathbf{L}^H$ represents the inverse linear Radon transform. The operator $\mathbf{W}$ represents forward propagation and $\mathbf{W}^H$ approximates backward propagation; $\widetilde{\mathbf{S}}_k(z_m)$ is the focal source beam of target point $k$; $\mathbf{W}_k$ is the $k^{th}$ column of matrix $\mathbf{W}$ and it forward propagates the wavefield at target $k$ to the designated depth level. The element-wise multiplication of the residual $\widetilde{\mathbf{E}}_k(z_m)$ and the source beam $\widetilde{\mathbf{S}}_k(z_m)$ is used to update the receiver density so that it is combined with the influence of the source geometry. The gradient is obtained by forward propagation, correlation with the one-way wavefield from the target, and applying the imaging condition. For more details on the gradient, please refer to Section 5.1.4.

### 7.1.3. SOURCE DENSITY UPDATE

Similarly, the gradient with respect to the source density can be formulated as:

$$\nabla_{\phi_s} J = -2\sum_{\omega} \mathbf{W}_k(z_0,z_m)\mathbf{L}^H\{\widetilde{\mathbf{D}}_k(z_m)\circ\widetilde{\mathbf{E}}_k(z_m)\}[\mathbf{W}(z_0,z_m)]^H, \tag{7.3}$$

where the residual $\widetilde{\mathbf{E}}_k(z_m)$ again represents the difference compared to the reference AVP function and is used to update the source density; $\widetilde{\mathbf{D}}_k$ is the focal receiver beam in the linear Radon domain. Similar as the receiver density update, the residual is multiplied with the receiver beam; then the gradient is obtained by forward propagation, correlation with the one-way wavefield from the target, and applying the imaging condition. (See Section 5.1.4 for more details.)

We use a gradient descent scheme combined with several starting models and line search to solve the optimisation problem. During the process, the source side is fixed while updating the receiver side, and vice versa. In this way, we can optimise for both receiver and source geometries under one criterion. Note that the objective function and the gradient are formulated for one target point. In the case of multiple target points, the objective function and the gradient are summed over all target points.

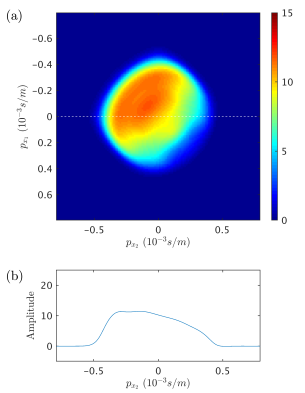


Figure 7.3: (a) The reference AVP function and (b) a cross section at $p_{x_1} = 0\ s/m$.

## 7.2. NUMERICAL EXAMPLES

### 7.2.1. SIMPLE 3D MODEL

We use the simple 3D velocity model presented in Chapter 5 to show how the method works (Figure 5.3). The target point located at a depth of 570 m is indicated by a red dot in the 3D velocity model with a survey area of 4 km by 4 km. Both the receiver and source numbers are limited to 100. The objective is to calculate the receiver and source geometry that has the minimum difference in angle coverage compared to the reference beam in figure 7.3, which has a full 3D sampling that satisfies the Nyquist rule at both receiver and source sides.

For computational reasons, the frequency range used here is 5 to 10 Hz. Based on Nyquist sampling, the full geometry that ensures no aliasing effect for a bandwidth of 5-10 Hz requires $67^2 = 4489$ receivers. For geometry optimisation, the numbers of receivers and sources are both limited to 100, which is less than 3% of the Nyquist require-

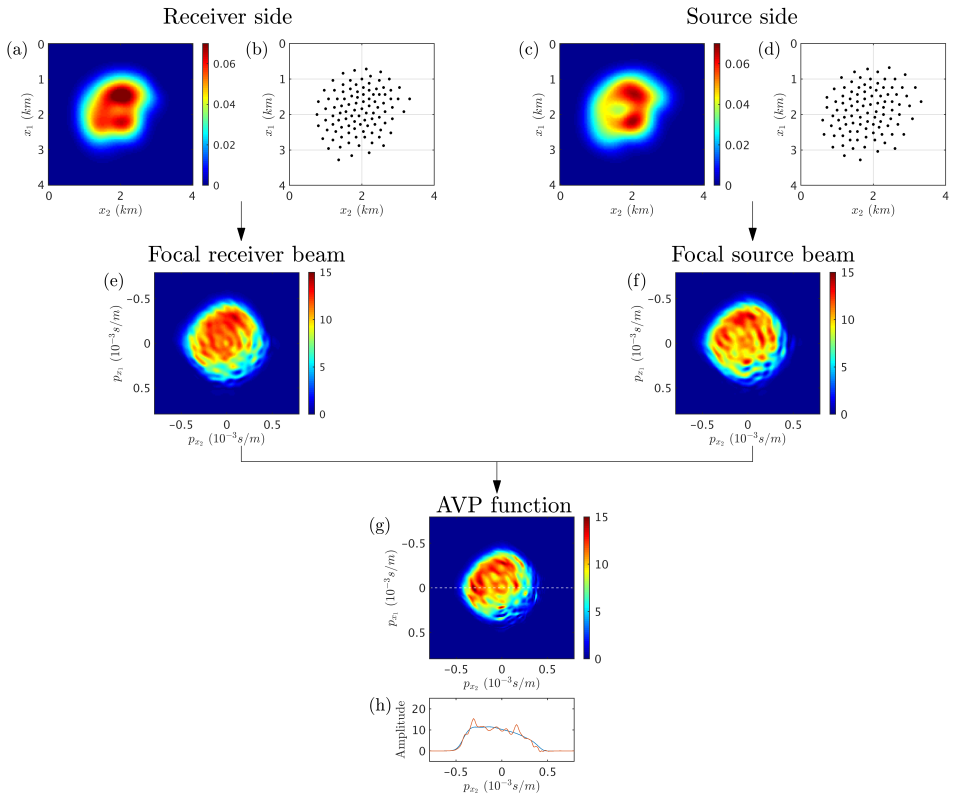


Figure 7.4: Acquisition geometry optimisation results under the simple 3D model: (a) optimised receiver sampling density, (b) optimised receiver geometry, (c) optimised source density, (d) optimised source geometry, (e) focal receiver beam of the optimised receiver geometry, (f) focal source beam of the optimised source geometry, (g) corresponding AVP function, and (h) a cross section of (g) at $p_{x_1} = 0\ s/m$.

ment. Figure 7.3 shows that the reference AVP function has a full angle coverage, and its spectrum is non-flat due to the influence of the salt overburden. We consider that the focal functions from the full 3D sampling on both the source and receiver sides represent the best attainable illumination, provided that no illumination compensation or least-squares inversion procedures are used.

During optimisation, we update the receiver geometry twice, then switch to update the source geometry twice, and repeat this process until the maximum number of iterations is reached. Figure 7.4 shows the geometry optimisation results: the optimised receiver geometry gives the focal receiver beam in Figure 7.4e; the optimised source geometry gives the focal source beam in Figure 7.4f; the AVP function in Figure 7.4g combines the focal receiver and source beams. The focal beams show adequate focusing and sensing ability of the source and receiver geometries. The AVP function shows a full angle coverage with small amplitude fluctuations compared to the reference. The optimised geometries of 100 receivers and 100 sources achieve an angle-dependent amplitude accuracy that is close to the one in Figure 7.5a, where there is a full 3D source sampling, and the number of sources is approximately 45 times the one in Figure 7.4. Compared to the case of optimised receiver geometry and a sparse uniform geometry of 100 sources in Figure 7.5b, Figure 7.4g shows a much better angle coverage. In this example, the optimised sampling densities show irregular shapes, where the spatial variance in the sampling density indicates the area that should be more densely sampled and the area that could be more sparsely sampled. It could also results in other shapes due to the nonlinearity of the problem.



### 7.2.2. SEG/EAGE MODEL

The geometry optimisation method is also tested for the subsampled SEG/EAGE salt model shown in Chapter 5. The velocity model with a target located at (8160 m, 4560 m, 2300 m) was shown in Figure 5.9, and the reference AVP function and a cross section are shown in Figure 7.6. The reference AVP function has a full angle coverage and the spectrum has an imprint from the complex salt overburden. In this example, the frequency range is $5-10$ Hz, and the Nyquist sampling requires $169^2 = 28561$ receivers and sources. The reference source and receiver geometries are full 3D geometries that satisfy the Nyquist criterion. Both the receiver and the source number are limited to 300, which is roughly 1% of the Nyquist requirement.

The results of optimising the receiver and the source geometries are shown in Figure 7.7. The focal receiver beam in Figure 7.7e shows that the large angles can be sufficiently detected, but it has less coverage in the small angles. The focal source beam in Figure 7.7f shows a sufficient angle coverage with part of the small angles slightly over-represented. Nonetheless, the resulting AVP function as a combination of the focal beams shows a relatively adequate angle coverage compared to the reference (Figure 7.7g and h). For comparison, Figure 7.8a shows the AVP function from an optimised geometry of 300 receivers and a full 3D source sampling. The angle-dependent amplitude is more accurate than the one in Figure 7.7h; however, note that the number of sources in the full 3D sampling is approximately 100 times the one in Figure 7.7d. The AVP function displayed in Figure 7.8b is from a sparse uniform geometry of the same number of sources as in Fig-

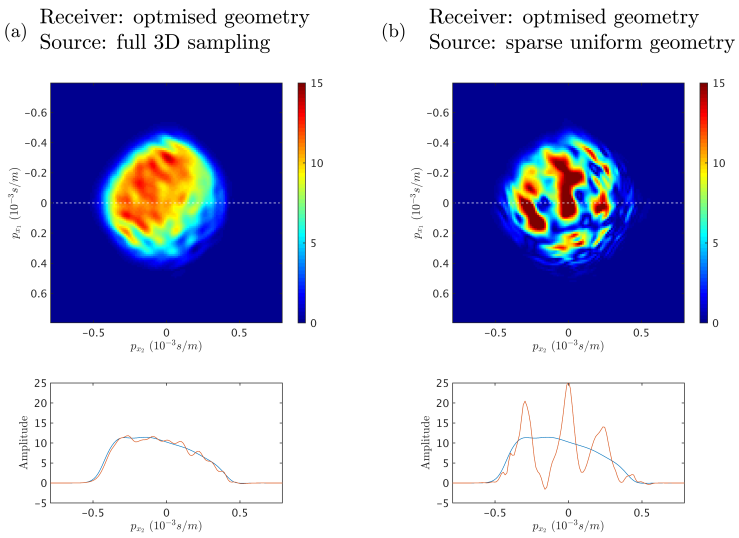


Figure 7.5: The AVP functions and their cross sections for two cases: (a) the receiver geometry is optimised for a full 3D source sampling geometry; (b) the receiver geometry is the same as the one in Figure 7.4b, and the source geometry is a sparse uniform geometry of 100 sources. In the cross section plots, blue represents the reference AVP function, and red represents the AVP function of the corresponding geometries.



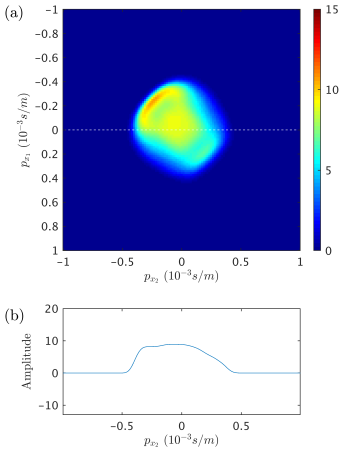


Figure 7.6: (a) The reference AVP function and (b) a cross section at $p_{x_1} = 0\ s/m$.

ure 7.7d. It shows a large fluctuation in amplitude and, therefore, a low angle-dependent amplitude accuracy.

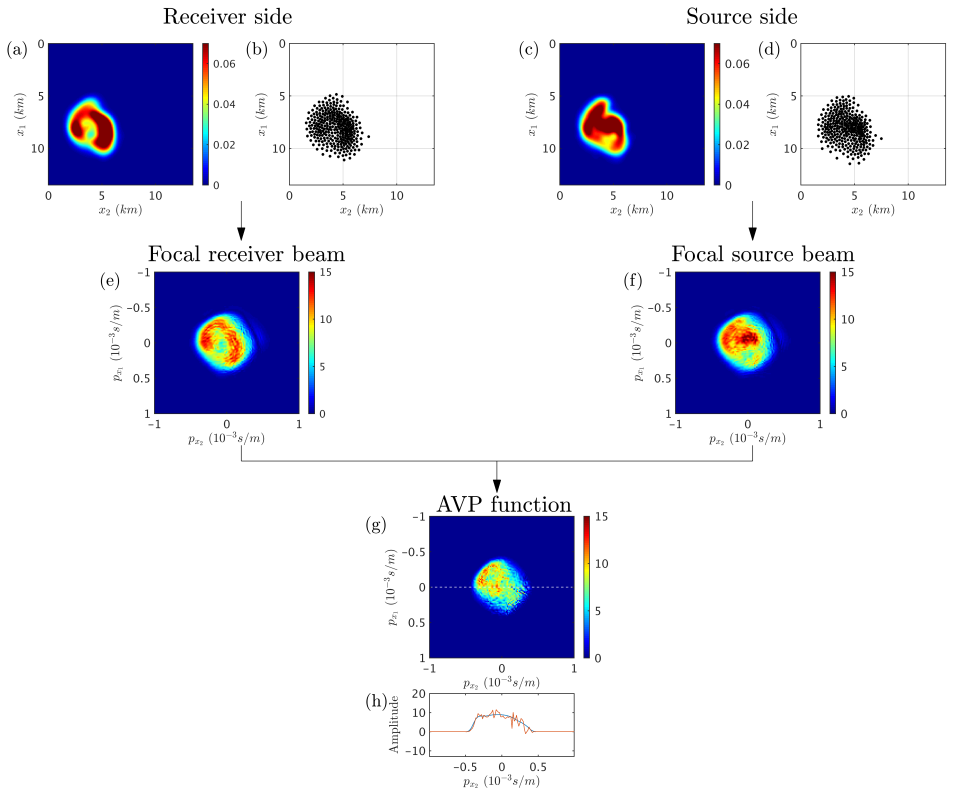


Figure 7.7: Acquisition geometry optimisation results under the SEG/EAGE salt model: (a) optimised receiver sampling density, (b) optimised receiver geometry, (c) optimised source density, (d) optimised source geometry, (e) focal receiver beam of the optimised receiver geometry, (f) focal source beam of the optimised source geometry, (g) corresponding AVP function, and (h) a cross section of (g) at $p_{x_1} = 0\ s/m$.

## 7.3. CONCLUSIONS

We have demonstrated a methodology that can optimise the receiver and source geometries for improving angle-dependent information at a target location. The results show that the source geometry can take the missing angles caused by the receiver geometry into account and try to compensate that. With much less source effort, it achieves a similar illumination quality compared to the full 3D source sampling. The presented acquisition design framework can be interesting for the development of automated devices for seismic acquisition.

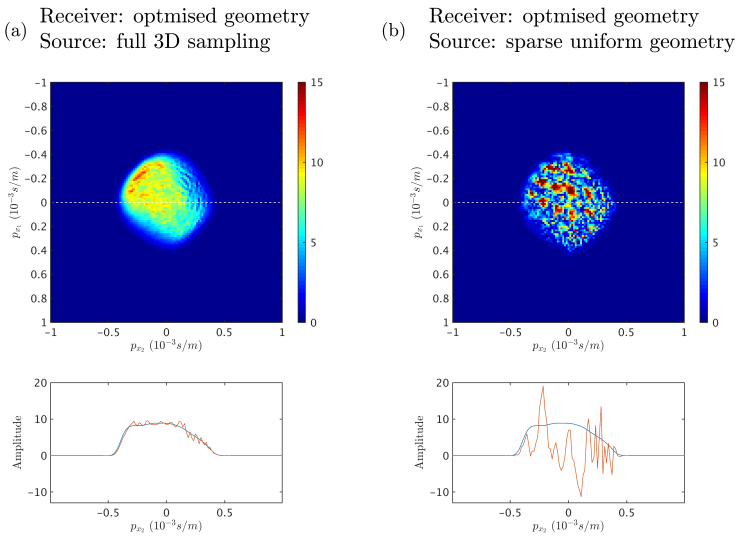


Figure 7.8: The AVP functions and their cross sections for two cases: (a) the receiver geometry is optimised for a full 3D source sampling geometry; (b) the receiver geometry is the same as the one in Figure 7.7b, and the source geometry is a sparse uniform geometry of 100 sources. In the cross section plots, blue represents the reference AVP function, and red represents the AVP function of the corresponding geometries.

# III

# Part III

# 8

# CONCLUSIONS AND RECOMMENDATIONS

## 8.1. CONCLUSIONS

In this thesis, we have investigated two aspects of the optimisation of marine seismic acquisition. Part I describes the source encoding methods in blended acquisition; Part II describes target-oriented acquisition geometry optimisation using focal beam analysis to quantify the illumination criteria. The key findings are summarised below:

**Part I:**

- Repetitive shooting in a blended survey can enhance the signal-to-noise ratio and can enable deblending in individual shot gathers, which is more effective than the deblending methods that are restricted by the random time delay type of source encoding.
- Source ghosts can be exploited as part of the source encoding in the deblending process.
- Optimising the source encoding in a blended survey shows improvements in the deblending performance; therefore, it can potentially improve the data quality and reduce acquisition costs.

**Part II:**

- We have established a linearised acquisition optimisation method which allows us to optimise the source and receiver geometries separately, and simultaneously in a flip-flop mode.
- By using the sampling density as the parameter, the acquisition geometry optimisation problem can be solved by a gradient method, which is computationally efficient.

- Two criteria are used for acquisition geometry optimisation — resolution and angle-dependent illumination. The resolution criterion is less sensitive to geometry than the angle-dependent illumination criterion when the number of sampling points is fixed. The angle-dependent illumination of an optimised geometry has significantly more angle coverage than the one of an uniform geometry.

- We have established a nonlinear optimisation framework that uses a low-rank parameterisation and a genetic algorithm to solve the acquisition geometry optimisation problem. This framework can handle nonlinear constraints.

## 8.2. RECOMMENDATIONS

From a broader perspective, the concepts of Part I and II are seemingly contradicting to each other. Part I encourages to acquire repetitive information at the same spatial location, while Part II aims to reduce redundant information from different spatial sampling locations. It depends on the objectives and limitations of the acquisition survey at hand. For example, if the objective is to improve data quality by increasing trace density and the budget allows this, then acquiring redundant data for the sake of data quality makes sense; if the objective is to acquire data of the optimum quality with a limited budget and resources, then excluding redundant information is necessary. Nevertheless, optimisation of the survey should be tailored to each individual problem that has different objectives and restrictions.

Mathematical optimisation algorithms are recommended for solving such optimisation problem because of the following reasons. Acquisition surveys are commonly designed by heuristics due to the large amount of parameters, objectives and limitations. The processing and imaging algorithms have progressed tremendously through years, while the acquisition design principles are not always up to date with the new data processing techniques. Turning acquisition design into an optimisation problem can help us find unobvious links between the criteria and the design parameters fast; therefore, a more effective acquisition design can be obtained. In addition, the optimisation algorithms allows an automatic update of the acquisition parameters, which can potentially reduce cost.

This thesis established an acquisition design framework for one target point, where the focal beam analysis is used as the forward engine. To further develop the acquisition design method, the following is recommended:

- Ideally, a reservoir volume is considered for 3D acquisition design in a monitoring scenario. Therefore, the acquisition design method should include multiple target points so that they can represent a reservoir volume.

- To speed up the forward calculation for a reservoir volume, we need to consider a parallel computation of the focal functions, e.g. evaluating the focal functions of multiple target points simultaneously in a 'blended' fashion.

- Multiple scattering should be considered in the acquisition design framework. Kumar et al. (2016) discussed the focal beam analysis including multiples and showed

examples where multiples provide additional illumination at the target point. Our acquisition design framework can be easily extended to include multiple scattering by substituting the forward engine.

- More nonlinear constraints should be considered in the nonlinear acquisition design framework described in Chapter 6.
- The design parameter—sampling density—provides an interesting opportunity for the real-time geometry design of autonomous source and receiver devices (e.g. Dispersed Source Arrays discussed by Caporal et al., 2016).
- In practice, noise is one of the most important aspects in acquisition design; therefore it should be included in the acquisition optimisation procedure in future research.

# REFERENCES


Abma, R., and Ross, A., 2015, Practical aspects of the popcorn source method: 85th Annual International Meeting, SEG, Expanded Abstracts, 164–169.

Abma, R., Howe, D., Foster, M., Ahmed, I., Tanis, M., Zhang, Q., Arogunmati, A., and Alexander, G., 2015, Independent simultaneous source acquisition and processing: Geophysics, **80**, no. 6, WD37–WD44.

Alvarez, G., Pereyra, V., and Carcione, L., 2004, Model-based 3-D seismic survey design as an optimization problem: 74th Annual International Meeting, SEG, Expanded Abstracts, 63–66.

Aminzadeh, F., Burkhard, N., Long, J., Kunz, T., and Duclos, P., 1996, Three dimensional SEG/EAEG models—An update: The Leading Edge, **15**, no. 2, 131–134.

Amundsen, L., 1993, Wavenumber-based filtering of marine point-source data: Geophysics, **58**, no. 9, 1335–1348.

Andersen, K. D., 1995, Method for cascading sweeps for a seismic vibrator: U.S. Patent 5, 410, 517.

Araya-Polo, M., Verschuren, M., and Hohl, D., 2016, Target-oriented automatic shot selection: 86th Annual International Meeting, SEG, Expanded Abstracts, 3855–3859.

Bagaini, C., 2006, Overview of simultaneous vibroseis acquisition methods: 76th Annual International Meeting, SEG, Expanded Abstracts, 70–74.

Bagaini, C., 2008, Vibroseis acquisition method: U.S. Patent 8, 811,116.

Barbier, M. G., and Viallix, J. R., 1973, Sosie: a new tool for marine seismology: Geophysics: Geophysics, **38**, no. 4, 673–683.

Barr, F. J., and Sanders, J. I., 1989, Attenuation of water-column reverberations using pressure and velocity detectors in a water-bottom cable: 59th Annual International Meeting, SEG, Expanded Abstracts, 653–656.

Bearnth, R. E., and Moore, N. A., 1989, Air gun-slant cable seismic results in the gulf of mexico: 59th Annual International Meeting, SEG, Expanded Abstracts, 649–652.

Beasley, C. J., Chambers, R. E., and Jiang, Z., 1998, A new look at simultaneous sources: 68th Annual International Meeting, SEG, Expanded Abstracts, 133–135.

Beasley, C. J., Coates, R., and Lapilli, C., 2013, Wave equation receiver deghosting: 5th IEEE International Workshop on Computational Advances in Multi-Sensor Adaptive Processing (CAMSAP), pages 280–283.

Bengio, Y., Courville, A., and Vincent, P., 2013, Representation learning: A review and new perspectives: IEEE transactions on pattern analysis and machine intelligence, **35**, no. 8, 1798–1828.

Berkhout, A. J., and Blacquière, G., 2013, Effect of noise in blending and deblending: Geophysics, **78**, no. 5, A35–A38.

Berkhout, A. J., and Blacquiere, G., 2014, Combining deblending with source deghosting: 76th Annual International Conference and Exhibition, EAGE.

Berkhout, A. J., Ongkiehong, L., Volker, A., and Blacquière, G., 2001, Comprehensive assessment of seismic acquisition geometries by focal beams part I: Theoretical considerations: Geophysics, **66**, no. 3, 911–917.

Berkhout, A. J., 1982, Seismic migration, imaging of acoustic energy by wave field extrapolation, A: theoretical aspects: Elsevier.

Berkhout, A. J., 2008, Changing the mindset in seismic data acquisition: The Leading Edge, **27**, no. 7, 924–938.

Bernhardt, T., and Peacock, J., 1978, Encoding techniques for the vibroseis system: Geophysical Prospecting, **26**, no. 1, 184–193.

Campman, X., Tang, Z., Jamali-Rad, H., Kuvshinov, B., Danilouchkine, M., Ji, Y., Walk, W., and Smit, D., 2017, Sparse seismic wavefield sampling: The Leading Edge, **36**, no. 8, 654–660.

Caporal, M., Blacquiere, G., and Davydenko, M., 2016, 3D seismic acquisition with decentralized dispersed source arrays: 86th Annual International Meeting, SEG, Expanded Abstracts, 240–244.

Carlson, D., Söllner, W., Tabti, H., Brox, E., and Widmaier, M., 2007, Increased resolution of seismic data from a dual-sensor streamer cable: 77th Annual International Meeting, SEG, Expanded Abstracts, 994–998.

Chen, Y., Fomel, S., and Hu, J., 2014, Iterative deblending of simultaneous-source seismic data using seislet-domain shaping regularization: Geophysics, **79**, no. 5, V179–V189.

Chen, Y., Zhang, D., Jin, Z., Chen, X., Zu, S., Huang, W., and Gan, S., 2016, Simultaneous denoising and reconstruction of 5-D seismic data via damped rank-reduction method: Geophysical Journal International, **206**, no. 3, 1695–1717.

Chen, Y., 2015, Iterative deblending with multiple constraints based on shaping regularization: IEEE Geoscience and Remote Sensing Letters, **12**, no. 11, 2247–2251.

Curtis, A., and Snieder, R., 1997, Reconditioning inverse problems using the genetic algorithm and revised parameterization: Geophysics, **62**, no. 5, 1524–1532.

Day, A., Klüver, T., Söllner, W., Tabti, H., and Carlson, D., 2013, Wavefield-separation methods for dual-sensor towed-streamer data: Geophysics, **78**, no. 2, WA55–WA70.

De Bruin, C., Wapenaar, C., and Berkhout, A., 1990, Angle-dependent reflectivity by means of prestack migration: Geophysics, **55**, no. 9, 1223–1234.

Docherty, P., Hays, D., Shurtleff, R., and Paffenholz, J., 2005, Multi-component ocean bottom seismic data acquired with an autonomous node system: 67th Annual International Conference and Exhibition, EAGE.

Earp, S., and Curtis, A., 2019, Probabilistic neural-network based 2D travel time tomography: arXiv preprint arXiv:1907.00541.

Gardner, J., Lapilli, C., Xu, C., and González, A., 2012, Finite difference wave-equation illumination: A deep-water case study: SEG Annual Meeting.

Haavik, K. E., and Landrø, M., 2015, Variable source depth acquisition for improved marine broadband seismic data: Geophysics, **80**, no. 3, A69–A73.

Halliday, D., Laws, R., and Özbek, A., 2017, Phase sequencing, marine vibrators, and high-multiplicity simultaneous sources: 87th Annual International Meeting, SEG, Expanded Abstracts, 57–61.

Holland, J. H., 1975, Adaptation in natural and artificial systems: University of Michigan Press.

Hopperstad, J., Laws, R., and Kragh, E., 2008, Fundamental principles of isotropic marine source design: 70th Annual International Conference and Exhibition, EAGE.

Howard, M., 2007, Marine seismic surveys with enhanced azimuth coverage: Lessons in survey design and acquisition: The Leading Edge, **26**, no. 4, 480–493.

Howie, J. M., Robinson, N., Riviere, M., Lyon, T., and Manley, D., 2005, Developing the long-term seismic strategy for Azeri-Chirag-Gunashli, South Caspian Sea, Azerbaijan: The Leading Edge, **24**, no. 9, 934–939.

Ibrahim, A. A., 2005, 3D ray-trace modeling to assess the effects of overburden and acquisition geometry on illumination of pre-evaporite reservoirs in Karachaganak field, Kazakhstan: The Leading Edge, **24**, no. 9, 940–944.

Ikelle, L., 2010, Coding and decoding: Seismic data: The concept of multishooting: Elsevier.

Jolliffe, I., 2011, Principal component analysis: Springer.

Kinneging, N., Budejicky, V., Wapenaar, C., and Berkhout, A., 1989, Efficient 2D and 3D shot record redatuming: Geophysical Prospecting, **37**, no. 5, 493–530.

Knopoff, L., and Gangi, A. F., 1959, Seismic reciprocity: Geophysics, **24**, no. 4, 681–691.

Kontakis, A., and Verschuur, D., 2017, Using a hybrid focal: Curvelet transform for deblending: 87th Annual International Meeting, SEG, Expanded Abstracts, 4903–4908.

Kontakis, A., Wu, S., and Verschuur, D., 2016, Acquisition geometry-aware focal deblending: 78th Annual International Conference and Exhibition, EAGE.

Kumar, A., Blacquière, G., Pedersen, M. W., and Goertz, A., 2016, Full-wavefield marine survey design using all multiples: Geophysics, **81**, no. 3, P1–P12.

Landrø, M., and Amundsen, L., 2014, Is it optimal to tow air guns shallow to enhance low frequencies?: Geophysics, **79**, no. 3, A13–A18.

Latiff, A. H. A., Ghosh, D. P., and Latiff, N. M. A., 2017, Optimizing acquisition geometry in shallow gas cloud using particle swarm optimization approach: International Journal of Computational Intelligence Systems, **10**, no. 1, 1198–1210.

Lindsey, J., 1960, Elimination of seismic ghost reflections by means of a linear filter: Geophysics, **25**, no. 1, 130–140.

Liner, C. L., Gobeli, R., and Underwood, W. D., 1998, 3-D seismic survey design as an optimization problem: 68th Annual International Meeting, SEG, Expanded Abstracts, 117–120.

Mahdad, A., Doulgeris, P., and Blacquière, G., 2011, Separation of blended data by iterative estimation and subtraction of blending interference noise: Geophysics, **76**, no. 3, Q9–Q17.

Mahdad, A., 2012, Deblending of seismic data: Ph.D. thesis, Delft University of Technology.

Moldoveanu, N., Combee, L., Egan, M., Hampson, G., Sydora, L., and Abriel, W., 2007, Over/under towed-streamer acquisition: A method to extend seismic bandwidth to both higher and lower frequencies: The Leading Edge, **26**, no. 1, 41–58.

Moldoveanu, N., 2000, Vertical source array in marine seismic exploration: 70th Annual International Meeting, SEG, Expanded Abstracts, 53–56.

Monsegny, J., 2017, Bi-objective optimization for seismic survey design: 87th Annual International Meeting, SEG, Expanded Abstracts, 274–278.

Morrice, D. J., Kenyon, A. S., and Beckett, C. J., 2001, Optimizing operations in 3-D land seismic surveys: Geophysics, **66**, no. 6, 1818–1826.

Mueller, M. B., Halliday, D. F., van Manen, D. J., and Robertsson, J. O. A., 2015, The benefit of encoded source sequences for simultaneous source separation: Geophysics, **80**, no. 5, V133–V143.

Mueller, M. B., Halliday, D. F., van Manen, D. J., and Robertsson, J. O. A., 2016, Optimizing near-orthogonal air-gun firing sequences for marine simultaneous source separation: Geophysics, **81**, no. 6, V415–V423.

Muerdter, D., and Ratcliff, D., 2001, Understanding subsalt illumination through ray-trace modeling, part 3: Salt ridges and furrows, and the impact of acquisition orientation: The Leading Edge, **20**, no. 8, 803–816.

Murphy, K. P., 2012, Machine learning: a probabilistic perspective: MIT press.

Nakayama, S., Blacquière, G., Ishiyama, T., and Ishikawa, S., 2019, Blended-acquisition design of irregular geometries towards faster, cheaper, safer and better seismic surveying: Geophysical Prospecting, **67**, no. 6, 1498–1521.

Nyquist, H., 1928, Certain topics in telegraph transmission theory: Transactions of the American Institute of Electrical Engineers, **47**, no. 2, 617–644.

Okabe, A., Boots, B., Sugihara, K., and Chiu, S. N., 2009, Spatial tessellations: concepts and applications of voronoi diagrams:, volume 501 John Wiley & Sons.

Pacific Gas Electric, 2019, Seismic safety and advanced seismic testing: https://www.pge.com/myhome/edusafety/systemworks/dcpp/seismic/3D.shtml.

Parkes, G., and Hatton, L., 1954, The marine seismic source: D. Reidel publishing company.

Parkes, G., and Hegna, S. A marine seismic acquisition system that provides a full 'ghost-free' solution:, 2011.

Peirce, C., and Day, A. J., 2002, Ocean-bottom seismograph tomographic experiments—a consideration of acquisition geometries vs. resources: Geophysical Journal International, **151**, no. 2, 543–565.

Posthumus, B., 1993, Deghosting using a twin streamer configuration: Geophysical Prospecting, **41**, no. 3, 267–286.

Rabinowitz, N., and Steinberg, D. M., 1990, Optimal configuration of a seismographic network: a statistical approach: Bulletin of the Seismological Society of America, **80**, no. 1, 187–196.

Regone, C. J., 2007, Using 3D finite-difference modeling to design wide-azimuth surveys for improved subsalt imaging: Geophysics, **72**, no. 5, SM231–SM239.

Robertsson, J. O., Amundsen, L., and Pedersen, Å. S., 2016, Signal apparition for simultaneous source wavefield separation: Geophysical Journal International, **206**, no. 2, 1301–1305.

Röth, G., and Tarantola, A., 1994, Neural networks and inversion of seismic data: Journal of Geophysical Research: Solid Earth, **99**, no. B4, 6753–6768.

Sablon, R., Payen, T., Tonchia, H., Siliqi, R., Labarre, X., Salaun, N., and Men, Y. L., 2013, Ghost-free imaging combining synchronized multi-level source and variable-depth streamer: 83rd Annual International Meeting, SEG, Expanded Abstracts, 72–76.

Sambridge, M., and Drijkoningen, G., 1992, Genetic algorithms in seismic waveform inversion: Geophysical Journal International, **109**, no. 2, 323–342.

Santos, A. B., Porsani, M. J., and Góis, M. S., 2019, 3D seismic survey design using mixed-radix based algorithm inversion: Geophysical Prospecting, **67**, no. 7, 1720–1731.

Schneider, W. A., Larner, K. L., Burg, J. P., and Backus, M. M., 1964, A new data-processing technique for the elimination of ghost arrivals on reflection seismograms: Geophysics, **29**, no. 5, 783–805.

Secord, A., 2002, Weighted voronoi stippling: Proceedings of the 2nd international symposium on Non-photorealistic animation and rendering, pages 37–43.

Shen, X., Ahmed, I., Brenders, A., Dellinger, J., Etgen, J., and Michell, S., 2018, Full-waveform inversion: The next leap forward in subsalt imaging: The Leading Edge, **37**, no. 1, 67b1–67b6.

Sønneland, L., Berg, L. E., Eidsvig, P., Haugen, A., Fotland, B., and Vestby, J., 1986, 2-D deghosting using vertical receiver arrays: 56th Annual International Meeting, SEG, Expanded Abstracts, 516–519.

Soubaras, R., and Lafet, Y., 2011, Variable-depth streamer acquisition: Broadband data for imaging and inversion: 81st Annual International Meeting, SEG, Expanded Abstracts, 2364–2368.

Tenghamn, S., 2006, Motion sensors in a marine seismic streamer: US Patent Application No. 11/021,919.

Turk, M., and Pentland, A., 1991, Eigenfaces for recognition: Journal of cognitive neuroscience, **3**, no. 1, 71–86.

Vaage, S., 2002, Method and system for acquiring marine seismic data by using multiple sources: U.S. Patent 6, 906, 981.

Van Groenestijn, G. J. A., 2010, Estimation of primaries and multiples by sparse inversion: Ph.D. thesis, Delft University of Technology.

Van Melle, F., and Weatherburn, K., 1953, Ghost reflections caused by energy initially reflected above the level of the shot: Geophysics, **18**, no. 4, 793–804.

Van Veldhuizen, E., Blacquière, G., and Berkhout, A., 2008, Acquisition geometry analysis in complex 3D media: Geophysics, **73**, no. 5, Q43–Q58.

Van Veldhuizen, E., 2006, Integrated approach to 3-D seismic acquisition geometry analysis: Ph.D. thesis, Delft University of Technology.

Van Wijngaarden, A. J., 1998, Imaging and characterisation of angle-dependent seismic reflection data: Ph.D. thesis, Delft University of Technology.

Vermeer, G. J., 2002, 3D seismic survey design, second edition: Society of Exploration Geophysicists.

Volker, A., Blacquière, G., Berkhout, A., and Ongkiehong, L., 2001, Comprehensive assessment of seismic acquisition geometries by focal beams part II: Practical aspects and examples: Geophysics, **66**, no. 3, 918–931.

Weglein, A., Shaw, S., Matson, K., Sheiman, J., Stolt, R., Tan, T., Osen, A., Correa, G., Innanen, K., and Guo, Z., 2002, New approaches to deghosting towed-streamer and ocean-bottom pressure measurements: 72nd Annual International Meeting, SEG, Expanded Abstracts, 2114–2117.

Womack, J., Cruz, J., Rigdon, H., and Hoover, G., 1990, Encoding techniques for multiple source point seismic data acquisition: Geophysics, **55**, no. 10, 1389–1396.

Wu, S., Blacquière, G., and van Groenestijn, G. J. A., 2015, Shot repetition: an alternative approach to blending in marine seismic: 85th Annual International Meeting, SEG, Expanded Abstracts, 48–52.

Yilmaz, Ö., 2001, Seismic data analysis: Processing, inversion, and interpretation of seismic data: Society of exploration geophysicists.

Zu, S., Zhou, H., Chen, Y., Qu, S., Zou, X., Chen, H., and Liu, R., 2016, A periodically varying code for improving deblending of simultaneous sources in marine acquisition: Geophysics, **81**, no. 3, V213–V225.

Zu, S., Zhou, H., Mao, W., Zhang, D., Li, C., Pan, X., and Chen, Y., 2017, Iterative deblending of simultaneous-source data using a coherency-pass shaping operator: Geophysical Journal International, **211**, no. 1, 541–557.

# ACKNOWLEDGEMENTS

My time as a PhD candidate at TU Delft has been a memorable experience thanks to many people. I would like to take the opportunity to express my gratitude to all of them.

This research started in December 2014, under the project of Acquisition and Preprocessing, in the Delphi Consortium. I would like to thank the sponsors for their financial support and all the interest and feedbacks at the sponsor meetings.

First and foremost, I would like to thank my promotors Gerrit Blacquière and Eric Verschuur for their invaluable guidance and continuous support. From the start of my PhD, we had many discussion about the project during our weekly meetings. Every time I had new ideas, Gerrit was very encouraging and supported me to evaluate these ideas to see whether they can be implemented. Thank you, Gerrit, especially for supporting me when I wanted to switch my research topic from deblending to acquisition design, and for brainstorming the new research proposal that we are both excited about.

Eric has been my promotor for the second half of my PhD on the acquisition design project. It has always been a pleasure to discuss my research with Eric and I enjoyed the chain of reasoning in our discussion. Thank you, Eric, for your guidance on defining and solving a research problem from scratch, and your constructive feedbacks to the research. Your enthusiasm to solving research problems motivated me to stay positive when both the research result and I were in the local minima.

I would like to thank Prof. Guus Berkhout for the discussions that contributed to the first part of this thesis. Thanks to Prof. Kees Wapenaar who hosted me in his geophysics group in the department of CiTG for the first four years of my PhD. Special thanks to Guy Drijkoningen for the opportunity to test shot repetition during the field campaign of the converted wave imaging research project that took place on the Danube river (Novi Sad, Serbia).

I would like to thank Gert-Jan van Groenestijn and Roald van Borselen for making my internship at PGS Leiden possible. My PhD journey initiated at PGS Leiden, where I completed my master thesis project and continued there part-time in the first year of my PhD. Thanks to my colleagues during that time: Rob Hegge, Rolf Baardman, Christina Dwiriyanti, Martijn Frijlink, Dorit Koenitz; I had a wonderful time there with you and the memory of the fun-and-smart team kept inspiring me to go through this PhD journey.

The last half year of my PhD was kindly hosted by the group of acoustical imaging in the faculty of TNW. Thanks to Eric and Prof. Nico de Jong for providing the opportunity to stay there. Thanks to Angela van der Sande and Annelies van Beek, for organizing the group activities. I felt home immediately and a part of the family of Quantitative Imaging.

I would like to thank Edo Bergsma and Henry den Bok for the great help and for making the high quality IT environment that we Delphi students are spoiled with. Typically we are not even aware of the node dropped off because you had already fixed it before

it would cause further problems. Special thanks to Guus Lohlefink, who magically saved the data in my hard disk when it was diagnosed as 'destroyed'.

I would like to thank Hanneke Berkhout, Gerrie van der Beek and who always made sure that the Delphi meetings would be smooth and greatly organized. Thanks to Lydia Broekhuijsen-Bentvelzen and the CEG support team who helped me with all the admin stuff throughout the PhD.

As a member of Delphi Consortium, I also enjoyed the meetings with the Delphi friends. Thank you all for your invaluable support. Gabriel, Apostolos, Xander, Amarjeet, Abdulrahman, Mikhail, Runhai, Matteo, Tomohide, Ozkan, Bouchaib, Prabu, Shogo, Ewoud, Halah, Tiexing, I wish you all the best after the Delphi journey. Shotaro, Billy, Jan-Willem, Aayush, Siddharth, Shan, Apprajita, Dong, Leo, Junhai, Hussain, Nick, Ali, Siamak, I wish you the all the best in finishing your PhD or continuing your paths as PostDoc in the Delphi family.

Thanks to my colleagues and friends at TU Delft who I shared many academic discussions, social, sport and art activities with: Remi, Helena, Quiten, Thais, Stephan, Martha, Santosh, Rahul, Youwei (Geology), Joost, Pawan, Asiya, Iris, Ranjani, Max, Karlien, Myrna, Lissanne, Florencia, Giovanni, Shohei, Shahar, Pieter, Atsushi, Lele, Musab, Gil, Joeri, Lissamme, Johno, Jianhuan, Chris, Nicholas, Bingkun, Reuben (Geophysics), Mengshi (Remote Sensing), Tian, Yan, Boling (Computational Imaging). I wish you all the best in continuing your paths in or outside of academia.

Thanks to my family who supported me with unconditional love throughout this journey. All my friends out there across the world have been a great motivation and support. You have constructively contributed to the completion of this thesis, probably without even realising it.

Finally, thank you Casper, I couldn't have done it without you.

Sixue

Royal Tunbridge Wells
March 2020

# CURRICULUM VITÆ

## Sixue WU

30-01-1990 Born in Wuhan, China.

## EDUCATION

| | |
|---|---|
| 2014 –2020 | Ph.D. in Geophysics<br>Delft University of Technology |
| 2012–2014 | Master of Science in Applied Geophysics<br>TU Delft, ETH Zürich, RWTH Aachen |
| 2008–2012 | Bachelor of Science<br>China University of Geoscience |